NANOSTRUCTURED MATERIALS WITH WELL-CONTROLLED DIMENSIONS, COMPOSITIONS AND ARCHITECTURES VIA PRECISE MOLECULAR DESIGN OF NON-LINEAR COPOLYMERS

A Dissertation
Presented to
The Academic Faculty

by

Yanjie He

In Partial Fulfillment
of the Requirements for the Degree
Doctor of Philosophy in the
School of Materials Science and Engineering

Georgia Institute of Technology
May 2018

NANOSTRUCTURED MATERIALS WITH WELL-CONTROLLED DIMENSIONS, COMPOSITIONS AND ARCHITECTURES VIA PRECISE MOLECULAR DESIGN OF NON-LINEAR COPOLYMERS

Approved by:

Dr. Zhiqun Lin, Advisor
School of Materials Science and Engineering
Georgia Institute of Technology

Dr. Meisha Shofner
School of Materials Science and Engineering
Georgia Institute of Technology

Dr. Vladimir Tsukruk
School of Materials Science and Engineering
Georgia Institute of Technology

Dr. Yulin Deng
School of Chemical and Biomolecular Engineering
Georgia Institute of Technology

Dr. Dong Qin
School of Materials Science and Engineering
Georgia Institute of Technology

ACKNOWLEDGEMENTS

I would like to thank my advisor Prof. Zhiqun Lin for his continuous support, motivation, and generosity. His perseverance and passion about nano-materials and energy related research highly motivate me to conduct research passionately through my Ph.D. His outstanding diligence in terms of designing new experiment, proposal writing and revising research articles indeed helps me to accomplish many achievements. He placed tremendous trust in me for generating ideas, solving problems and giving me opportunity to take part in two National Science Foudation funded and one Air Force Office of Rsearch funded projects. I would also like to thank all my dissertation committees, Prof. Vladimir Tsukruk, Prof. Dong Qin, Prof. Meisha Shofner, and Prof. Yulin Deng for their kind willingness to be my dissertation committee, and specially for offering me valuable comments and feedbacks to guide me through my research and successfully achieve the thesis goal.

I would not be able to accomplish this without the help and support from the members of NanoFM group. Particularly I would like to thank Prof. Xinchang Pang and Prof. Hui Xu for providing me with tremendous support and guidance regarding to knowledge and skill of polymer chemistry (especially ATRP). I would specially like to thank Dr. Chaowei Feng, Dr. Ming He, Dr. Beibei Jiang, Dr. Bo Li and Dr. Yijie Tao for being supportive and essential knowledge I learn from these wonderful people (e.g., controlled living polymerization, condensed matter physics, lithium ion battery). I am grateful for the help from Dr. Dajiang Zheng, Yeu-Wei Harn, James Iocozzia, Dr. Shiqiang Zhao, Zhe Cheng, Akanksha Menon, Prof. Shuguang Zhang, Prof. Jaehan Jung, Yajing

Chang, Shuang Pan, Dr. Yihuang Chen and Yoonjun Young. I would also like to thank current and former NanoFM group members, Prof. S. Li, Prof. H. Zhang, Prof. Y. Yang, Prof. D. Yang, Prof. R. Liu, Prof. Y. Yuan, Prof. Y. Wang, X. Xu, W. Han, C. Lu, Z. Wang, S. Liang, J. Yu, M. Rager, A. Wang, G. Biesold-Mcgee, X. Cui, X. Meng, K. Yuan, C. Gomez, B. Wang and M. Zhang.

I would also like to thank several professors for being kind and generous and allowing me to have access to their instruments, Prof. Younan Xia, Prof. Mostafa El-Sayed and Prof. Samuel Graham. Moreover, sincere gratitude goes to several staffs for training me and sharing knowledge and skills regarding various characterization instruments, Dr. Yong Ding, Yolande Berta and Dr. David Tavakoli. Lastly, I am extremely grateful to my dear parent for their unconditional love and constant support, without whom I would not be here.

TABLE OF CONTENTS

LIST OF TABLES

LIST OF FIGURES

LIST OF SYMBOLS AND ABBREVIATIONS

CRP	Controlled radical polymerization
ATRP	Atom transfer radical polymerization
CUAAC	Copper (I) catalyzed alkyne azide cycloaddition
GRIM	Grignard metathesis method
MNR	Nuclear magnetic resonance
GPC	Gel permeation chromatography
FT-IR	Fourier transform infrared spectroscopy
UV-Vis	Ultraviolet visible spectroscopy
PL	Photoluminescence
AFM	Atom force microscopy
TEM	Transmission electron microscopy
HRTEM	High resolution transmission electron microscopy
DLS	Dynamic light scattering
NIR	Near infrared spectroscopy
NCs	Nanocrystals
HNCs	Hollow nanocrystals
PNCs	Perovskite nanocrystals
CSNCs	Core shell nanocrystals
P*t*BA	Poly *tert* butyl acrylate
PS	Polystyrene
P4VP	Poly (4-vinylpyridine)
PEO	Polyethylene oxide

PEDOT	Poly(3,4-ethylenedioxythiophene)
NCs	Nanocrystals
PNCs	Perovskite Nanocrystals

SUMMARY

The past two decades witnessed the significant advancement of controlled living radical polymerization (CRP), leading to the controlled preparation of synthetic polymers that cannot be synthesized via traditional free radical polymerization. Living CRP techniques consisting of atom transfer radical polymerization (ATRP), reversible addition fragmentation chain transfer polymerization (RAFT) and nitroxide mediated polymerization (NMP) enable the fabrication of well-defined synthetic polymers with tailorable composition (e.g., block copolymers, alternating copolymers and statistical copolymers) and diverse architectures (e.g., star-like, bottle brush-like, dendrimer-like and hyperbranch-like). The generated synthetic copolymers prepared via CRP with tailorable chemical compositions and complex architectures have demonstrated unique properties compared to their linear counterparts. Notably, recent studies successfully demonstrate that tailor-made non-linear copolymers (e.g., star-like, bottle brush-like and necklace-like copolymers) play an essential role in directing the growth of inorganic nanocrystals, thereby leading to the formation of various polymer-capped inorganic nanoparticles, nanorods, nanotubes and nano-necklaces. The fact that well-defined non-linear copolymers can serve as the nanoreactors in nanocrystal formation overcomes a challenging task: although diverse inorganic nanocrystals can be synthesized through traditional colloidal synthesis routes, there are still several limitations associated with these well-established methods, which fail to prepare functional inorganic nanocrystals with complex morphologies. Therefore, this dissertation aims to utilize non-linear star-like triblock copolymers as nanoreactors to synthesize hollow nanocrystals and core-shell nanocrystals,

which are inaccessible to conventional colloidal synthetic strategies, as well as exploring the novel properties and enhanced performance originated from these complex architectures.

To be more specific, the novel and critical findings of this dissertation can be summarized as following bullets:

First, polystyrene-capped semiconducting hollow lead chalcogenides (e.g., PbTe and PbS) nanocrystals with tunable core diameter and shell thickness were crafted via the utilization of well-defined star-like PS-b-PAA-b-PS as nanoreactors where the precursors can be selectively partitioned into the space populated by PAA chains due to the strong coordination ability of PAA to PbTe precursors and the nanocrystals growth can be initiated at high temperature. Our nanoreactors strategy enabled the creation of semiconducting hollow lead chalcogenide nanocrystals with precise dimension control and tunable surface chemistry, which cannot be prepared by conventional synthetic approaches. The surface capping ligands can be tuned from insulating polystyrene to semiconducting conjugated PEDOT, thereby generating organic-inorganic hybrids consisting of semiconducting PbTe hollow nanocrystals as nano-fillers and the conducting PEDOT as matrix, which may be promising for organic-inorganic hybrid thermoelectrics. In addition, semiconducting hollow lead chalcogenides nanocrystals exhibited blue-shift of NIR absorption in comparison to solid lead chalcogenides counterparts, thus offering the possibility of controlling the design and synthesis of organic-inorganic hybrids.

Second, we designed two series of amphiphilic 21-armed P4VP-b-PtBA-b-PEO and P4VP-b-PtBA-b-PS via ATRP in conjunction with click reaction and utilized these

judiciously synthesized star-like macromolecules as nanoreactors to direct the growth of lead halide nanocrystals followed by in-situ conversion of them into the corresponding organo-lead halide perovskite nanocrystals. Encapsulation of these perovskite nanocrystals with a silica shell was achieved via in-situ hydrolysis of alkoxide silica precursor in the space occupied by PAA chains, leading to the formation of polymer-capped perovskite /silica core/shell nanocrystals with tunable core size as well as shell thickness. The resulting core-shell-1/shell-2 morphology composed of perovskite nanocrystals as core, silica coating as shell-1 and the polymer ligands as shell-2 exhibited an excellent stability while maintaining a good solution processability, which may be a promising candidate for the next-generation LEDs.

Finally, we extended this nanoreactors strategy to craft plasmonic-semiconducting (Au-CdS) core/shell nanocrystals with large lattice mismatch between core and shell materials by utilizing star-like amphiphilic 21-arm P4VP-b-PtBA-b-PEO as nanoreactors and demonstrated the core/shell nanocrystals' application in perovskite solar cells. Star-like amphiphilic 21-arm P4VP-b-PtBA-b-PEO nanoreactors circumvented the synthetic limitation imposed by epitaxial growth of core/shell nanocrystals through independently tuning the size of Au diameter owing to the strong coordination ability of pyridyl groups in P4VP blocks and the selective partitioning of CdS precursor by PAA chains. In comparison to conventionally prepared Au-CdS capped by oleylamine and oleic acid, the resulting PEO- capped Au/CdS core/shell nanocrystals achieved an optimum length of PEO to facilitate the transportation of carriers and the chemical compatibility with organo-lead iodide active layer in perovskite solar cells, thereby leading to a good photovoltaic conversion efficiency improvement.

In summary, the bottom-up crafting of nanomaterials with complex architectures, tunable dimensions, controlled chemical compositions and well-defined surface chemistry promises new opportunities to tailor-make next-generation nanomaterials for a myriad of applications, including lithium ion batteries, photovoltaic devices, thermoelectrics, catalysis, electronics, nanotechnology, and biotechnology.

.

CHAPTER 1. INTRODUCTION

1.1 Background

1.1.1 Atom Transfer Radical Polymerization

Macromolecular engineering comprises precise design, synthesis, processing, and characterization of well-defined polymers with specific properties suitable for targeted applications. Currently, polymers can be synthesized with precision matching that of pharmaceutically active organic compounds via controlled radical polymerization (CRP). [1] In contrast to conventional radical polymerization (e.g, free radical polymerization) where initiation, propagation and termination take place in an uncontrolled way, controlled radical polymerization or reversible-deactivation radical polymerization introduces the concept of dynamic equilibrium, thereby rendering the synthesis of polymers with controlled molecular weight, tunable chemical composition (e.g., block, graft, alternating, and gradient copolymers), narrow polydispersity (e.g., polydispersity<1.3) and complex architecture (e.g., star-like and bottle brush-like) possible. Currently, there are three well-established controlled radical polymerization techniques that enable the preparation of well-defined copolymers with complex architectures: (a) nitroxide-mediated radical polymerization (NMP) where copolymers with well-controlled stereochemistry was initiated by a alkoxyamine compound and the livingness nature was owing to the persistent radical effect, [2] (b) reversible addition-fragmentation chain-transfer polymerization (RAFT) where the livingness and low polydispersity were realized via utilizing thiocarbonylthio compound as chain transfer agent [3] and (c) atom transfer radical polymerization (ATRP) where well-controlled polymerization process was mediated

through using metal halide (e.g., copper(I) bromide) in lower oxidation state as catalyst in the presence of organic amine serving as ligand. [4] Of these three living radical polymerization techniques, ATRP is the most attractive technique across laboratories, disciplines and levels of chemical expertise because of the wide availability of initiators (e.g., alkyl halides whereas the initiator for RAFT requires complicated thiocarbonylthio compounds) and the abundance of catalysts (e.g. metal halide salts).

The livingness of ATRP is achieved via dynamic equilibrium between propagating radicals and inactive species. [1, 5] The concept of dynamic equilibrium was firstly demonstrated in Matyjaszewski's group where well-defined polystyrene with narrow molecular distribution and pre-determined molecular weight was prepared via employing 1-phenylethyl chloride as initiator, 2,2-bipyridine as ligand and widely accessible copper(I) chloride as catalyst. [6] The initiation process took placed by the abstraction of chlorine atom from 1-phenylethyl chloride initiator by copper-bipyridine complex (i.e., chlorine atom transfer promoter), thereby generating radials that initiated polymerization. More importantly, a linear relationship of In([M]d[M]) with respect to polymerization time indicated that the concentration of active radicals in reaction solution was constant and the irreversible termination that caused large molecular weight distribution was not significant, suggesting the livingness nature of whole polymerization process. [6, 7] In general, ATRP mechanism follows a process by which the dormant species periodically react with transition metal complex in lower oxidation state to intermittently produce growing radicals and transition metal complex in higher oxidation state serving as deactivator to maintain a constant level of growing radicals in reaction solution. Ever since the discovery of ATRP, [8] this polymerization technique has been extended to prepare diverse polymers

with very low PDI, including substituted styrene, [9, 10] methacrylates, [11, 12] functional acrylates, [13-17] acrylonitrile [18, 19] and acrylamides. [20-22] Although ATRP is a powerful technique to polymerize diverse monomers, polymerization of monomers (e.g., 4-vinylpyridine) that form unfavorable complex with transition metal catalysts usually leads to ill-defined polymers forming polymer network or polymer gel. Xia *et al.* reported synthesis of well-defined poly (4-vinylpyrinde) via utilizing very strong ligand (i.e. tris[2-(dimethylamino)ethyl]amine denoted as Me_6TREN). [23] The well-controlled polymerization is attributed to the strong coordination ability of Me_6TREN in comparison to conventional amine ligands as well as the high polymerization rate originated from the structure of Me_6TREN. The effect of ligand structure on the activation rate of ATRP process is summarized in **Figure 1.1**. [24] Another important factor affecting the livingness of ATRP is the reactivity of alkyl halide initiators. It is well-established that the reactivity of alkyl halides follows the order of I>Br>Cl in agreement with bond dissociation energy required for hemolytic bond cleavage. [1] However, the reactivity of alkyl iodide is too high to achieve a good control during polymerization. Thus, the most common initiators used in ATRP are generally alkyl bromide or alkyl chloride.

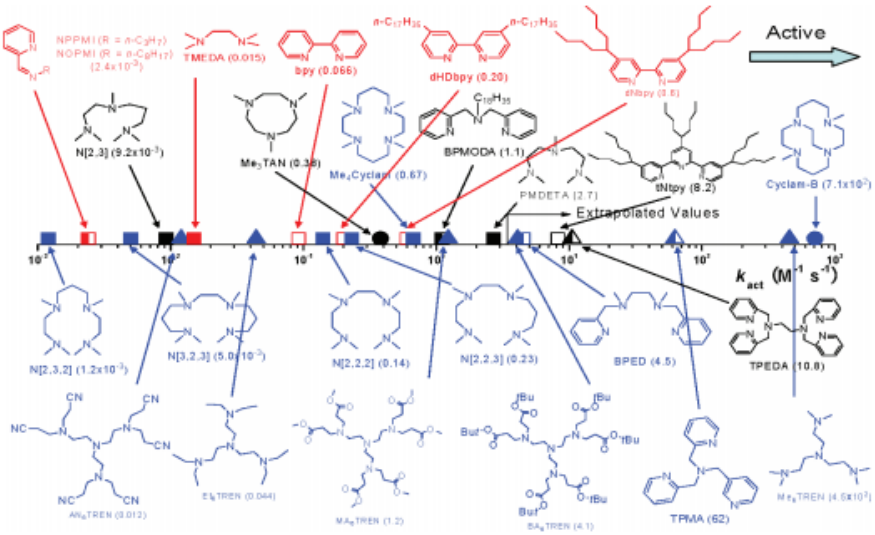

Figure 1.1 ATRP activation rate for various ligands with EtBriB in the presence of copper bromide in MeCN at 35 C. [1]

Currently, there are five modified ATRP with different advantages: (a) activators regenerated by electron transfer (ARGET) ATRP [25] where a much lower concentration of copper catalyst was used, indicating potential industrial scale-up production, (b) initiators for continuous activator regeneration (ICAR) ATRP [26] where the process is considered as a reversed ARGET ATRP, (c) eATRP [27] where the activator Cu(I) is regenerated via electrochemical process, (d) supplemental activator and reducing agent (SARA) ATRP [28] where zero valent transition metal halide is used as catalyst to activate alkyl halides in order to decrease the amount of transitional metal halide used in system and (e) photoinduced ATRP [12] where ATRP can be performed in ppm level of catalyst. The development of aforementioned ATRP is to decrease the amount of transitional metal halide catalysts involved in reaction, which is promising for the industrial production of well-defined copolymers with narrow size distribution and pre-determined molecular weight. Nonetheless, these ATRP routes still rely on the trace amount of transitional metal halides

as catalysts. ATRP process without relying on the usage of transitional metal halides was independently developed by Hawker's group [29] and Miyake's group. [30] Metal free ATRP was achieved via employing organic photosensitizer which can abstract halide from alky halide initiator under the illumination of UV light, thereby producing radicals. The mechanism of metal free ATRP is schematically illustrated in **Figure 1.2**. This metal free ATRP completely avoids the usage of any transitional metal catalysts in reaction, which is very promising for the future mass-production of well-defined copolymers.

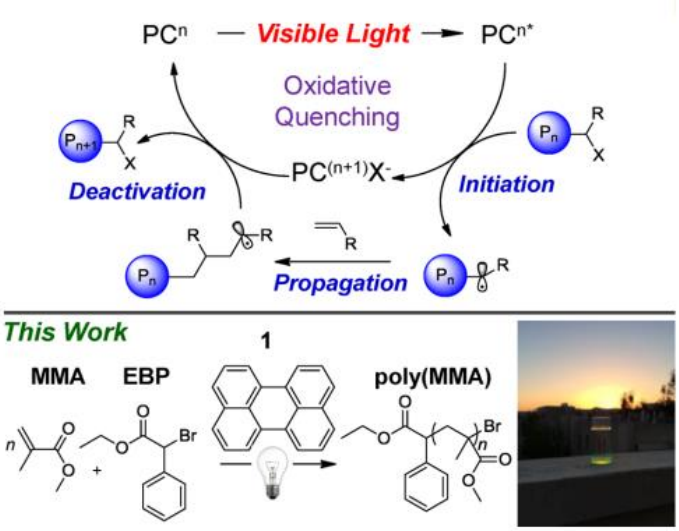

Figure 1.2 Proposed mechanism for the photoinduced metal-free ATRP process mediated by using perylene as an organic photocatalyst for the polymerization of methyl methacrylate with alkyl bromide initiators. [30]

1.1.2 Recent Progress on Synthesis of Lead Chalcogenides Nanocrystals

The preparation of high-quality inorganic nanocrystals (NCs) with narrow size distribution (e.g., monodispersed NCs generally possessed size distribution less than 5%) enabled the diverse applications, including catalysis, biomedicine, nanoelectronics, bio-

imaging, high-performance thermoelectrics, lithium ion battery as well as the fabrication of the state-of-the-art high efficiency photodetectors, solar cells. [31] Monodispersed NCs was firstly demonstrated in gold NCs via reducing tetrachloroauric acid aqueous solution by sodium citrate also functioning as surface capping ligands, thereby producing water-soluble monodisperse gold NCs with size tunable from 2 nm to 14 nm and narrow localized surface plasmon resonance peak around 520 nm. [32, 33]

With the aid of the development of electron microscope, the last two decades witnessed the tremendous advancement of colloidal synthetic strategies for crafting uniform NCs with different compositions. One classic synthetic liquid-solid-solution (LSS) phase transfer and separation route developed by Li. *et al* firstly demonstrated a general and facile approach for making various categories of inorganic NCs (e.g., noble metal, transition metal oxides, metal chalcogenides and metal hydroxide, etc.) by which the metal ions in aqueous state was transferred into solid state followed by the dehydration of metal ions in solid phase to produce NCs (**Figure 1.3**). [34] Meanwhile, the short-chain ligands employed to facilitate LSS phase transfer and separation process functioned as stabilizing ligands, endowing inorganic NCs good solubility in non-polar organic solvents.

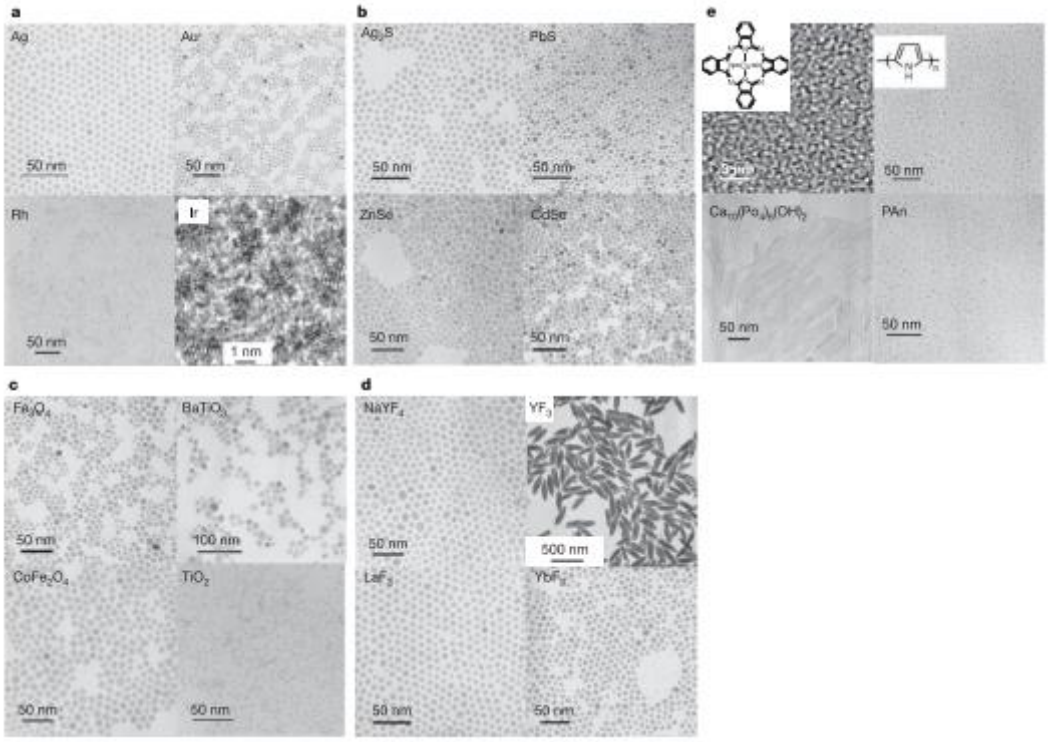

Figure 1.3 Various inorganic nanocrystals with narrow size distribution prepared via liquid-solid-solution phase transfer and separation process. [34]

Another widely used synthetic approach for crafting monodispersed NCs developed by Hyeon *et al.* was achieved by thermolysis of metal-oleate precursor in high boiling point organic solvent in the presence of short chain ligands (e.g., oleylamine or oleic acid) which tended to tether on the surface of NCs and prevented the aggregation of NCs. [35] One characteristic of this synthetic strategy is that it is readily to increase the scale of experiment to produce a large amount of high quality iron oxide NCs in one batch (**Figure 1.4**). The facile preparation of other metal-oleate precursors not only enabled the extension of this approach to other metal oxide NCs with narrow size distribution (e.g., cobalt oxide, manganese oxide and nickel oxide, etc.) but also offered a powerful platform to investigate the self-assembly behavior of superparamagnetic NCs. [36, 37]

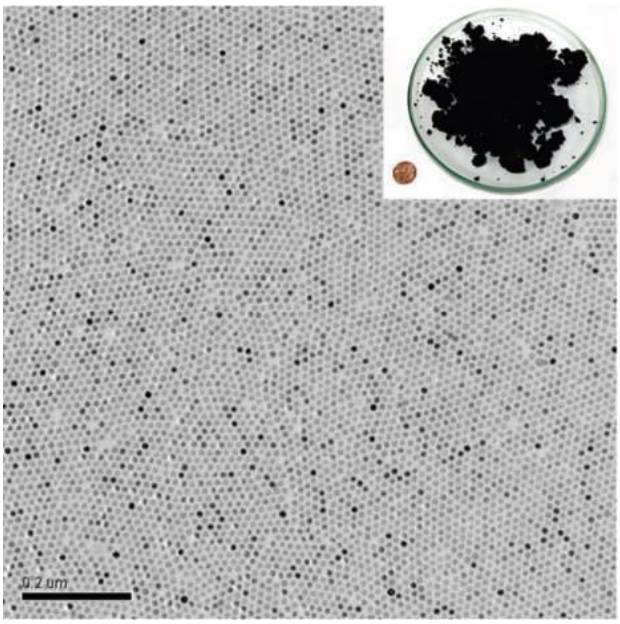

Figure 1.4 The TEM image clearly illustrates that the size of iron oxide NCs have uniform particle-size distribution with inset showing the mass-production of NCs for one batch. [35]

These two classic synthetic strategies mainly focused on the insulating metal compound NCs. One pioneering work developed by Bawendi's group firstly demonstrated that monodispersed semiconducting cadmium based chalcogenides NCs can be prepared by hot injection method, investigating the optical properties of a series of semiconducting NCs with significant quantum confinement effect. [38] As-synthesized cadmium chalcogenides NCs with size below the critical value (e.g., Bohr radius) exhibited the pronounced side-dependent optical band gap. The formation mechanism of cadmium chalcogenides NCs can be rationalized by La Mer NC formation mechanism. In a typical synthesis of cadmium chalcogenides NCs, highly reactive metal alkyls (e.g., dimethylcadmium and diethylcadmium) was dissolved in high boiling point coordination solvents (e.g., octadecene) followed by quick injection of oganophosphine chalcogenides prepared by dissolving sulfur or tellurium in organophosphate. According to the growth of

monodisperse NCs based on La Mer model, rapid injection of regents into reaction increased the precursors concentration to a critical level above which the formation of nuclei and the growth of NCs were energetically favorable. The nucleus initiated the growth of NCs and all NCs in the system kept growing without the presence of newly formed nucleus provided that the rate of consumption of precursors by the existing NCs was much higher than the feeding rate of precursors. The initial size distribution of cadmium chalcogenides NCs was largely dependent upon the time over which the nuclei were formed and initiated the growth process. The size distribution of resulting NCs can further be narrowed by subsequent Ostwald ripening process by which large NCs tended to continuously grow with the dissolution of small-sized NCs with high surface to volume ratio to decrease the total free energy of the system. [39]

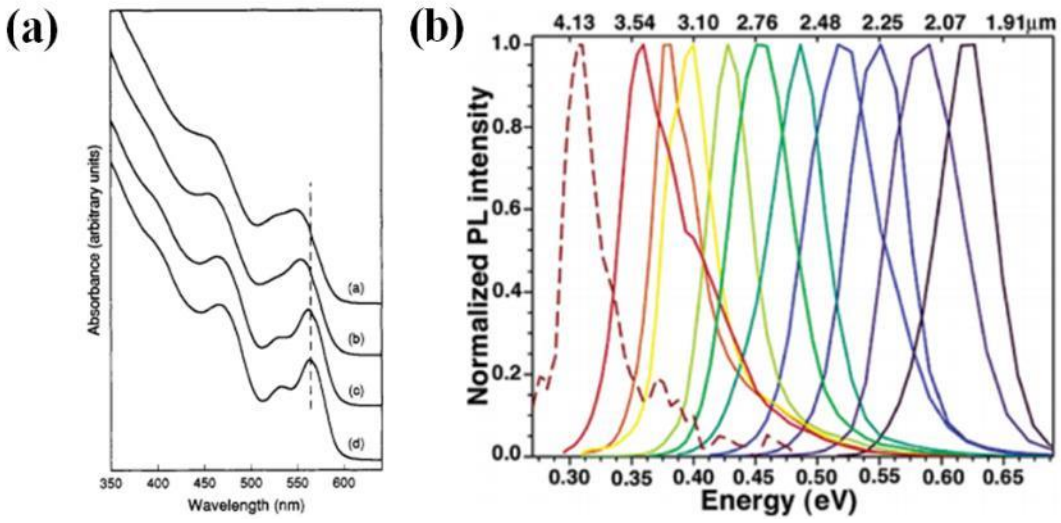

Figure 1.5 Optical properties of semiconducting (a) cadmium selenide (CdSe) nanocrystals UV-Vis absorption peaks in visible range and (b) lead selenide (PbSe) nanocrystals photoluminescent spectra in near-IR range. [38, 40]

This hot injection method for preparing cadmium chalcogenides NCs had been extended to the synthesis of various semiconducting narrow band gap NCs, rendering the investigation of optical properties of narrow band gap NCs possible. There are two essential characteristics of narrow band gap NCs in comparison to wide band gap NCs. First, the narrow band gap generally indicates the relatively high electrical conductivity, which is very important for serving as active materials in the functional devices. For instance, photovoltaic devices (e.g., solar cells) usually requires the band gap of active layer less than 2.0 eV, which is not accessible to cadmium chalcogenides NCs. Similarly, theories concerning thermoelectric materials demands that a promising candidate for thermoelectric devices should possess high electrical conductivity, low thermal conductivity and high Seeback coefficient, which prevents the application of wide band gap NCs in thermoelectrics and other energy harvesting applications. Another characteristic that wide band gap NCs cannot compete with narrow band gap counterparts is related to the effective tunable wavelength range or tunable band gap range. Unlike wide band gap NCs (cadmium chalcogenides NCs) only possessing tunable wavelength through visible range and the band gap larger than 1.5 eV (e.g., cadmium telluride), the tunable wavelength range and optical band gap of narrow bad gap NCs (e.g., lead chalcogenides NCs) are able to cover from near-IR to visible range. The comparison of optical properties of CdSe and PbSe is shown in **Figure 1.5**. [38, 40] Because of this, narrow band gap, especially lead chalcogenides NCs have a wide varieties of application in solar cells (e.g., band gap alignment with respect to hole transport layer and electron transport layer can be readily accomplished by synthesizing lead chalcogenides NCs with interested band gap), thermoelectric devices (e.g., electrical conductivity, thermal conductivity and Seeback

coefficient can be rationally designed and tuned) and photodetectors (e.g., lead chalcogenides NCs possess high photoluminescent emission at near-IR range).

The lead sulfide (PbS) NCs is the first important low band gap NCs in the family of lead chalcogenides NCs with band gap=0.37 eV in bulk state, suggesting that the optical band gap of PbS NCs can be continuously tuned starting from 0.37 eV (3351 nm) to visible range. Hines *et al*. reported the synthesis of oil-soluble PbS NCs by replacing labile metal alkyls with stable metal-oleate as precursor followed by hot injection of bis(trimethylsilyl) sulfide, leading to the formation of PbS NCs with very narrow size distribution. [41] As a result, as-synthesized PbS NCs exhibited clearly pronounced excitonic absorption spectrum (**Figure 1.6**). The surface chemistry of these PbS NCs can be readily tuned from long-chain ligands (e.g., oleic acid or oleylamine) to shorter alkylamines, thereby facilitating the injection of electron and holes into the NCs by decreasing the chain length of the ligands for potential optoelectronic application.

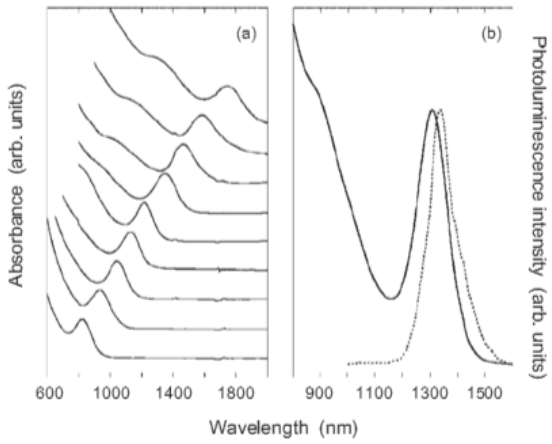

Figure 1.6 Optical properties of PbS NCs in toluene (a) absorption peak and (b) photoluminescent peak. [41]

The synthesis of PbS NCs via hot injection method was further developed by Kruger *et al.* who employed modified approach by using other lead precursors [42] and Li *et al.* who used octadecene to dissolve sulfur and lead oxide without using any organosulfate in the presence of oleic acid and oleylamine. [43] In addition, PbS NCs can be synthesized via thermolysis of single PbS precursor (i.e., a single precursor consisted of lead and sulfur source) by soft hydrothermoal method, producing nanostructured PbS with irregular structures. [44]

Cademartiri *et al.* reported an alternative approach to hot injection method by dissolving lead precursor in oleylamine, thereby forming high viscous gel, followed by injection of sulfur precursor dissolved in oleayamine. Despite the requirement of delicate purification process, this synthetic approach enabled the formation of monodispersed PbS NCs, which self-assembled into large-scale superlattice. The low polydispersity of PbS NCs also rendered the investigation of size-dependent transition energies, extinction coefficient and per particle absorption cross section possible. [45]

Although oil-soluble PbS NCs prepared from hot injection method mentioned above exhibited tendency to decompose or undergo phase transformation in the contact of water molecules, Bakueva *et al.* reported the one-stage synthesis of water-soluble PbS NCs via utilizing thioglycerol and dithioglycerol as co-stabilizing ligands, resulting high quality and stable NCs displaying clear luminescence peak from 1000 to 1400 nm. The high quantum yield of as-synthesized PbS NCs can be maintained exposure to different environment (e.g., DNA solutions or semiconducting polymer matrix), suggesting potential application in bio-imaging and optical fiber communication devices. [46]

Lead telluride (PbTe) NC with very large excitonic Bohr radius (46 nm) and light electron and hole masses is another important low band gap NCs in the family of lead chalcogenides NCs, which exhibit potential application in solar cells, thermoelectric devices, telecommunication, field effect transistors and bio-imaging. [47-49] Since the bulk PbTe has lower band gap (0.28 eV) than bulk PbS (0.37 eV), PbTe NCs demonstrate wider tunable wavelength range in comparison to PbS NCs. Lu *et al.* firstly reported the controlled synthesis of monodisperse PbTe NCs via hot injection of mixture solution consisting of tellurium dissolved in trioctylphosphine (TOP-Te) and lead acetate into hot phenyl ether. [50] The morphology of resulting monodisperse PbTe NCs can be tuned from spherical shape to cubic shape by varying the reaction temperature. Later, Mokari *et al.* reported a modified hot injection method with the aid of hydrocarbon long-chain amines (i.e., hexadecylamine and dodecylamine) to precise tune the morphologies of PbTe NCs through controlling the growth of specific lattice plane. [47] However, both of these studies did not measure the excitonic absorption peak and PL emission of PbTe NCs. The uniformity of PbTe NCs was further improved by Urban *et al.* via hot injection of TOP-Te into lead oleate in hot squalene with oleic acid functioning as ligands. [48] This approach resulted in highly monodisperse PbTe NCs (**Figure 1.7**), leading to strong tendency to from large-scale ordered packing in thin film state.

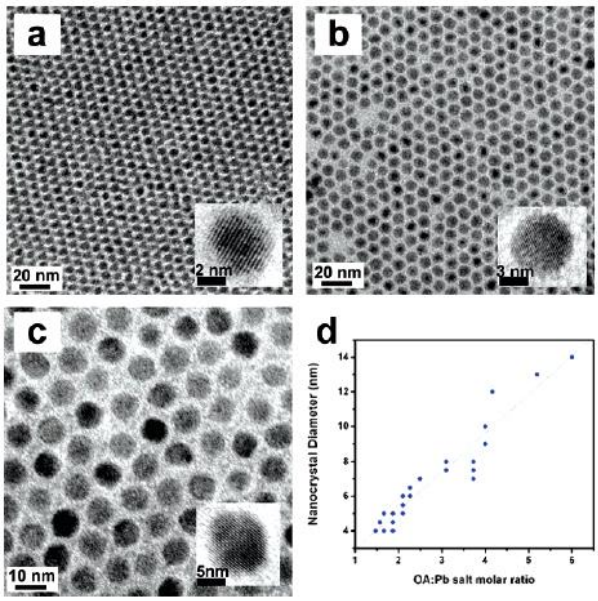

Figure 1.7 TEM images of PbTe NCs with different sizes (a) 5.0 nm, (b) 6.5 nm, (c) 8.2 nm and (d) relationship of the size of PbTe NCs with respect to the ratio of oleic acid to Pb salt. [48]

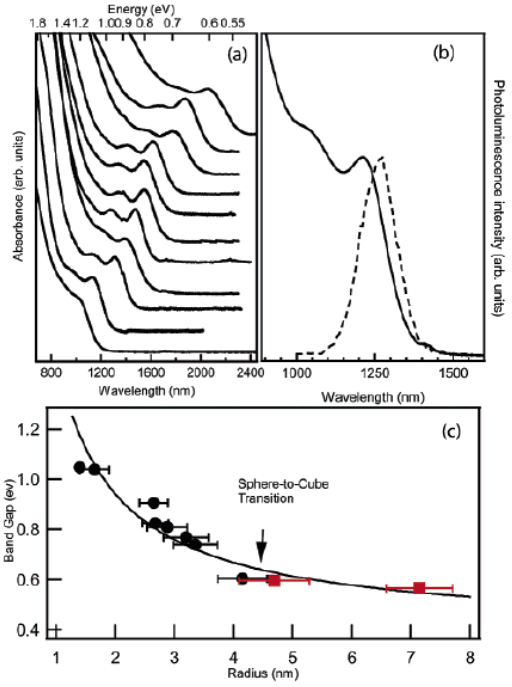

Figure 1.8 (a) Near-IR absorption of PbTe NCs with energy excitonic transition tunable from 1009 to 2054 nm and (b) relationship between optical band gap and the size of PbTe NCs. [49]

Moreover, based on the highly monodisperse PbTe NCs, the optical properties were investigated by Urban *et al.* [48] and Mruphy *et al.* [49], displaying evident first exciton absorption peak and PL emission spectra with quantum yield as high as 52% (**Figure 1.8**). The high uniformity of PbTe NCs also allowed the first observation of efficient multiple exciton generation (i.e., carrier multiplication effect) from single photons absorbed in PbTe NCs, which was impossible for semiconducting NCs with large band gap.

There are not too many papers concerning the synthesis of uniform PbTe NCs with clear exitonic absorption peaks and PL emission due to several reasons. First, the extremely poor solubility of tellurium in most of organic solvents impeded the advancement of new synthetic strategies. It was found that unlike other elements such as sulfur and selenium, both of which can be dissolved in diverse organic solvent (e.g., oleylamine and octadecene, etc.), the only good solvent for Te was trioctylphosphine. [48] Another reason for the lack of papers related to the synthesis of monodisperse PbTe NCs is due to the lack of appropriate ligands to control the growth of NCs.

1.1.3 Recent Progress on Synthesis of Lead Halide Perovskite Nanocrystals

Ever since the first discovery of high performance in thin film lead halide perovskite based photovoltaic device in 2013, [51] there are extensive studies concerning the energy harvesting and conversion applications of this family of materials with remarkable high power conversion efficiencies of more than 22% and extreme high extremal quantum

efficiencies of lead halide perovskite light-emitting diodes over 10%. [52, 53] Unlike conventional semiconducting metal chalcogenides (e.g., cadmium and lead chalcogenides) used in last generation of photovoltaic devices, lead halide perovskite are highly ionic compounds, suggesting that they can readily form highly crystalline ABX_3 (X=Cl, Br and I) structures composed of three-dimensional arrangement of $[PbX_6]$ octahedrons in corner sites with A cation (e.g., methylammonium, cesium and formamidium cation) fitted into central location. The successful demonstration of high performance and readily formation of lead halide perovskite in thin film devices generated the motivation to investigate the colloidal synthesis of perovskite nanocrystals (PNCs). [54]

The first successful demonstration of colloidal synthesis of organic-inorganic hybrid lead halide PNCs was reported by Schmidt *et al.* via utilizing long alkyl chain ammonium cations (i.e., octylammonium bromide or octadecylammonium bromide) as stabilizing ligands to control the growth of $MAPbBr_3$ (MA=methylammonium cation) PNCs. [55] As-synthesized octylammonium bromide capped 6-nm $MAPbBr_3$ PNCs exhibited good colloidal stability over months without requiring a mesoporous materials, narrow bandwidth of the visible spectrum and a descent quantum yield (20%). However, the size distribution of this organic-inorganic PNCs was still relatively large and the quantum yield was not high enough for lighting and display application. Later, Zhang *et al.* developed a facile and room-temperature preparation of highly luminescent organic-inorganic PNCs with tunable chemical compositions with quantum yield as high as 70% which demonstrated the wide gamut prototype LED devices. [56] This ligand assisted reprecipitation (LARP) synthetic strategy involved precipitating precursor solution consisting of lead halide and organoammonium halide dissolved in dimethylformamide

(DMF) into toluene (i.e., poor solvent for perovskite materials) under vigorous stirring while utilizing long–chain molecules (e.g., oleic acid and n-octylamine) as co-ligands (**Figure 1.9**). This LARP method was further developed by conducting precipitation reaction at elevated temperature to control the size of PNCs, thereby observing the size-dependent band gap of $MAPbBr_3$ PNCs with quantum yield tunable from 74% to 94%. In addition, this synthetic strategy was extended with modification to the synthesis of organic-inorganic amorphous nanoparticles via using DMF and γ-butyrolactone as co-solvents. The formation of amorphous $MAPbBr_3$ nanoparticles is owing to the fact that the addition of γ-butyrolactone can destroy the soft framework of lead halide octahedrons in DMF and free lead halide octahedrons cannot crystalize into nanocrystals even in the presence of octylamine, thereby leading to the $MAPbBr_3$ amorphous nanoparticles. As-synthesized amorphous $MAPbBr_3$ nanoparticles still exhibited clearly absorption peak and interesting temperature-independent photoluminescence properties in contrast to crystalline $MAPbBr_3$ NCs with temperature-dependent photoluminescence properties. Because of this, amorphous $MAPbBr_3$ nanoparticles based LED devices exhibited very high internal quantum efficiency.

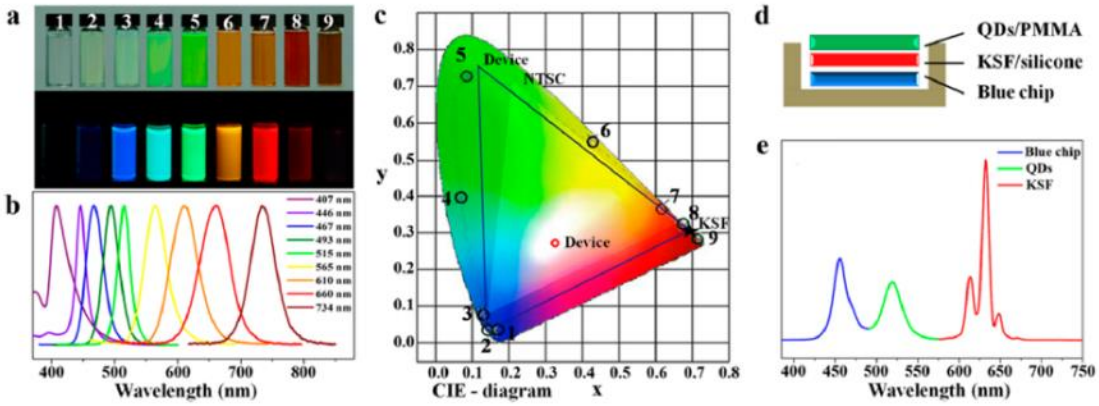

Figure 1.9 Color tunable $MAPbX_3$ PNCs and wide-colar gamut LED devices (a) optical images of $MAPbX_3$ PNCs, (b) PL emission spectra of $MAPbBr_3$ PNCs, (c) CIE coordinates corresponding to the $MAPbX_3$ PNCs and (d)(e) schematic diagram and EL spectra of LED devices using $MAPbBr_3$ PNCs and red emissive rare-earth phosphor KSF**.** [56]

Although previous synthetic strategies are very effective to prepare high-quality organic-inorganic PNCs with the tunable wavelength covering the whole visible range, LARP method only allows the preparation of organolead iodide PNCs with extremely poor stability, even performing LARP in glove box. Performing LARP in open air generally resulted in white flocculent composed of micro-size crystals without showing any emission peak in visible range. Detailed investigation of solvent effect indicated that lead iodide has a strong tendency to coordinate with DMF to form lead halide-DMF intermediate. Although this intermediate underwent crystallization process with mathylammonium iodide to form $MAPbI_3$ PNCs in the presence of capping ligands, the resulting $MAPbI_3$ PNCs still contained residual solvent molecules on the surface, which can form iodine vacancies due to the removal of solvent molecules. These defects due to the presence of residual solvent molecules and iodine vacancies caused the transformation from $MAPbI_3$-solvent to $MAPbI_3$-water and eventually leaded to the fully decomposition.

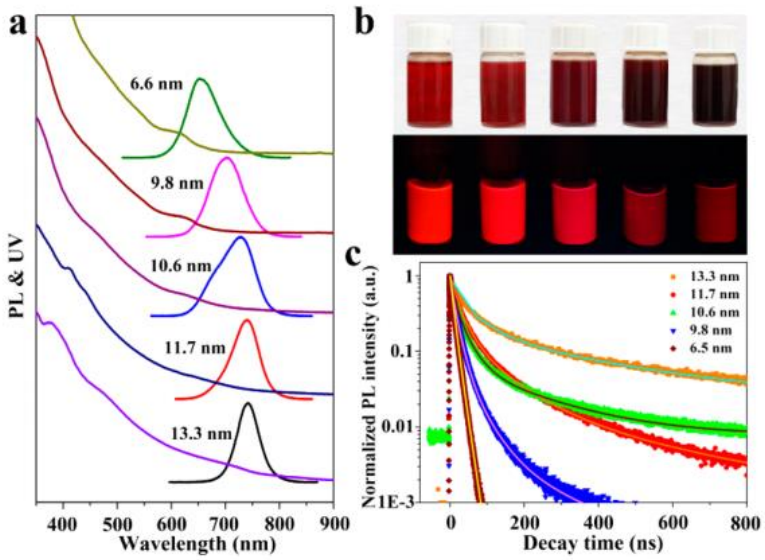

Figure 1.10 (a) Preparation of $MAPbI_3$ PNCs with different sizes using non-coordination solvent, (b) digital images of $MAPbI_3$ PNCs under room light and UV light and (c) time resolved photoluminescent spectra of $MAPbI_3$ PNCs. [57]

In order to tackle this instability issue of $MAPbI_3$ PNCs, Zhang *et al.* reported using acetonitrile as good solvent for PNCs preparation, which did not coordinate with lead halide, thereby rendering the synthesis of $MAPbI_3$ PNCs at ambient condition possible. [57] The resulting $MAPbI_3$ PNCs not only exhibited size-dependent optical property owing to the quantum size confinement, but also were stable for several weeks while still maintaining bright red luminescence at ambient condition (**Figure 1.10**).

Based on the success of conventional semiconducting colloidal NCs through hot injection method, Protesescu *et al.* reported a controlled arrested precipitation method (modified hot injection method) via injecting cesium-oleate solution into lead halide dissolved in octadecene with the aid of oleylamine and oleic acid. [58] This modified hot injection method enabled the preparation of monodispersed cesium lead halide PNCs with

readily tunable size, visible spectral region (i.e., 410 to 700 nm) and chemical composition by combining appropriate ratio of lead halide salts (**Figure 1.11**). The resulting cesium lead halide PNCs not only enabled the strong tendency for self-assembly (**Figure 1.11a**), but also exhibited potential optoelectronic applications such as lasing, LEDs, photovoltaics, and photon detection due to the narrow emission line-widths and very high quantum yield (i.e., up to 90%). In addition to narrow emission line-width, high quantum yield and widely tunable wavelength range, the chemical composition of PNCs can be readily tuned by a simple post-treatment anion exchange process, thereby tuning the optical properties of PNCs. The optical properties of conventional semiconducting NCs can only be tuned by varying the size of NCs, thereby tuning the band gap of NCs and the variation of chemical composition has to be performed in elevated temperature with elongated time. For instance, in the case of CdSe NCs, the substitution of S with Te via anion exchange only caused a limited change of absorption peak and complete compositional tuning of PbTe to CdTe via cation exchange generally required more than 12 hours at elevated temperature with a little bit of morphology change. On the contrary, the chemical composition of lead halide perovskite can be readily tuned by simply mixing with compounds capable of delivering halide ions at room temperature. This anion exchange process took placed within few seconds and was capable of reversible tuning the composition from chloride to iodide with preserving the shape and size of original NCs, thereby tuning photoluminescence across whole visible range. Fast anion exchange reaction also happened among PNCs with different chemical composition, eventually leading to the homogenization of PNCs. [59]

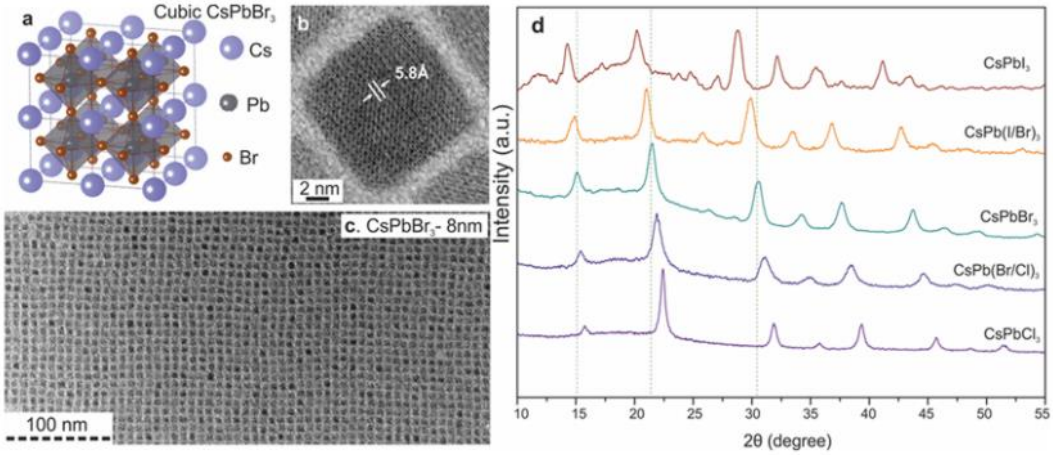

Figure 1.11 Monodisperse $CsPbX_3$ NCs and their structural characterization (a) cubic perovskite lattice, (b)(c) TEM images of $CsPbBr_3$ NCs and (d) XRD patterns of typical ternary and mixed-halide NCs. [58]

Another interesting property of lead halide PNCs is that the surface capped ligands have a highly dynamic equilibrium in a sense that the long-chain ligands (e.g., oleic acid and oleylamine) tends to undergo attachment and detachment equilibrium, which is the principle reason for the colloidal instability when PNCs are exposed to repetitive solvent washing during purification steps. However, this highly dynamic nature offers a powerful way to conduct surface passivation, which enhances the optical properties of lead halide PNCs. Previous synthetic strategies enabled the fabrication of lead halide PNCs with quantum yield ranging from 20% to around 90% depending on the chemical composition and, more importantly, surface chemistry of PNCs (i.e., surface capping ligands are expected to decrease the defects exited in the NCs). Post-treatment via passivating appropriate ligands is able to significantly improve the optical properties of PNCs. For instance, surface passivation oleyleamine or oleic acid capped cesium lead bromide PNCs via treating with thiocynate salts was capable of effectively decreasing the non-radiative

pathways of PL decay, thereby enhancing the freshly prepared PNCs with 90% quantum yield and aged PNCs with 70% quantum yield to almost 100%. [60] The thiocynate salts treatment can repair lead-rich surface on PNCs (i.e., defects), accessing a limited number of surface sites without leading to the destruction of the entire NCs. This thiocynate salts treatment was also extended to lead halide PNCs with different chemical compositions but with limited improvement of PL quantum yield.

Moreover, highly dynamic surface chemistry of lead halide PNCs in combination with deliberate purification step can retain unstable perovskite phase which is thermodynamic unfavorable in bulk state. $CsPbI_3$ perovskite tended to stay in orthorhombic structure (i.e., cubic phase was not stable at room temperature) at ambient condition, which had a large band gap and weak light absorbing ability and therefore was not suitable for optoelectronic application. Traditionally prepared $CsPbI_3$ PNCs quickly transformed from cubic phase to orthorhombic phase, losing light emitting ability especially in contact with common solvents used in PNCs purification process. The removal of surface–stabilized ligands due to excess washing also induced instantaneous transformation to orthorhombic phase. Swarnkar *et al.* developed a very effective purification process by which the purification of $CsPbI_3$ PNCs via using methyl acetate as precipitant was employed to not only separate $CsPbI_3$ PNCs from unreacted precursors, but also maintain the cubic phase at ambient condition for several months. $CsPbI_3$ PNCs prepared from conventional hot injection method were exposed to a series purification steps with great deliberation in the presence of methyl acetate which removed excessed precursors and ligands capped on PNCs, thereby eventually leading to large energy contribution from PNCs surface. [61] The stable cubic-phased $CsPbI_3$ PNCs also exhibited excellent tendency for self-assembly into

structure that allowed efficient dot-to-dot electronic transportation, which demonstrated good power conversion efficiency in all-inorganic PNCs based optoelectronic devices. Later, Liu *et al.* reported that a trioctylphosphine-based synthetic strategy in combination with methyl acetate based isolation method resulted in not only stable $CsPbI_3$ PNCs but also significant enhanced optical properties. [62] In contrast to conventional methods using long-chain amine to dissolve lead iodide, this route employed trioctylphosphine as a solvent for halide source, crafting near-perfect photophysical $CsPbI_3$ PNCs with record-breaking high quantum yield (i.e., 100%), longer radiative lifetime and the negligible electron or hole-trapping pathways. The same research group had successfully extended this synthetic route to more unstable lead halide PNCs (i.e., $CsSnI_3$) in comparison to $CsPbI_3$ PNCs. Although $CsPbI_3$ PNCs have been incorporated into photovoltaic devices with descent conversion efficiency, the band gap of $CsPbI_3$ PNCs are still too large compared to the organic-inorganic hybrid perovskite. Doping tin in B sites to form $CsSn_{1-x}Pb_xI_3$ are expected to decrease the band gap of PNCs. However, it was found that $CsSnI_3$ perovskite immediately lost single crystallinity and degraded to the yellow phase with very poor optical properties followed by irreversible oxidation into metallic Cs_2SnI_6 due to the readily oxidation of Sn^{2+} to Sn^{4+}. Consequently, previous synthesis of $CsSnI_3$ PNCs was required to perform in glove box with very limited stability upon exposure to ambient condition. Utilization of trioctylphosphine as solvent for lead halide source in combination with methyl acetate as precipitant resulted in successful fabrication of high-quality of $CsSn_{1-x}Pb_xI_3$ PNCs which showed enhanced chemical stability even exposure to air and promising application in solar cells with high photocurrent. [63]

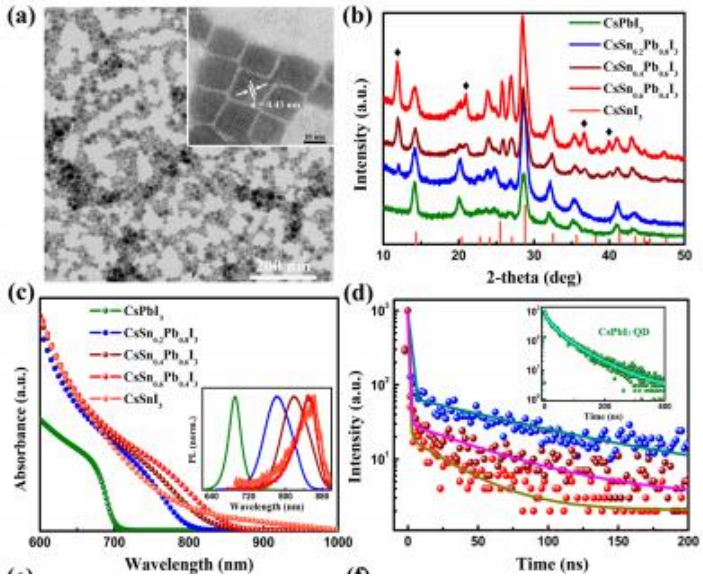

Figure 1.12 Stable $CsSn_{1-x}Pb_xI_3$ PNCs (a) TEM image, (b) XRD pattern of $CsSn_{1-x}Pb_xI_3$ PNCs with different chemical compositions, (c) UV-Vis absorption spectra and (e) time resolved PNCs. [63]

The superior stability of alloyed $CsSn_{1-x}Pb_xI_3$ PNCs is owing to improved oxidation stability of Sn instead of surface capped hydrophobic ligands. Detailed investigation of $CsSn_{1-x}Pb_xI_3$ PNCs indicated that significant improvement of oxidation stability is attributed to the increase in the bonding energy of Sn^{2+} in contrast to pure $CsSnI_3$ PNCs, shorter tin-iodine bond length as well as the introduction of Sn with smaller ionic radius than Pb ions into B sites, which results in the higher tolerance factor and eventually leading to enhancement of stability. [63]

Another advantage of lead halide PNCs in comparison to traditional semiconducting NCs is that lead halide PNCs exhibited readily morphology tunability. Unlike cadmium or lead based narrow band gap NCs, synthesis of NCs with different morphologies (e.g., nanorods and nano-sheets) was realized via the presence of long-chain hydrocarbon

amines, trioctylphosphine and trioctylphosphine oxide, serving as capping agents in combination with special long-chain phosphoric acid. [64-66] However, the morphologies of lead halide PNCs can be readily tuned from nanocubes, to nanoplates [67, 68] and to nanowires. [69, 70] with just varying the hot-injection temperature or reaction time (**Figure 1.13**). Lead halide PNCs also displayed tendency to couple with other uniform NCs to generate metal-semiconducting hybrid NCs with fast time resolved PL decay lifetime. [71]

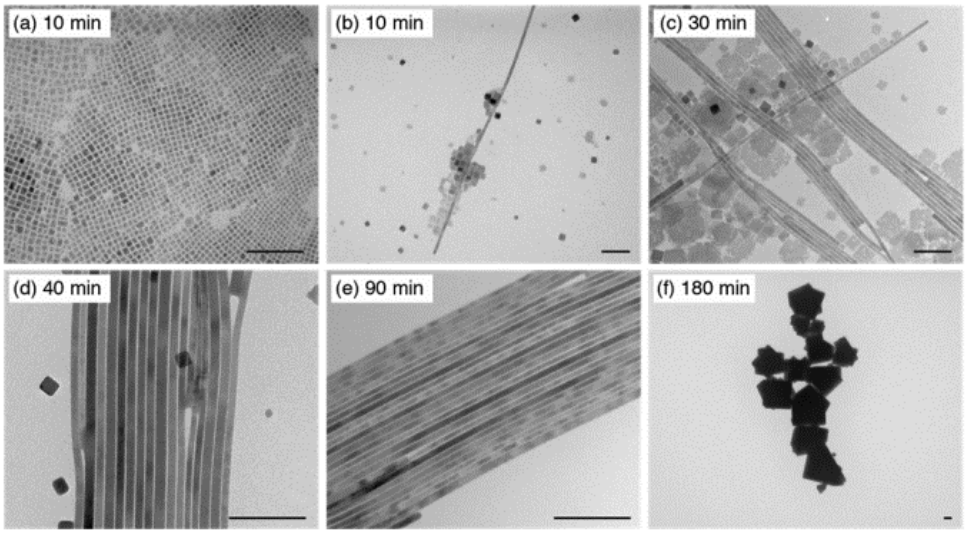

Figure 1.13 Shape evolution of as-synthesized cesium lead bromide NCs with different reaction time. [70]

Another reason for the wide application of PNCs in the state-of-the-art optoelectronic devices is their chemical composition versatility and structural tunability, which offer possibility to craft myriad of, virtually unlimited, perovskite materials with required band gap and stability. With the structure of ABX_3, perovskite materials are capable of replacing or doping with different elements at A, B or X sites. As mentioned above, anion exchange process enabled continuous tuning halide composition from Cl to Br and I with any ratio. [59] And the lead ions in B sites can be partially substituted with tin, thereby leading to the

decrease in the band gap. Manganese (Mn) doping in conventional semiconducting NCs resulted in spin-polarized d-d emission. Recently, Mn doping in B sites was demonstrated in cesium lead halide PNCs, resulting continuous and reversible variation of host energy gap from 1.8 to 3.1 eV without affecting NCs size and shape. [72] Moreover, Mn doping in PNCs was reported to help stabilize $CsPbI_3$ PNCs in cubic phase with almost same optical properties. [73] In addition, high level of Mn doping was also reported in the case of organic-inorganic lead halide PNCs (**Figure 1.14**), forming organolead halide PNCs with displacement of almost 90% Pb while preserving the unique excitonic emission of the PNCs with an additional orange emission of Mn^{2+} via energy transfer. [74] More interestingly, doping of lead halide PNCs can be achieved via heterovalent doping. Begum *et al.* demonstrated a modified hot injection method to obtain the doping of cesium lead halide PNCs with Bi^{3+} and illustrated the effect of this heterovalent doping on the modulation of the charge-carrier dynamics and energy level alignment at the interface of PNCs with different molecular acceptors. [75]

The most common cations located in A sites are methylammonium (MA), formamidinium (FA) and Cs. In fact, there are several other available organoammonium cations that can be used to dope in A sites. For instance, organoammonium cations with different length of carbon chains (e.g., ethylammonium and hexylammonium) were able to react with lead halide to give rise to two dimensional PNCs with enhanced chemical stability.

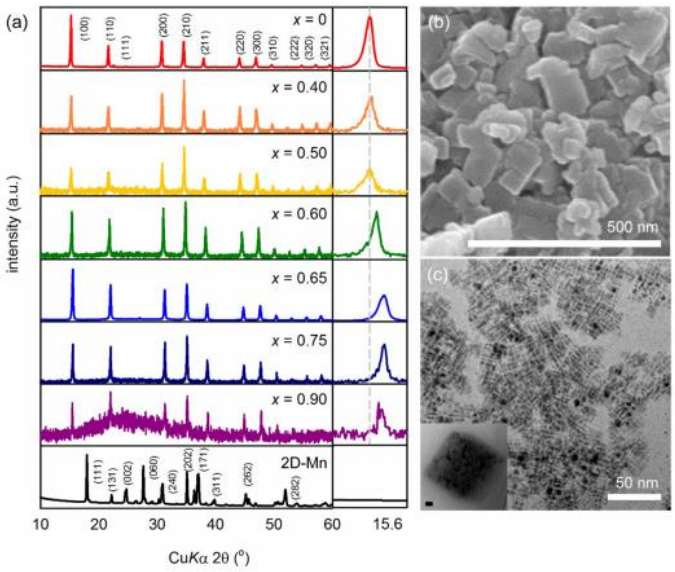

Figure 1.14 (a) XRD of 3D-$MAPb_{1-x}Mn_xBr_{3-(2x+1)}Cl_{2x+1}$ and 2D-MA_2MnCl_4 (2D-Mn) and (b) SEM and (c) TEM of 3D-$MAPb_{0.35}Mn_{0.65}Br_{0.7}Cl_{2.3}$. [74]

In contrast to conventional semiconducting NCs as well as all-inorganic PNCs prepared from hot injection method, organic-inorganic hybrid PNCs generally possessed relatively high NCs-size distribution. The possible reason for this high polydispersity of PNCs prepared from LARP can be explained by La Mer model. According to La Mer model, the size distribution of NCs prepared from hot injection method can be further narrowed down by Ostwald ripening process. After the injection of precursor solution into hot reaction vessel at high temperature, the colloidal solution (e.g., all-inorganic PNCs) was allowed to maintain at that temperature so that the size of NCs was increased with consumption of precursors from surrounding medium. During this process, Ostwald ripening process took place, causing the dissolution of small NCs and the growth of large NCs. However, the formation of organic-inorganic PNCs via LARP method is too fast to allow the occurrence of the Ostwald ripening process since the formation is usually complete within one second.

Although lead halide PNC, whether it be organic-inorganic or all-inorganic, exhibited several fascinating optical properties and short preparation process in contrast to the conventional semiconducting colloidal NCs, there are several problematic issues that impede their applications in photovoltaic devices. First, the highly ionic bonding in PNCs inevitably leads to the fact that PNCs are extremely sensitive to high polar solvents (e.g., methanol) and protic solvents (e.g., water). Trace amount of protic or polar molecules is sufficient to induce morphology or phase transformation and dimension change. In fact, any molecules that have propensity for dissolving or reacting with PNCs will destroy the structural integrity, causing the loss of photoluminescence and eventually PNCs decomposition. The structural fidelity of PNCs becomes even worsen in the case of organic-inorganic hybrid PNCs, especially considering that the organic ammonium cations (i.e., MA or FA) are able to rotate and vibrate in A sites. [76-78] Because of these rotational and vibrational movements, organic-inorganic hybrid PNCs generally exhibited lower stability compared to the all-inorganic counterparts with same chemical composition in B and X sites. And the low energy formation of organic-inorganic hybrid PNCs can eventually revert back to lead halide and volatile ammonium byproduct. [79] Moreover, this tendency of rotation and vibration movement was increased with increasing of the temperature, eventually causing the decomposition of organic-inorganic PNCs occurred at temperature much lower than that of all-inorganic PNCs. Since the temperature employed to craft all-inorganic PNCs via hot injection method may trigger the decomposition of organic-inorganic PNCs, the synthesis of hybrid PNCs is generally achieved via LARP method at *room temperature*. The conservation of structural integrity of all-inorganic PNCs can be realized via passivating with protective layer (e.g., silica coating and capping with

hyper branched small ligands), [80] giving rise to colloidal solution with enhanced stability (i.e., silica coated PNCs exhibited enhanced stability in the response to humid air and constant UV illumination and polyhedral oligomericmeric silsesquioxane capped PNCs even displayed resistance to anion exchange process [81]). Nonetheless, these protection strategies are hardly extended to the case of organic-inorganic PNCs due to the stringent requirements imposed by the structure of organic-inorganic perovskite (i.e., hybrid PNCs have poorer chemical stability compared to the all-inorganic PNCs). The chemical instability of lead halide PNCs can be demonstrated by the strong tendency for anion exchange. It was found that anion exchange process can even be initiated by mixing of cesium lead halide PNCs in dihalomethane solvents under the illuminating of 405 nm UV light owing to the generation of halide ions from dihalomethane molecules excited by photoinduced electron transferred from PNCs. [82] Another problem regarding to PNCs is that lead halide PNCs possessed a certain level of toxicity due to the presence of lead. This toxicity problem becomes pronounced especially considering the poor chemical stability of PNCs and can be mitigated, to some extent, via doping with non-toxic element or encapsulation in protection medium, including silica encapsulation and incorporation in polymer matrix.

1.2 Summary

The aforementioned information indicates that the growth of uniform semiconducting NCs (e.g., metal chalcogenides and perovskite NCs) is mediated by small molecules (e.g., oleic acid and oleylamine), leading to semiconducting NCs with spherical or rod-like morphologies. Unfortunately, uniform semiconducting NCs with novel morphology (i.e., hollow structure) or complex architecture (i.e., core/shell) have not yet

been reported because of the characteristics of semiconducting NCs and the fact that the small molecule ligands cannot function as effective morphology mediator to achieve these goals. Seldom have well-defined copolymers with complex architectures prepared by ATRP and click reaction been employed as morphology controller (i.e., nanoreactors) to achieve these goals. This disseration is dedicated to the investigation of precise molecular design of macromolecules and utilization of these macromolecules as nanoreactors to craft semiconducting NCs with novel morphology and complex architectures. The detailed motivations and goals are listed in chapter 2.

CHAPTER 2. MOTIVATION AND RESEARCH GOALS

2.1 Motivations

2.1.1 Challenges and Significance in Narrow Band Gap Semiconducting Metal Chalcogenides Nanocrystals with Novel Morphology

There are several theoretical studies with regard to the optical properties of semiconducting hollow metal chalcogenides nanostructured materials with negative curvature, predicting that the presence of negative curvature surface will cause the enlargement of optical band gap of hollow nanostructured materials. Previous theoretical modelling studies give an in-depth explanation for the blue-shifted in the UV-Vis absorption spectrum based on the well-established bond-order-length-strength correlation mechanism using local bond average approach. ***Unfortunately, this theoretical prediction has not been proved in the hollow metal chalcogenide nanocrystals below 50 nm with uniform hollow interior and shell thickness for the reason that there is no available synthetic approach for preparing semiconducting hollow metal chalcogenide nanocrystals with high quality, not to mention the narrow band gap hollow metal chalcogenide nanocrystals***. Conventional hollow nanocrystals preparation methods are very difficult to be extended to the case of semiconducting hollow metal chalcogenide nanocrystals. Moreover, classic synthesis of semiconducting metal chalcogenide nanocrystals based on the utilization of organophosphate as ligands requires delicate post-treatment approaches (i.e., ligand exchange process) to replace insulating ligands with conducting ligands, which is time-consuming and may damage the structural integrity of as-synthesized nanocrystals.

2.1.2 Challenges in Organolead Halide Perovskite Nanocrystals

Although organolead halide perovskite nanocrystals have been demonstrated various applications in LEDs, photodetectors, solar cells and high performance displays, one inherent issue impedes the further application of organolead halide perovskite nanocrystals is their chemical instability. The structural integrity of organolead halide perovskite nanocrystals can be easily destroyed exposure to the stimuli, such as high humid air, repetitive solvent washing, mixing with perovskite nanocrystals with different compositions and continuous ultra-violet illumination. ***Currently, there is no available synthetic route that can simultaneously improve perovskite nanocrystals stability in terms of colloidal stability, chemical composition stability, photostability and moisture stability***. Moreover, unlike conventional semiconducting NCs and all-inorganic PNCs, both of which can be fabricated with very low polydispersity via hot injection method and are able to self-assemble into large-are superlattice due to size monodispersity, ***the organic-inorganic hybrid PNCs prepared via LARP method have comparatively high polydispersity***.

2.1.3 Challenges in Core/Shell Nanocrystals with Large Lattice Mismatch

Core/shell nanocrystals with tunable core dimensions and shell thickness are a group of nano-hybrids, which not only combine the properties inherited from core and shell materials but also exhibits fascinating coupling effect owing to the intimate contact of core and shell materials. However, current synthetic routes to core/shell nanocrystals based on epitaxial growth mechanism fail to be extend to the scenarios in which the lattice mismatch of core and shell materials is large than 40%. Although there are a few synthetic strategies

based on non-epitaxial growth mechanism, showing the possibility of crafting core/shell nanocrystals with large lattice mismatch, the controllability of these methods in terms of size of core and shell thickness is rather poor, leading to the formation of core/shell nanocrystals with large size variation and non-uniform shell thickness. ***Accordingly, it is imperative to develop a facile and robust non-epitaxial synthetic approach for crafting core/shell nanocrystals with large lattice mismatch, good dimension controllability and tunable surface chemistry for the purpose of potential application in functional devices***.

2.2 Research Goals

The goal of this disseration is to develop an effective and robust synthetic strategy based on a series of judiciously designed 21-armed star-like triblock copolymers prepared from ATRP in conjunction with click reaction to address all the aforementioned issues and limitations encountered in conventional synthetic routes, thereby pushing the boundary of current available synthetic approaches, answering the in-depth question regarding to quantum chemistry, developing novel materials with enhanced properties and demonstrating the energy harvesting application of resulting novel nano-materials. To be more specific, in this dissertation, we address the following issues:

First, in chapter 3, we developed an unconventional amphiphilic star-like polystyrene-block-poly(acrylic acid)-block-polystyrene (PS-*b*-PAA-*b*-PS) and polystyrene-block-poly(acrylic acid)-block-poly(3,4-ethylenedioxythiophene (PS-*b*-PAA-*b*-PEDOT) triblock copolymers and demonstrated that hollow lead chalcogenide nanocrystals can be crafted via utilizing star-like triblock copolymers as nanoreactors. The main achievements and novelties of chapter 3 can be summarized as following bullets:

1. Amphiphilic star-like coil-*b*-coil-*b*-rod PS-*b*-PAA-*b*-PEDOT was rationally synthesized.
2. Star-like PS-*b*-PAA-*b*-PS and PS-*b*-PAA-*b*-PEDOT triblock copolymers were employed as nanoreactors to direct the growth of semiconducting hollow lead chalcogenide nanocrystals with tunable dimension of hollow interior and shell thickness, which were inaccessible to conventional methods.
3. Surface tethered insulating polymer ligands can be 100% substituted by semiconducting conjugated polymers without utilizing highly toxic and explosive chemical.
4. The blue-shift of absorption peak owing to the presence of negative curvature (i.e., hollow interior) was firstly confirmed by experiment.

Second, in chapter 4, we developed two series of poly(4-vinylpyridine)-*block*-poly(*tert*-butyl acrylate)-*block*-polyethylene oxide (P4VP-*b*-P*t*BA-*b*-PEO) and star-like poly(4-vinylpyridine)-*block*-poly(*tert*-butyl acrylate)-*block*-polystyrene) (P4VP-*b*-P*t*BA-*b*-PS) triblock copolymers and demonstrated that utilization of star-like triblock copolymers as nanoreactors render the preparation of polymer-capped silica-coated organolead halide perovskite nanocrystals possible. The main achievements and novelties of chapter 4 can be summarized as following bullets:

1. Star-like triblock copolymers was utilized as nanoreactors to dictate the growth of core/shell nanocrystals consisting of ***uniform*** perovskite nanocrystals as core, silica coating as shell-1 and polymer ligands as shell-2 with good dimension control and ***tunable surface chemistry*** which are inaccessible to conventional methods.

2. The resulting organolead halide nanocrystals exhibited excellent moisture stability, colloidal stability, photostability and chemical composition stability, which is a promising materials for the next generation of LED devices.

Third, in chapter 5, we developed a novel poly(4-vinylpyridine)-*block*-poly(*tert*-butyl acrylate)-*block*-oligomeric polyethylene oxide P4VP-*b*-P*t*BA-*b*-oligomeric PEO with the decreased length of PEO block and demonstrated that utilization of star-like triblock copolymers as nanoreactors was able to facilitate the formation of core/shell nanocrystals with large lattice mismatch. Surface capped short-chain oligomeric PEO not only endowed excellent colloidal stability to the resulting core/shell nanocrystals, thereby maintaining the solution processability, and did not block the carrier transportation but also conferred good chemical compatibility with organolead halide perovskite, thereby rendering the incorporation of core/shell nanocrystals into perovskite solar cell possible. The resulting perovskite solar cells incorporating core/shell nanocrystals also exhibited enhanced power conversion efficiency.

CHAPTER 3. UNCONVENTIONAL ROUTE TO UNIFORM HOLLOW SEMICONDUCTING NANOCRYSTALS WITH TAILORABLE DIMENSIONS, COMPOSITIONS, SURFACE CHEMISTRY, AND NEAR-INFRARED ABSORPTION

3.1 Introduction

In general, nanostructured materials can be classified into two categories based on the curvature of the presented surface: (1) nanostructured materials with only positively curved surfaces (e.g., nanosphere, [83] nanocube, [84] nanoprism [85] and nanorods [86]) and (2) nanostructured materials with positive curved surfaces and negatively curved surfaces (e.g., hollow nanoparticles [87] and nanotubes [88]). From the point of view of algebraic topology, nanostructured materials with negative curvature differ from materials with only positive curvature in a sense that the former ones cannot shrink into a single point whereas the latter ones can. Because of this, hollow nanocrystals (HNCs) with not only positive curvature but also negative curvature have attracted a great attention due to their much higher surface to volume ratio compared to their solid counterparts with the same dimension, which renders nanostructured materials with hollow interior promising candidates for applications including electronic, catalysis, energy harvesting and storage as well as biomedicine. [89] Previous studies showed that incorporation of HNCs into the thin film solar cells improved light trapping owing to the scattering light by HNCs, which was beneficial to light absorption and enhanced power conversion efficiency. Hollow metal oxide NCs were considered to be the advanced electrode materials for the next generation lithium ion battery owing to superior cycling performance originated from hollow

structures which can maintain the structural integrity during the lithiation and delithiation cycle. [90, 91]

Although considerable studies have been done on precise synthesis of inorganic colloidal NCs with tunable morphologies (i.e., zero-dimension, one-dimension and two-dimension), chemical composition (i.e., noble metal, metal oxide, metal sulfide and metal chalcogenide) and tailorable dimensions (i.e., size can be readily tuned from few nanometers to several hundred nanometers), these synthetic routes cannot be easily extended to HNCs systems. Accordingly, the synthetic approach for the preparation of HNCs with negatively curved hollow interior and positively curved outer surface had been explored by several research groups in depth. Based on the different hollow interior formation mechanism, conventional synthetic routes to HNCs can be mainly divided into four groups: HNCs prepared from the nanoscale Kirkendall effect, [92-94] hollow interior formed via galvanic replacement reaction, [95, 96] preferential chemical etching of core materials to produce HNCs [97, 98] and template-mediated approach based on the self-assembly of small molecule or linear polymers to direct the growth of hollow nanostructures. Unfortunately, there are still inherent limitations which restrict the general applicability of these methods.

One of the well-established synthetic route to HNCs is to utilize the nanoscale Kirkendall effect in which the migration of nanoscopic atom boundary takes place as the consequence of differential atom diffusion rate. The net result of this atomic motion gives rise to the formation of hollow interior. To be more specific, this process usually involved the preparation of transition metal NCs (i.e., iron or cobalt NCs) followed by introduction of oxygen in high boiling point organic solvents (e.g., octadecane) and solvent-annealing

at high temperature (i.e., higher than 200 °C). The dissolved oxygen first reacted with metal atom at the surface of metal NCs to yield amorphous metal oxide shell (i.e., metal/amorphous metal oxide core/shell NCs) and the oxygen atoms in amorphous metal oxide shell diffused into metal core NCs while metal atoms diffused outward. Outward diffusion of metal atoms generated nanopores due to the higher diffusion rate of metal atoms in comparison to oxygen atoms (i.e., Kirkendall effect). As this process kept going on, the fusion of these nanopores eventually formed well-defined hollow interior with spherical shape and the metal NCs transformed into metal oxide HNCs. Although this approach has proved to be a very powerful and facile strategy for preparing HNCs, there are several limitations associated with this method. One of the disadvantage regarding to this method is the material availability. Since the hollow formation mechanism of this method is predicated on Kirkendall effect, it requires that the atoms in core of NCs possess higher diffusion rate than the introduced atoms in the shell domain. Otherwise, only solid metal compound NCs will be produced. Accordingly, this prerequisite restricts the general applicability of this method. Currently, these method is mainly used to prepare transitional metal oxide (e.g., iron oxide or cobalt oxide HNCs) or transitional metal sulfides and selenides HNCs. Moreover, precise tuning the core size, shell thickness and chemical composition of HNCs are still not fully decoupled, leading to the fact that these parameters are usually interdependent with each other and the whole diffusion process can be complicated by factors, including annealing and reaction temperature, atom diffusion rate, chemical composition profile and specific geometry. [99] For instance, high temperature was necessary to initiate the diffusion of oxygen atoms into metal NCs core for precisely controlling the dimension of hollow interior and shell thickness. In order to maintain the

uniform core size and shell thickness, iron NCs were oxidized to Fe_3O_4 HNCs instead of Fe_2O_3 HNCs. Also, this approach involves the synthesis of sacrificial core NCs first followed by post-synthetic treatment to produce hollow interior. Therefore, the morphologies of resulting HNCs are largely dependent upon the dimension of sacrificial NCs. Thus, independent tuning the morphologies of HNCs and tailoring the chemical composition of HNCs are still considered to be a highly challenging task. Consequently, this synthetic approach is largely limited to the synthesis of metal oxide, [100] metal sulfides and selenides HNCs. [101]

Another well-established synthetic route applied to colloidal synthesis of HNCs involves performing galvanic replacement reaction *in-situ* on the surface of solid NCs, [102] which is an effective self-templating method for preparing noble metal HNCs bearing complex architecture and well-controlled hollow nanostructure. Classical noble metal HNCs prepared by galvanic replacement reaction commonly followed a process in which noble metal solid NCs (e.g., silver NCs) with lower reduction potential were synthesized first followed by the introduction of targeted metal precursor (e.g., $HAuCl_4$) with higher reduction potential. The introduced metal precursor was reduced on the surface of pre-synthesized solid NCs to form shell while solid NCs were oxidized and dissolved, leading to the formation of hollow interior. Unfortunately, although galvanic replacement reaction has also extended to the synthesis of metal oxide HNCs, [103] there are also some limitations associated with it. First, this approach is mainly limited to the synthesis of noble metal HNCs, especially for gold HNCs (e.g., hollow nanoparticles and nanocages) despite of the fact that a few transitional metal oxide HNCs (e.g., iron oxide and manganese oxide) can be also synthesize via this strategy. [103] Second, fabrication of noble metal HNCs via this

method has to rely on the utilization of noble metal solid NCs with lower reduction potential as the starting material. The standard reduction potentials of common metals at 298 K under one atmosphere are summarized in **Table 3.1**.

Table 3.1 Standard reduction potentials of metals in increasing order.

Half Reaction	**E^0(V)**
$Sr^+ + e^- \rightleftharpoons Sr$	-4.01
$Ca^+ + e^- \rightleftharpoons Ca$	-3.80
$Li^+ + e^- \rightleftharpoons Li$	-3.04
$Cs^+ + e^- \rightleftharpoons Cs$	-3.02
$K^+ + e^- \rightleftharpoons K$	-2.93
$Na^+ + e^- \rightleftharpoons Na$	-2.71
$Mg^{2+} + 2e^- \rightleftharpoons Mg$	-2.37
$Be^{2+} + 2e^- \rightleftharpoons Be$	-1.84
$Ti^{3+} + 3e^- \rightleftharpoons Ti$	-1.37
$Zn^{2+} + 2e^- \rightleftharpoons Zn$	-0.76
$Fe^{2+} + 2e^- \rightleftharpoons Fe$	-0.44
$Ni^{2+} + 2e^- \rightleftharpoons Ni$	-0.25
$Pb^{2+} + 2e^- \rightleftharpoons Pb$	-0.13
$Ge^{4+} + 4e^- \rightleftharpoons Ge$	+0.12
$Bi^{3+} + 3e^- \rightleftharpoons Bi$	+0.38
$PtCl_4^{2-} + 2e \rightleftharpoons Pt + 4Cl^-$	+0.758
$Ag^+ + e^- \rightleftharpoons Ag$	+0.80
$Hg^{2+} + 2e^- \rightleftharpoons Hg$	+0.85
$Pd^{2+} + 2e^- \rightleftharpoons Pd$	+0.915
$AuCl_4^- + 3e^- \rightleftharpoons Au + 4Cl^-$	+0.93
$Pt^{2+} + 2e^- \rightleftharpoons Pt$	+1.19
$Au^{3+} + 3e^- \rightleftharpoons Au$	+1.52
$Au^+ + e^- \rightleftharpoons Au$	+1.83

As can be seen from **Table 3.1**, the solid metal NCs serving as sacrificial template

during galvanic replacement reaction should have lower reduction potential compared to the final targeted metal HNCs. Because of this requirement, the preparation of metal HNCs with very low reduction potential is considered to be very challenging for the reason that solid metal NCs with even lower reduction potential have to be synthesized first and serve as sacrificial template. This is principle reason why this synthetic strategy is primarily targeting for the fabrication of a limited set of noble metals or metal alloys. Although this method is successfully extended to the fabrication of transitional metal oxide HNCs with enhanced LIB performance and noble metal HNCs bearing complicated hollow architecture with superior surface enhanced Raman properties, morphologies of the hollow structure of the resulting HNCs may undergo pronounced change in comparison to pre-synthesized solid metal NCs serving as sacrificial template after galvanic replacement reaction. Last but not least, dissolution of sacrificial template and deposition of targeted metal inevitably produce HNCs with shell composed of metal alloy as opposed to be single-component metal, which hinders the in-depth investigation of plasmatic property or surface enhanced Raman spectroscopy of pristine noble metal HNCs. Admittedly, this metal alloy HNCs can be selectively transformed into single-component HNCs via dealloying process. Nonetheless, dealloying process usually tends to cause the morphological reconstruction. [104]

Preferential chemical etching, or partial dissolution of the nanocrystal interior while keeping its shell intact, is another feasible and versatile approach to prepare HNCs with well-controlled hollow interior. However, this method is largely directed to the synthesis of metal oxide HNCs and usually requires high temperature to induce etching process. [105] Moreover, the high temperature necessary for allowing conversion of the solid NCs into

HNCs inevitably caused morphology change or shape distortion. Obviously, it is difficult to perform this high temperature etching process on NCs with relatively low stability, such as organolead halide perovskite NCs or narrow band gap metal chalcogenides NCs, both of which have strong tendency to react with water or oxygen in the air. Another problematic issue regarding to preferential etching is that the regent used in this process is highly material-specific. As a result, this approach is generally limited to transition metal oxide. [97, 106, 107]

Furthermore, although template-mediated approach is effective in preparation of various HNCs, the drawbacks of this method, whether it be hard or soft, are not negligible. In the case of hard template approach, availability of template and homogeneous nucleation during coating process render it difficult to control the morphology of the final product in a reproducible manner and post-treatment required to remove template can be a major impedance. [89] For instance, silica nanoparticles prepared from Stober method are one of the most widely used hard template for making various hollow nanostructures with enhanced LIB performance or even multi-shell structures. However, the size of these hollow structure is usually larger than 50 nm because Stober method cannot produce silica nanoparticles less than this size. Moreover, the removal of silica nanoparticles after the growth of shell usually involves the usage of hydrofluoric acid which is very toxic and dangerous. Under some very special circumstances, hollow nanostructures with high-quality can be synthesized from the self-assembled superstructures formed via the small molecules or linear block copolymers. Unfortunately it is still a challenge task to exploit soft template method (e.g., amphiphilic small molecular or linear block copolymers) to precisely tailor-make hollow structures for the reason that the self-assembled structures

formed by soft templates are sensitive to several factors, such as pH value, temperature, solvent, introduction of metal precursors, etc. and can be easily destroyed by these factors. [108, 109] This is primary reason why the preparation of hollow structures via soft template method is generally material specific.

Narrow band gap colloidal lead chalcogenides NCs are of particular interest for application in solar cells, [110] thermoelectric devices [111] and photodetector [112] due to their widely size-tunable property from the visible to near-IR regime. Traditional synthetic strategies are proved to be powerful way to prepare various HNCs. Nevertheless some inherent limitations associated with these traditional methods give rise to a synthetic dilemma that it is still a very challenging task to extend these strategies to the narrow band gap lead chalcogenides HNCs. The nature of lead chalcogenides NCs (i.e., sensitive to air and water) further aggravates this situation. For instance, most synthetic strategies for preparing lead chalcogenides solid NCs (e.g., PbTe) have to rely on the alkylphosphine ligands (e.g., trioctylphosphine (TOP), trioctylphosphine oxide (TOPO) and tributyl phosphate (TBP)) because of poor solubility of tellurium in most of solvents, [38] leading to NCs with only positive curvature (i.e., spherical or cubic shape). [48-50]

The previous information regarding the conventional HNCs synthetic routes indicates that although there is tremendous advancement of synthesis of colloidal metal oxide or noble metal HNCs with decent morphology control, there is no synthetic approach for crafting colloidal semiconducting HNCs with precise size, morphology and surface chemistry control, not to mention the narrow band gap lead chalcogenides HNCs with negative curvature, due to some inherent limitations associated with aforementioned traditional HNCs synthetic methods. Theoretical modeling indicates that the presence of

negative curvature via formation of hollow interior in nanostructured semiconducting materials offers another route to tailor the size-dependent property of materials (e.g., optical band gap). [113, 114]

To the best of our knowledge, for the first time, we develop an unconventional synthetic approach to obtain semiconducting lead chalcogenides (e.g., PbTe and PbS) HNCs below 15 nm with excellent core and shell thickness control via utilizing a series of well-defined 21-arm star-like triblock copolymers (e.g., polystyrene-*block*-poly acrylic acid-*block*-polystyrene (PS-*b*-PAA-*b*-PS) and polystyrene-*block*-poly acrylic acid-*block*-poly(3,4-ethylenedioxythiophene) (PS-*b*-PAA-*b*-PEDOT)) as nano-reactors. 21-arm star-like macromolecules crafted via atom transfer radical polymerization (ATRP) in conjunction with click reaction and Grignard metathesis polymerization (GRIM) circumvent issues regarding semiconducting HNCs prepared by conventional approaches, thereby producing lead chalcogenides NCs with hollow structure. In contrast to conventional methods, this synthetic strategy not only offers an alkylphosphine-free synthesis of PbTe and PbS HNCs (i.e., reaction in the absence of TOP, TBP or TOPO), but also enables a feasible, one-pot hydrazine-free and tunable surface chemistry (e.g., surface capping ligand can be readily varied from insulating PS to conjugated semiconducting PEDOT). Furthermore, this study reports the blue-shift of the absorption spectrum of HNCs compared to their solid counterparts with same outer diameter due to the presence of hollow interior with negative curvature, which is consistent with a model based on the well-established bond-order-length-strength (BOLS) correlation mechanism using local bond average approach (LBA). [114]

3.2 Experimental details

3.2.1 Materials

Toluene (99.5%), dichloromethane (>99.5), anisole (99%), 2-butanone (99.0%), N,N-dimethylformamide (DMF, >99.8%), benzyl alcohol (BA, >99.0%), trichloroethylene (99.0%), anhydrous ethanol (>99.5%), anhydrous 1-methyl-2-pyrrolidinone (NMP, 99.5%), anhydrous hexane (95%), N,N,N',N',N''-pentamethyldiethylene triamine (PMDETA, 99%), 2,2'-bipyridyl (bpy, >99%), 2,5-dibromo-3,4-ethylenedioxythiophene (EDOT, 97%), α-bromoisobutyryl bromide (99%), tert-butylmagnesium chloride (1.0 M solution in tetrahydrofuran), ethynylmagnesium bromide (0.5 M solution in tetrahydrofuran), sodium azide (>99.5%), trifluoroacetic acid (TFA, 99.9%), lead(II) nitrate(Pb(NO3)2, >99.0%), tellurium powder (99.99%), sodium borohydride powder (>98.0%), hexamethyldisilathiane (reagent grade, >99.0%) were purchased from Sigma-Aldrich and used as received.

β-Cyclodextrin (β-CD, >97.0%, Sigma-Aldrich) was recrystallized twice from water, and dried under vacuum for 48 h at 50□C. The traces of water were removed by azeotropic distillation in toluene for 2 h at 110□C prior to the bromination reaction. Copper(I) bromide (CuBr, 98%, Sigma-Aldrich) was stirred overnight in acetic acid, filtered, rinsed with ethanol and diethyl ether successively, and dried in vacuum overnight. Styrene (St, Sigma-Aldrich) and tert-Butyl acrylate (tBA, Sigma-Aldrich) were distilled over CaH2 under reduced pressure prior to use. Tetrahydrofuran (THF, 99%) was stirred over sodium pellets and distilled from sodium naphthalenide. [1,3-bis(diphenylphosphino)propane] dichloronickel-(II) was dried under vacuum for 24 h prior to Grignard metathesis reaction. All other reagents were purified by common purification procedure.

3.2.2 Star-like copolymers synthesis

Synthesis of Heptakis[2,4,6-tri-O-(2-bromo-2-methylpropionyl]-β-cyclodextrin) (i.e., 21Br-β-CD macroinitiator) Azeotropically distilled β-CD (5.683 g, 5 mmol) was dissolved in 80 mL anhydrous NMP and cooled to 0°C. α-Bromoisobutyryl bromide (48.279 g, 210 mmol) was added to the β-CD solution under magnetic stirring from a dropping funnel in 15 min. The reaction temperature was kept at 0°C for 2 h, and then gradually increased to ambient temperature. The reaction solution was maintained at ambient temperature for 22 h for complete bromination reaction. The brown solution was transferred to a separation funnel and diluted with 100 mL dichloromethane. The resulting solution was washed sequentially with saturated $NaHCO_3$ aqueous solution and DI water until the pH was above 4.5. The product was retrieved from the resulting solution by rotary evaporation, re-dissolved in acetone, and precipitated in cold water three times to remove other impurities. The precipitant was re-dissolved in dichloromethane, and dried with anhydrous $MgSO_4$. The final product was obtained by removing solvent by rotary evaporation.

Synthesis of Star-like Homopolymer PS (i.e., Star-like PS-Br) by ATRP Using 21Br-β-CD as Macroinitiators. Polymerization of styrene (St) was performed by exploiting 21Br-β-CD with 21 initiation sites as macroinitiator. An ampoule charged with 21Br-β-CD (0.05 g), CuBr (0.035 g), bpy (0.1539 g) and St (40 mL) underwent three freeze-pump-thaw cycles in liquid N_2 and then placed in an oil bath at 90°C for a desired time. The polymerization process was stopped by quenching in liquid N_2 and exposing to air. The crude product was diluted with THF and passed through a neutral alumina column

to remove copper salt. The resulting solution was concentrated by rotary evaporation and precipitated in cold methanol, yielding a white powder. The products were further purified by the dissolution/precipitation method using THF/cold methanol twice to remove unreacted monomer and then dried at 40°C under vacuum.

Synthesis of Star-Like PS-*b*-P*t*BA (i.e., Star-like PS-*b*-P*t*BA-Br) by ATRP Using Star-Like PS-Br as Macroinitiators. All chain extension reactions with *t*BA using well-defined star-like PS synthesized above as macroinitiators were performed in an ampoule. The reaction mixture consisting of *t*BA, star-like PS, CuBr, PMDETA (molar ratio=800:1:1:2) in anisole (1 mL *t*BA in 1 mL solvent) were degassed by three freeze-pump-thaw cycles in liquid N_2 and then placed in oil bath preheated to 60°C. The polymerization was stopped by immersing in liquid N_2 and then exposing to air. The crude product was diluted with THF and passed through a neutral alumina column to remove copper catalyst. The resulting product was further purified by fractional precipitation using water/methanol mixture with a volume ratio of 1:1 to remove unreacted monomers. The resulting powder-like star-like PS-*b*-P*t*BA-Br was further purified by fractional precipitation using acetone as solvent and water/methanol mixture with a volume ratio of 1:1 as precipitator to separate star-like PS-*b*-P*t*BA-Br from the residual linear P*t*BA, and then dried at 40°C under vacuum to obtain pure star-like PS-*b*-P*t*BA-Br for the following chain extension reaction described below.

Synthesis of Star-Like PS-*b*-P*t*BA-*b*-PS (i.e., Star-like PS-*b*-P*t*BA-*b*-PS-Br) by ATRP Using Star-Like PS-*b*-P*t*BA-Br as Macroinitiators. Synthesis of star-like PS-*b*-P*t*BA-*b*-PS using star-like PS-*b*-P*t*BA as macroinitiator was performed in an ampoule. The reaction mixture consisting of St, star-like PS-*b*-P*t*BA, CuBr, PMDETA (molar

ratio=1000:1:1:2) in anisole (1 mL St in 1 mL solvent) were degassed by three freeze-pump-thaw cycles in liquid N_2 and then placed in oil bath preheated to 90°C for a desired time. The reaction was stopped by immersing in liquid N_2 and then exposing to air. The crude product was diluted with THF and passed through a neutral alumina column to remove copper salt. The resulting product was purified by dissolution/precipitation using THF/cold methanol twice to remove unreacted St and low molecular weight of linear PS due to high temperature. The final product was dried at 40°C under vacuum.

Synthesis of Star-Like P*t*BA-*b*-PS (i.e., Star-like P*t*BA-*b*-PS-Br) by ATRP Using 21Br-β-CD as Macroinitiators. Star-Like P*t*BA-*b*-PS diblock copolymers were prepared by similar way as star-like PS-*b*-P*t*BA-*b*-PS via sequential ATRP using 21Br-β-CD as macroinitiators.

Synthesis of Linear PS-*b*-P*t*BA-*b*-PS. Linear PS-*b*-P*t*BA-*b*-PS triblock copolymers were synthesized by sequential ATRP using α-bromoisobutyryl bromide as initiator.

Synthesis of Amphiphilic Star-Like PS-*b*-PAA-*b*-PS by Hydrolysis of Star-Like PS-*b*-P*t*BA-*b*-PS. In a typical process, star-like PS-*b*-P*t*BA-*b*-PS triblock copolymers obtained above (200 mg) were dissolved in 20 mL dichloromethane and TFA (the molar ratio of TFA to *t*BA in star-like copolymer = 10:1) was added into the reaction solution. The reaction solution containing star-like PS-*b*-P*t*BA-*b*-PS triblock copolymers, dichloromethane and TFA was kept stirring for 24 h at ambient temperature. After hydrolysis, the white product was precipitated on the bottom of flask. The product was retrieved by rotary evaporation to remove excess TFA, yielding white powder-like product.

To further purify the resulting star-like copolymers, the product was re-dissolved in a small amount of DMF and precipitated in cold methanol, followed by centrifugation at 13,000 rpm for 5 min and drying under vacuum at ambient temperature.

Synthesis of Amphiphilic Star-Like PAA-*b*-PS by Hydrolysis of Star-Like P*t*BA-*b*-PS. Star-like PAA-*b*-PS diblock copolymers were prepared in a similar way as star-like PS-*b*-PAA-*b*-PS described above.

Synthesis of Amphiphilic Linear PS-*b*-PAA-*b*-PS by Hydrolysis of Linear PS-*b*-P*t*BA-*b*-PS. Linear PS-*b*-PAA-*b*-PS triblock copolymers were prepared in a similar way as star-like PS-*b*-PAA-*b*-PS described above.

Synthesis of Star-Like Azide-Functionalized PS-*b*-P*t*BA (i.e., Star-like PS-*b*-P*t*BA-N_3). Pure star-like PS-*b*-P*t*BA-Br (0.5 g) was dissolved in DMF (10 mL) and sodium azide (Br in star-like PS-*b*-P*t*BA-Br : sodium azide =1:50) was added to the reaction solution. After reaction for 24 h at ambient temperature, the reaction solution was diluted with toluene. The product was purified by dissolution in THF and precipitation using cold water and methanol with volume ratio of 1:1 twice to remove excess NaN_3. The crude product was then re-dissolved in chloroform and washed with DI water for three times, followed by precipitation in water-methanol and drying at ambient temperature under vacuum.

Synthesis of Ethynyl-Terminated PEDOT by Grignard Metathesis Reaction (i.e., PEDOT-≡). In a typical synthesis, 2,5-dibromo-3,4-ethylenedioxythiophene (1.499 g, 5 mmol) dissolved in freshly dried THF (30 mL) was added in a dry 100 mL one-neck flask purged with ultra-pure argon. *Tert*-butylmagnesium chloride (5 mL, 5 mmol) was

added dropwise into the reaction solution. The reaction solution was kept stirring for 4 h at ambient temperature. The solution was then diluted with 30 mL dried THF, followed by the addition of dried Ni(dppp)Cl_2 (45 mg, 0.082 mmol). The resulting solution was stirred for 2 h at ambient temperature, leading to the formation of dark blue color of the reaction mixture. Ethynylmagnesium bromide (4 mL, 2mmol) was added into the reaction solution and allowed to react for 2 h. After precipitating the reaction solution in cold methanol, filtration and Soxhlet extraction with methanol for seven days were performed to obtain pure ethynyl-terminated PEDOT.

Synthesis of Star-Like PS-*b*-P*t*BA-*b*-PEDOT by Click Reaction. Briefly, star-like PS-*b*-P*t*BA-N_3 (100 mg) and PEDOT-≡ (200 mg) were dissolved in anhydrous DMF (20 mL) and transferred into an ampoule under argon protection. Three freeze-pump-thaw cycles were performed prior to the addition of CuBr (35 mg) and PMDETA (85 mg). The reaction solution was kept stirring at 90°C for seven days to ensure the completion of click reaction. The resulting dark product was diluted with a mixed solvent of DMF and chloroform (the volume ratio of DMF to chloroform = 1:10) and passed through an alumina column to remove the transition metal catalysts. The linear PEDOT in the solution was eliminated by fractional precipitation for three times. The resulting star-like copolymers were further purified by precipitation in cold methanol and dried in a vacuum oven for 24 h.

Synthesis of Star-Like PS-*b*-PAA-*b*-PEDOT by Hydrolysis of Star-Like PS-*b*-P*t*BA-*b*-PEDOT. Star-like PS-*b*-P*t*BA-*b*-PEDOT triblock copolymers (200 mg) were dissolved in 200 mL dichloromethane, followed by the addition of 5 mL TFA. The reaction

solution was kept stirring at 40°C for 24 h. The product was retrieved by precipitation in cold methanol. The amphiphilic star-like copolymers were further purified by the dissolution/precipitation twice using DMF/cold methanol to remove residual TFA in the copolymer and dried under vacuum at 40°C overnight.

Synthesis of PbTe HNPs Capped with PS and PEDOT on the Surface as the Stabilizing Ligands. The synthesis of polymer-capped PbTe HNPs was performed in a standard Schlenk line. The preparation of PbTe precursors was adapted from the published method with modification.[115] In a typical synthesis, Te powder (25.5 mg, 0.2 mmol) and $NaBH_4$ (151.3 mg, 4 mmol) were added into a Schlenk flask under argon protection. 10 mL DI water was added into flask and cooled to 0°C. The disappearance of dark Te powder and the formation of clear solution indicated the complete reaction of reagents after stirring at 0°C for 1.5 h. $Pb(NO_3)_2$ (66.2 mg, 0.2 mmol) was dissolved in 5 mL DI water and added dropwise into the reaction mixture. The instant appearance of dark product was the evidence of the formation of PbTe precursors. After stirring for 2 h, the PbTe precursors were retrieved by centrifugation and purified by washing with the mixture of methanol and DI water for three times. The residual water was removed by further washing with methanol. As the PbTe precursors can be easily oxidized, the resulting dark product was quickly transferred into a vacuum oven and dried at room temperature for 20 min prior to the PbTe HNPs synthesis.

For synthesis of PS-capped PbTe HNPs, the PbTe precursors and star-like PS-*b*-PAA-*b*-PS nanoreactors (10 mg) were dissolved in solution consisting of DMF (9 mL) and BA (1 ml) and transferred into a three-neck flask. The mixture solution consisting of DMF,

PbTe precursors and star-like tri-block copolymers was deoxygenated by argon bubbling and stirred at ambient temperature under argon protection for 2 h to ensure the diffusion and sufficient loading of precursors into the PAA regime. The reaction mixture was heated at 160°C with a constant heating rate of 3°C/min and then kept at that temperature for 6 h, yielding a homogeneous dark-brown colloidal solution. To isolate and purify the resulting PbTe HNPs colloidal solution, the crude reaction solution was first mixed with an equal volume of ethanol, followed by centrifugation. A black pellet of PbTe HNPs was formed on the bottom of centrifuge tube by pouring off the supernatant solution. The precipitant was re-dissolved in toluene or hexane, followed by centrifugation twice. After this, a stable colloidal solution was obtained by re-dissolving PbTe HNCs in various common organic solvents.

In order to synthesize PEDOT-capped PbTe HNPs, the same procedure was employed by replacing star-like PS-*b*-PAA-*b*-PS with star-like PS-*b*-PAA-*b*-PEDOT.

Synthesis of PbS HNPs Capped with PS on the Surface as the Stabilizing Ligands. In addition to PbTe HNPs, the star-like triblock copolymer nanoreactor strategy can be readily extended to synthesize PbS HNPs in a standard Schlenk line. In a typical synthesis, star-like PS-*b*-PAA-*b*-PS (10 mg) were dissolved in a mixed solvent consisting of DMF (9 mL) and benzyl alcohol (1 mL), and quickly transferred into a three-neck flask under argon purging. The resulting solution was deoxygenated by argon bubbling, followed by addition of $Pb(NO_3)_2$ (66.2 mg, 0.2 mmol). The residual water was further removed by heating the solution to 140°C under argon purging. The nucleation of PbS nanocrystals was initiated by the injection of hexamethyldisilathiane, followed by refluxing at 140°C,

producing a dark brown homogeneous colloidal solution. The isolation and purification of PS-capped PbS HNPs was same as that of PbTe HNPs described above.

Synthesis of PbS Solid NPs Capped with PS on the Surface as the Stabilizing Ligands. Synthesis of PbS solid NPs were prepared in a similar way as PbS HNPs using star-like PAA-*b*-PS diblock copolymers as nanoreactors instead of star-like PS-*b*-PAA-*b*-PS triblock copolymers.

3.2.3 Characterizations

The molecular weight of polymers was measured by gel permeation chromatography (GPC), equipped with an Agilent1100 with a G1310A pump, a G1362A refractive detector, and a G1314A variable wavelength detector. THF was used as the eluent at 1.0 mL/min at 35°C. One 5-μm LP gel column (500 Å, molecular range: $500-2\times10^4$ g/mol) and two 5-μm LP gel mixed bed columns (molecular range: $200-3\times10^6$ g/mol) were calibrated with the PS standard samples. ^{1}H nuclear magnetic resonance (^{1}H NMR) spectra were acquired using a Bruker 400MHz spectrometer with the solvent resonances as the internal standard. D-chloroform was used as solvent. Fourier transform infrared (FTIR) spectra were obtained using a Fisher Thermo Scientific Nicolet 6700 spectrometer equipped with an Ever-Glo source. The morphologies of and SAED patterns of HNPs were characterized by transmission electron microscopy (TEM) (JEOL TEM 100CX; operated at 100kv). The energy-dispersive X-ray (EDX) analysis of samples was obtained by scanning electron microscopy (SEM, LEO 1530, ZEISS & Hitachi SU8230). UV-Vis-NIR spectra were recorded using a Shimadzu UV-2600 and Cary 500 UV-Vis-

NIR spectrophotometers. X-ray diffraction profiles were collected using X'pert PRO (XRD, Netherlands).

3.3 Results and discussion

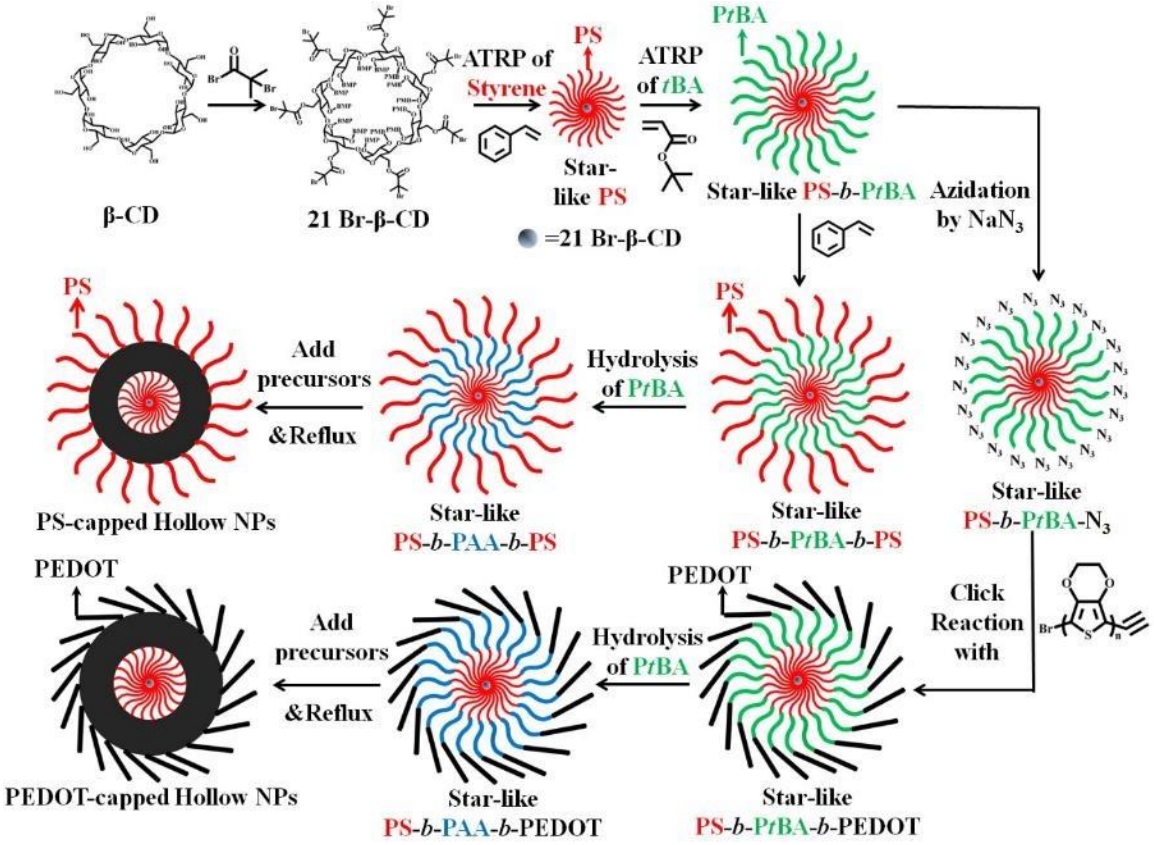

Figure 3.1 Stepwise representation of crafting narrow band-gap hollow nanocrystals (HNCs) with tunable dimensions and surface chemistry (i.e., PS-capped HNCs, central first panel; and PEDOT-capped HNCs, lower first panel) prepared by utilizing amphiphilic star-like PS-*b*-PAA-*b*-PS (coil-coil-coil) or PS-*b*-PAA-*b*-PEDOT (coil-coil-rod) triblock copolymers, respectively, as nanoreactors.

Figure 3.1 displays schematic illustration of synthetic approach to narrow band-gap lead chalcogenide HNCs capped with insulating PS and conjugated PEDOT as ligands via utilizing amphiphilic 21-arm star-like PS-*b*-PAA-*b*-PS (coil-*b*-coil-*b*-coil) triblock

copolymers prepared by sequential ATRP and star-like PS-*b*-PAA-*b*-PEDOT (coil-*b*-coil-*b*-rod) triblock copolymers synthesized via sequential ATRP in conjunction with click reaction as nanoreactors. In order to serve as effective nanoreactors to direct the growth of lead chalcogenide HNCs, star-like triblock copolymers are expected to possess enough number of arms in the space so that they are able to load metal precursors from reaction medium. Nearly 100% conversion of hydroxyl groups on β-CD to ATRP initiation sites through the esterification reaction between β-CD and α-bromoisobutyryl bromide was confirmed by ^{1}H NMR (**Figure 3.2**), indicating that the resulting brominated β-CD (denoted as 21Br-β-CD) was suitable for yielding 21-arm star-like copolymers. Based on our experience, we found that low bromination efficiency gave rise to low arm number of star-like copolymers (i.e., less than 21 arms) and eventually leaded to the formation of NCs with large size variation even if the total molecular weight of star-like triblock copolymers had very narrow distribution. In other words, enough arm density enabled the synthesis of uniform colloidal HNCs.

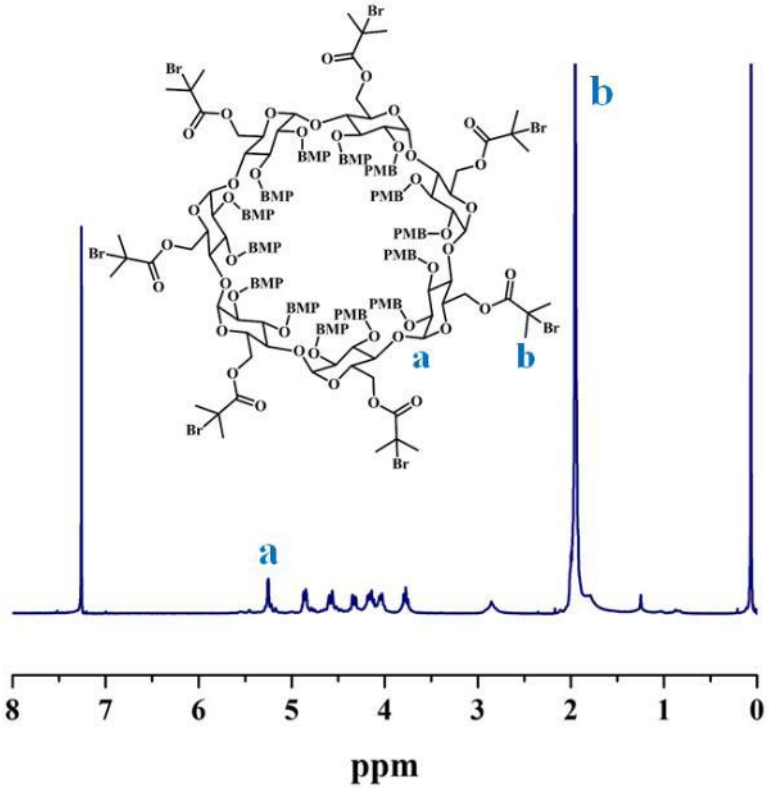

Figure 3.2 ^{1}H NMR spectrum of macroinitiator, that is, heptakis[2,3,6-tri-O-(2-bromo-2-methylpropionyl]-β-cyclodextrin (denoted 21Br-β-CD).

A series of star-like polystyrene-*block*-poly(*tert*-butyl acrylate)-*block*-polystyrene (PS-*b*-P*t*BA-*b*-PS) triblock copolymers with varied length (i.e., varied molecular weight) for different blocks were prepared by sequential ATRP of styrene (St), *tert*-butyl acrylate (*t*BA) and St using 21Br-β-CD as macroinitiator. Successful preparation of 21-arm star-like triblock copolymers upon which the nucleation and subsequent growth of lead chalcogenide HNCs depends was confirmed by proton NMR, showing characteristic peaks originating from PS block and P*t*BA block, respectively (**Figure 3.3**).

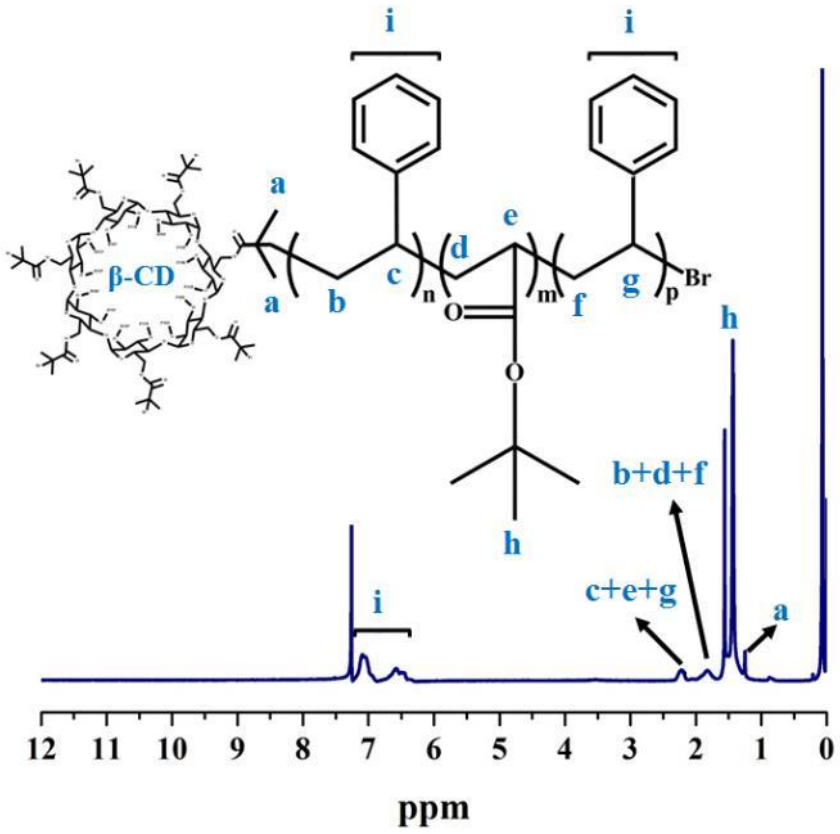

Figure 3.3 ^{1}H NMR spectrum of star-like PS-*b*-P*t*BA-*b*-PS in d-chloroform.

All obtained star-like polymers (e.g., star-like PS homopolymers, PS-*b*-P*t*BA diblock and PS-*b*-P*t*BA-*b*-PS triblock copolymers) exhibited the monomodal gel permeation chromatography (GPC) traces (**Figure 4**) and the molecular weight distribution of all star-like copolymers was very low (polydispersity<1.16). We also note that the polydispersity of star-like copolymers dictates the uniformity of HNCs in terms of outer diameter and shell thickness. The controlled livingness nature of ATRP endowed easily control of molecular weight of each individual block (i.e., precise tuning the length of each block) in star-like triblock copolymers, thereby enabling readily tuning the dimension of the HNCs. Notably, symmetric peaks can be observed in all GPC measurements,

suggesting that there was no inter-molecular coupling during ATRP process. The detailed information regarding the molecular weight and polydispersity of each individual block is summarized in **Table 3.2**.

Table 3.2 Molecular weights of amphiphilic star-like PS-*b*-PAA-*b*-PS and PS-*b*-PAA-*b*-PEDOT triblock copolymers and the corresponding dimensions of polymer-capped low bandgap hollow nanoparticles (HNCs).

Samples	$M_{n,\,PS1}$[a]	$M_{n,\,PAA}$[b]	$M_{n,\,PS2}$[c]	$M_{n,\,PEDOT}$[d]	**PDI**[d]	**Dimensions of PbTe HNCs (shell thickness /diameter of hollow interior)**[e] **(nm)**	**Dimensions of PbS HNCs (shell thickness /diameter of hollow interior)**[e] **(nm)**
Sample A	2,600	5,100	5,300	-	1.14	2.8 ± 0.2/3.5 ± 0.2	2.9± 0.2/3.6± 0.2
Sample B	1,000	7,200	9,500	-	1.12	4.6 ± 0.4/1.8 ± 0.2	-

Sample C	2,600	5,100	-	1,100	1.18	3.1 ± 0.3/3.2 ± 0.3	-

[a] Number average molecular weight of the inner PS block ($M_{n,PS1}$) was calculated from ^{1}H NMR data. The calculation method was adapted from previous work. [116]

[b] Number average molecular weight, M_n of each PAA block calculated based on ^{1}H NMR data from the molecular weight difference between P*t*BA block (before hydrolysis) and PAA block (after hydrolysis). The intermediate P*t*BA block can be calculated by the following equation:

$$M_{n,\mathrm{P}t\mathrm{BA}} = \frac{A_e/9}{A_d/5} \times M_{n,\mathrm{PS1}} \times \frac{M_{tBA}}{M_{St}}$$

where $M_{n,PtBA}$ and $M_{n,\ PS1}$ are molecular weights of the intermediate P*t*BA block and the inner PS block of each arm, respectively. A_e and A_d are the integral areas of methyl protons in *tert*-butyl group of P*t*BA chain and the integral area of phenyl protons in phenyl group of PS chain, respectively. M_{tBA} and M_{St} are molecular weights of *t*BA monomers and St monomers, respectively.

[c] Number average molecular weight of the outer PS block was calculated from ^{1}H NMR data based on the following equation:

$$M_{n,\mathrm{PS2}} = \frac{A_d/5}{A_e/9} \times M_{n,\mathrm{P}t\mathrm{BA}} \times \frac{M_{St}}{M_{tBA}} - M_{n,\mathrm{PS1}}$$

where $M_{n,PS1}$ $M_{n,PtBA}$ and $M_{n,PS2}$ are the molecular weights of the inner PS block, the intermediate P*t*BA block, and the outer PS block, respectively. A_e and A_d are the integral areas of methyl protons in *tert*-butyl group of P*t*BA chain and the integral area of phenyl protons in phenyl group of PS chain, respectively. M_{St} and M_{tBA} are molecular weights of St and tBA monomers, respectively.

[d] PDI was recorded by GPC

[e] The shell thickness of HNCs and the diameter of hollow interior were determined by performing image analysis on TEM images of HNCs.

It is worthwhile to note that in order to obtain uniform HNCs without impurities, it is critical to remove linear homopolymer P*t*BA (generated by second ATRP as side product) from star-like PS-*b*-P*t*BA diblock copolymers by manually fractional precipitation using acetone as solvent and methanol/water as precipitator prior to the third ATRP reaction (**Figure 3.4b and 4c**). The existence of this linear P*t*BA homopolymer will interfere nanocrystal formation because the linear PAA hydrolyzed from linear P*t*BA homopolymer will coordinate with metal precursors, which produces a large amount of lead chalcogenide micro sized crystals with irregular structures.

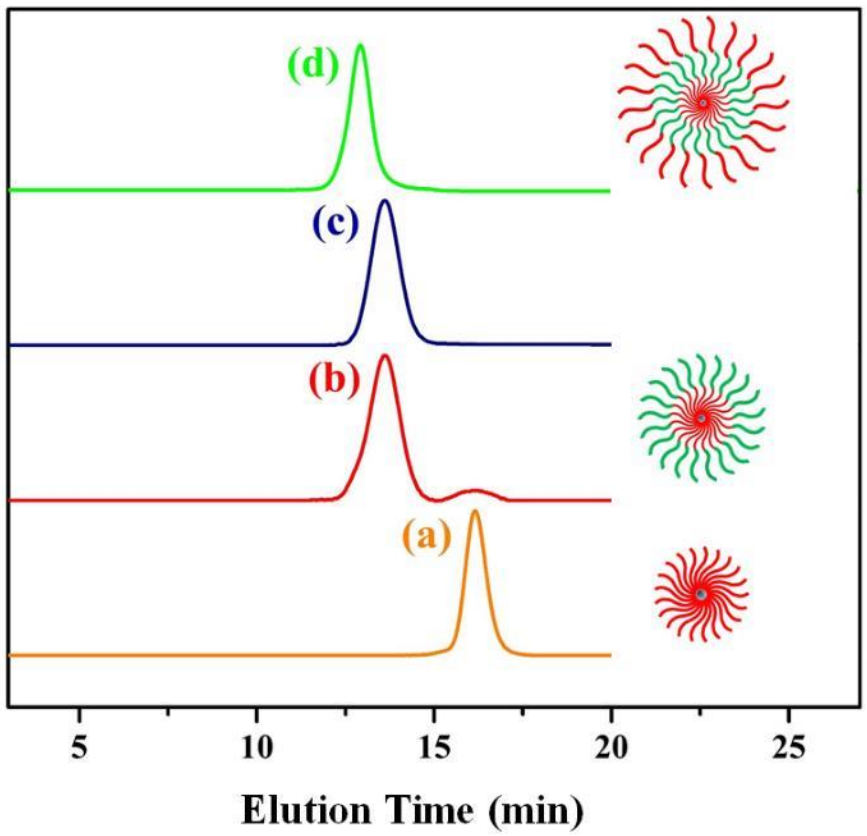

Figure 3.4 GPC traces of star-like homopolymer and block copolymers. (a) star-like PS-Br homopolymer, (b) star-like PS-*b*-P*t*BA-Br mixed with linear homopolymer P*t*BA generated during second ATRP, (c) star-like PS-*b*-P*t*BA-Br after the removal of linear P*t*BA by purification, and (d) star-like PS-*b*-P*t*BA-*b*-PS-Br.

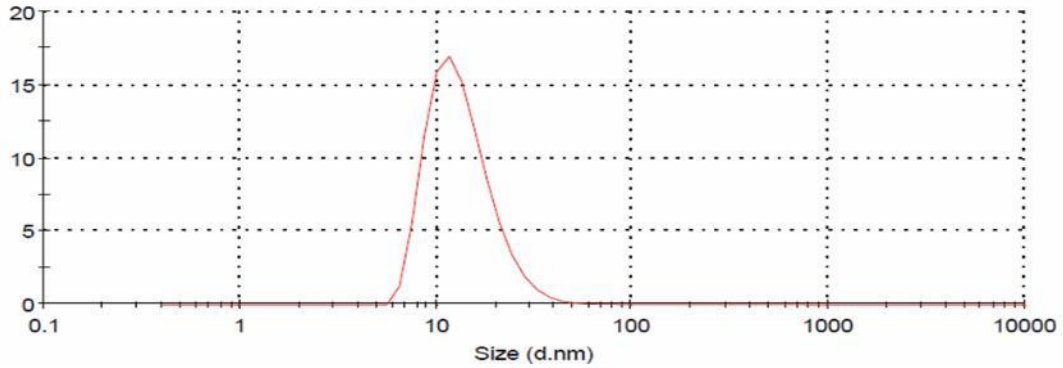

Figure 3.5 Dynamic light scattering measurement on unimolecular micelles of amphiphilic star-like PS-*b*-PAA-*b*-PS triblock copolymers.

The *tert*-butyl substituents in intermediate block of star-like PS-*b*-P*t*BA-*b*-PS can be easily hydrolyzed in the presence of trifluoroacetic acid, thereby generating star-like PS-*b*-PAA-*b*-PS triblock copolymer serving as nanoreactors in which lead chalcogenide precursors were selectively partitioned to PAA regime due to coordination ability of carboxylic acid groups in PAA blocks. The successful formation of monodispersed star-like PS-*b*-PAA-*b*-PS unimolecular nanoreactors was confirmed by DLS measurement, showing the uniform size of star-like triblock copolymers in dimethylformamide (DMF) which was good solvent for both PAA and PS blocks (**Figure 3.5**).

The feasibility and robustness of formation of narrow band gap lead chalcogenide HNCs prepared via well-defined star-like PS-*b*-PAA-*b*-PS unimolecular nanoreactors is demonstrated using PbTe HNCs as an example. Prior to PbTe HNCs synthesis, the star-

like PS-*b*-PAA-*b*-PS triblock copolymers were first dissolved in DMF/BA to form stable unimolecular spherical nanoreactors. The PbTe precursors separately prepared were added into the star-like PS-*b*-PAA-*b*-PS DMF solution, followed by refluxing at 160 °C. DMF is a good solvent for both PS and PAA blocks, while BA is a good solvent for PAA and poor solvent for PS. As a result, stable unimolecular micelles with well-defined spherical shape consisting of the fully expanded intermediate PAA chains and the collapsed inner and outer PS chains were formed in the mixed solvent of DMF/BA. The precursors were selectively partitioned into the hydrophilic PAA regime which can accommodate a large volume of precursors due to the expanded PAA chain conformation, and the strong coordination interaction between the carboxylic groups of PAA and the PbTe precursors. Under the high temperature refluxing, PbTe metal precursors (i.e., non-crystalline) in the compartment occupied by intermediate PAA blocks of star-like triblock copolymers led to the nucleation and growth of PbTe HNCs capped with PS chains inside the negatively curved hollow interior and outside the positively curved surface of HNCs. Since the surface of individual PbTe HNC is covalently and permanently connected with PS, the high solubility of PS in various organic solvents (i.e., polar solvents and non-polar solvents) confers an excellent colloidal stability of PbTe HNCs.

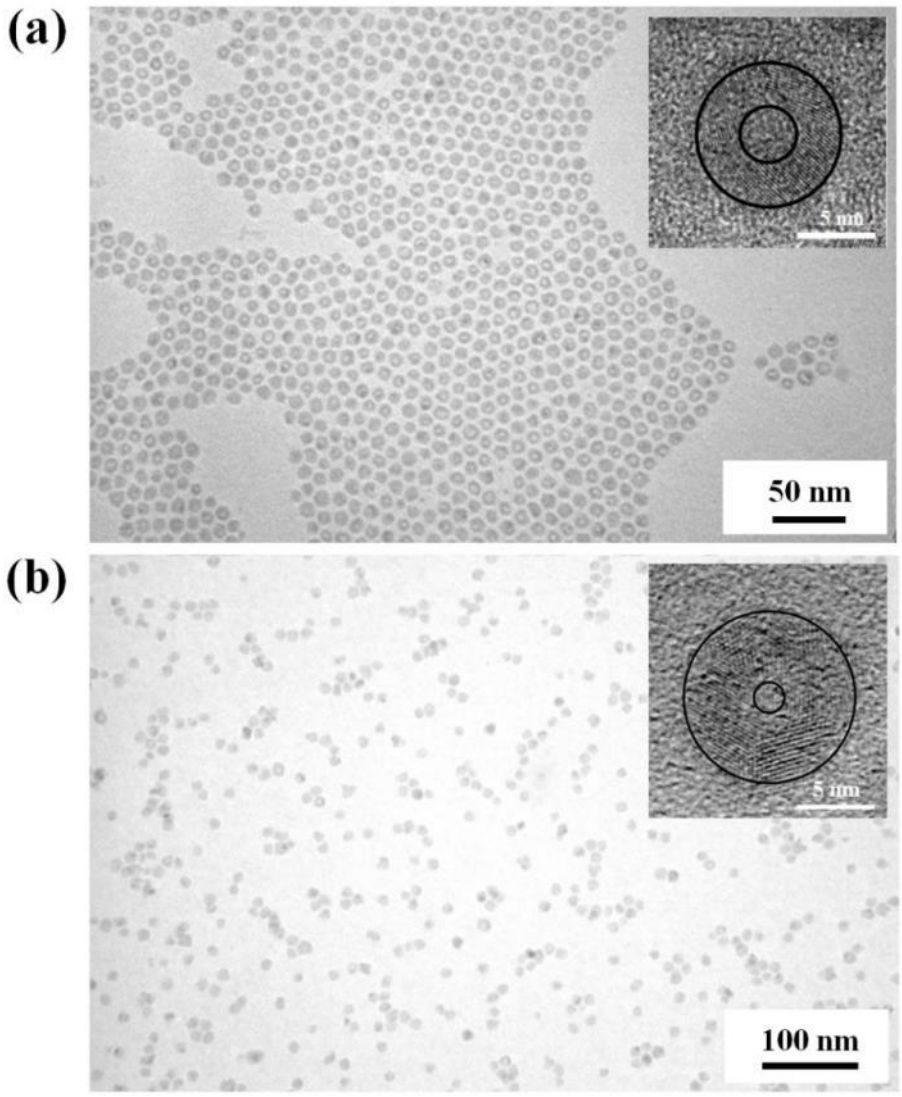

Figure 3.6 TEM images of PS-capped PbTe HNCs with (a) a diameter of hollow interior D_{hollow} = 3.5 ± 0.2 nm and shell thickness t = 2.8 ± 0.2 nm (Inset: HRTEM of PbTe HNCs), and (b) D_{hollow} = 1.8 ± 0.2 nm and shell thickness t = 4.6 ± 0.4 nm (Inset: HRTEM of PbTe HNCs), crafted by capitalizing on star-like PS-*b*-PAA-*b*-PS as nanoreactors. The black circles in insets are for guidance, showing the shell thickness of HNCs.

The formation of hollow interior in HNCs can be readily confirmed in TEM image (**Figure 3.6a**), in which a small bright dot can be clearly observed in the center of each HNC. More importantly, the HRTEM image (**Figure 3.6a** inset) further confirms the

crystallinity of as-synthesized HNCs, showing the formation of hollow nanocrystals with lattice spacing consistent with (220) interplanar distance of 0.23 nm of face-centered cubic PbTe as opposed to be amorphous hollow nanostructure. The amphiphilic star-like PS-*b*-PAA-*b*-PS copolymers serve as spherical nanoreactors in mixed high boiling point organic solvents and direct the formation of PbTe HNCs via selectively coordination between PbTe precursors and intermediate PAA block. The formation of hollow interior and PbTe nanocrystals can be ascribed to the fact that the innermost PS block does not possess any functional groups with coordination ability and only serves as nano-scaffold while intermediary PbTe precursors loaded in nanoreactors is converted to NCs through refluxing at high temperature. This mechanism is corroborated by the control experiment in which the star-like PAA-*b*-PS diblock copolymers are used as nanoreactors to craft PbTe NCs.

In addition, our star-like triblock copolymer nanoreactors strategy demonstrates excellent dimension control in stark comparison to conventional well-established routes. Uniform PbTe HNCs with varied core size and shell thickness prepared via utilization of star-like PS-*b*-PAA-*b*-PS triblock copolymers with varied molecular weight as nanoreactors are shown in **Figure 3.6b**. The detailed information regarding to the molecular weight and polydispersity of star-like triblock copolymers is summarized in **Table 3.2**.

It is illustrated in **Figure 3.6b** that utilizing star-like PS-*b*-PAA-*b*-PS triblock copolymers with varied molecular weight of PS and P*t*BA (hydrolyzed into PAA chains) enables the preparation of PbTe HNCs with precise tunable hollow interior and shell thickness. Again, HRTEM image substantiates the crystallinity of hollow nanostructures with lattice spacing of 0.32 nm consistent with interplanar distance of (200) plane in face-

centered cubic PbTe. In stark contrast to traditional approaches in which tunable preparation of HNCs is mainly achieved via adjusting temperature, the amount of small molecule ligands and reaction time, our nanoreactors strategy accomplishes the goal of size-tunable synthesis of HNCs merely through adjusting polymerization time during each cycle of ATRP reaction, which fully decouples factors controlling the dimension of HNCs. By increasing the polymerization time of P*t*BA blocks while decreasing the polymerization time of PS blocks, the shell thickness can be increased and the size of hollow interior can be decreased in a controlled way.

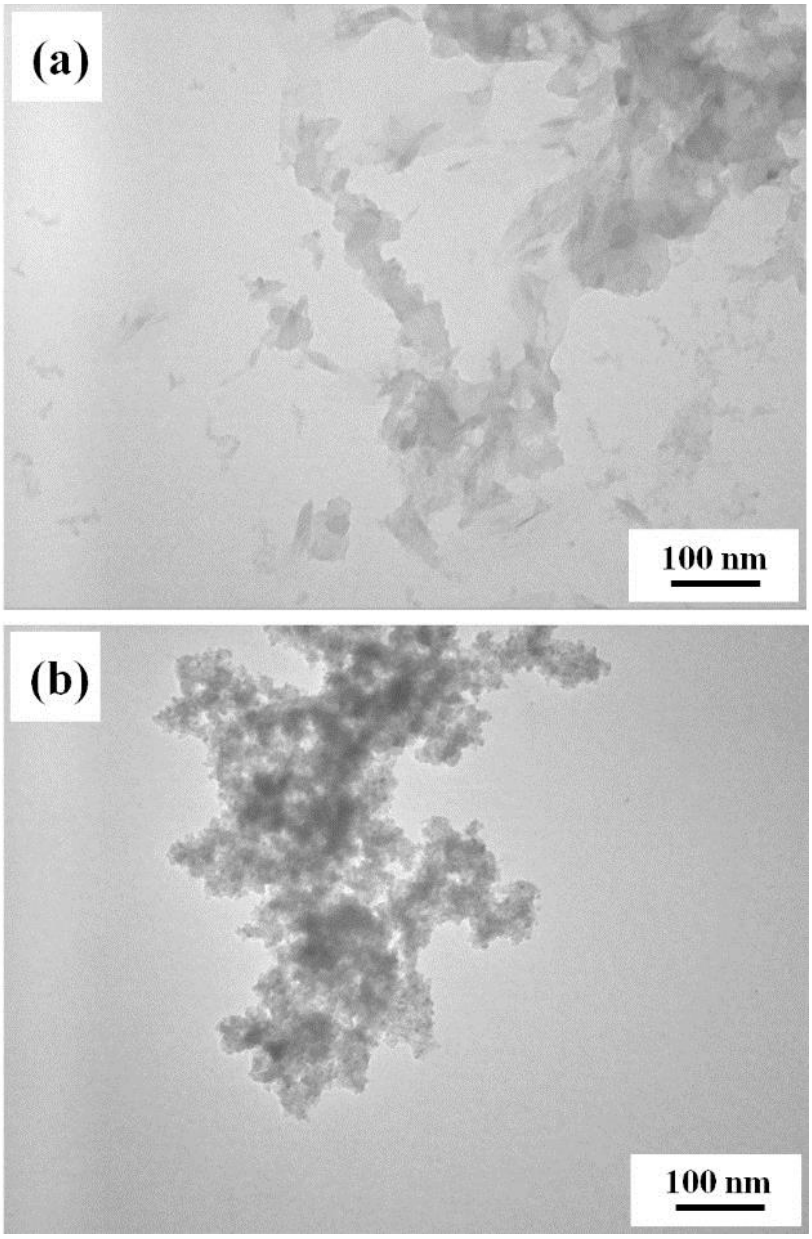

Figure 3.7 TEM images of as-synthesized PbTe crystals by employing different block copolymers as nanoreactors. (a) Using star-like PS-*b*-P*t*BA-*b*-PS as nanoreactors, and (b) using linear PS-*b*-PAA-*b*-PS as nanoreactors.

The excellent controllability of this strategy is owing to the controlled-livingness nature of ATRP, thereby producing star-like triblock copolymers with very narrow molecular weight distribution (i.e., length of each arm). In an effort to further substantiate

this HNCs formation mechanism via star-like triblock copolymers, we conduct two control experiments in which star-like PS-*b*-P*t*BA-*b*-PS triblock copolymers and linear PS-*b*-PAA-*b*-PS are employed as nanoreactors to grow PbTe HNCs. Hydrophobic star-like PS-*b*-P*t*BA-*b*-PS triblock copolymers are expected to maintain a well-defined spherical star-shape in mixed solvents composed of DMF and BA. Nevertheless, the presence of *tert*-butyl group as opposed to be carboxylic acid group in the star-like copolymer contributes to its inability to selectively sequester PbTe precursors dissolved in DMF. Consequently, PbTe crystals grow in a way that star-like copolymers fails to serve as nanoreactors during crystal growth process, contributing to crystalline PbTe with irregular and ill-defined morphology (**Figure 3.7a**). Equivalently, linear PS-*b*-PAA-*b*-PS also fails to direct the growth of PbTe HNCs due to the fact that although PAA chains in linear triblock copolymers are able to coordinate with metal precursors, this linear copolymers are not able to form thermodynamically stable micelles in mixed DMF/BA solutions at high temperature. As a result, only large and irregular PbTe aggregation is obtained (**Figure 3.7b**).

It is well-established that classical synthetic routes to metal chalcogenide NCs require temporally discrete homogenous nucleation induced by hot injection of precursors dissolved in organic compounds followed by steady crystallite growth due to re-heating at high temperature. Obviously, the net result of homogeneous nucleation of nuclei followed by crystallite growth tend to result in high-quality solid metal chalcogenides NCs with only positive curvature. The formation of solid metal chalcogenides NCs with narrow size distribution can be explained by classical nucleation theory. However, classical nucleation theory indicates that the formation of hollow nuclei is impossible. Assuming that the

surface energy per area (γ) and the bulk energy change per volume (ΔG_v) are constant, the Gibbs free energy change (ΔG) resulting from homogeneous nucleation is written as:

$$\Delta G = \frac{4}{3}\pi(R_2^3 - R_2^3)\Delta G_v + 4\pi\gamma(R_2^2 + R_1^2) \quad (1)$$

where R_2 and R_1 are outer and inner radius of a hollow spherical nucleus. The equation (1) is reduced to classical nucleation equation when $R_1 = 0$. In the nucleation period of solid nanocrystal, there is a critical radius above which growth of nuclei is energetically favorable whereas the growth of those nucleus with radius smaller than critical size is forbidden because of increasing in Gibbs free energy. It becomes evident that the growth of HNCs has higher thermodynamic energy barrier that originates from the extra interior surface, which translates into the fact that nuclei with hollow interior tend to spontaneously dissolve back to solution. In other words, the formation of nuclei from which HNCs are able to grow is thermodynamically forbidden. This is principle reason why the conventional protocols for synthesizing HNCs (e.g., Kirkendall effect, galvanic replacement method, etching method, etc.) usually involve the synthesis of sacrificial nanocrystals with only positive curvature followed by post-synthesis procedure (e.g., oxidation or etching to dissolve sacrificial core) which transforms solid core into hollow interior. The energy barrier originated from the extra interior is mediated by this two-step method, thereby causing the transformation from solid to hollow NCs thermodynamically favorable.

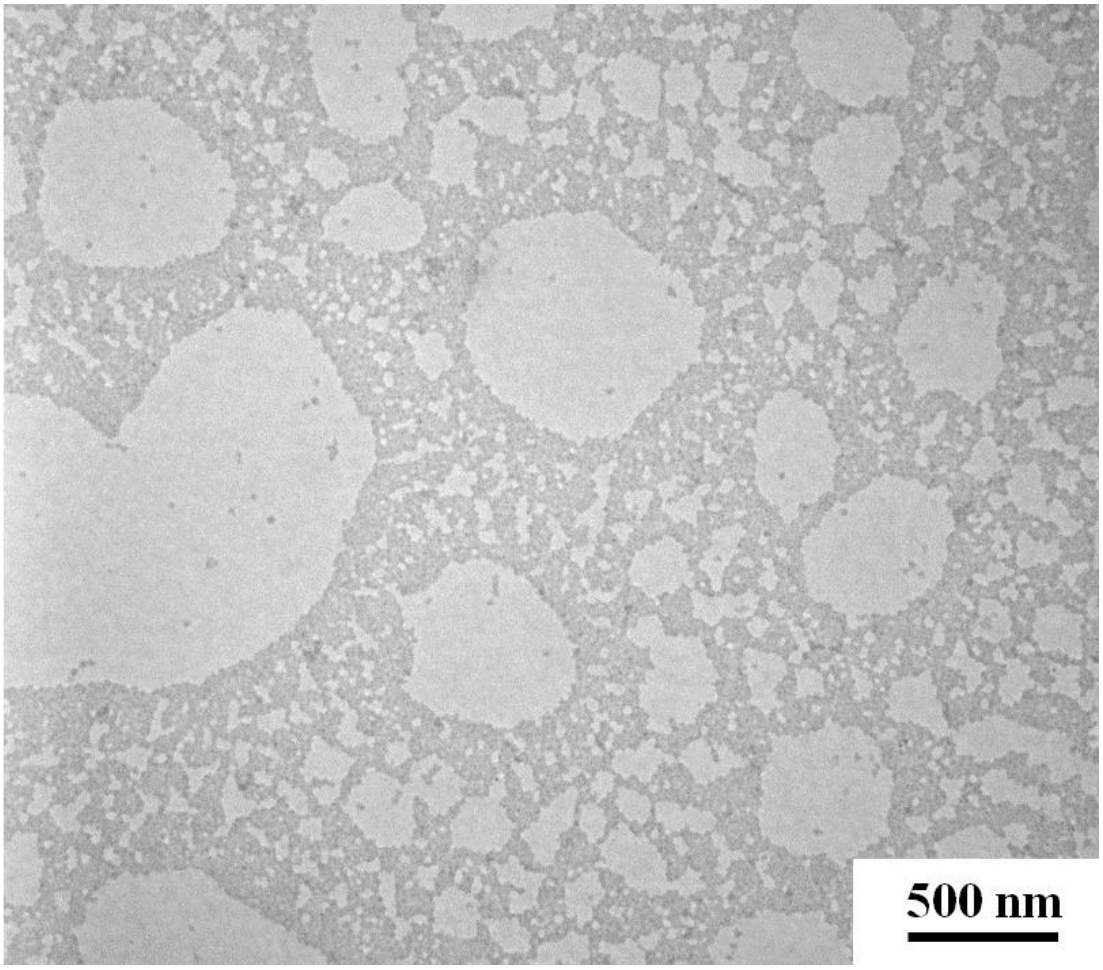

Figure 3.8 TEM image of PbTe HNCs shows a large area where HNCs form long-distance well-ordered packing.

In stark contrast to traditional synthetic method, our nanoreactors-approach circumvents this classical nucleation problem via utilizing 21-arm star-like PS-*b*-PAA-*b*-PS triblock copolymers to direct the growth of crystalline PbTe in specific intermediate PAA domain and eventually form PbTe HNCs in one step without using any sacrificial template. The energetically unfavorable increase in interfacial energy causing interior hollow structure is compensated by HNCs growth directly dictated by star-like copolymers without post synthesis process.

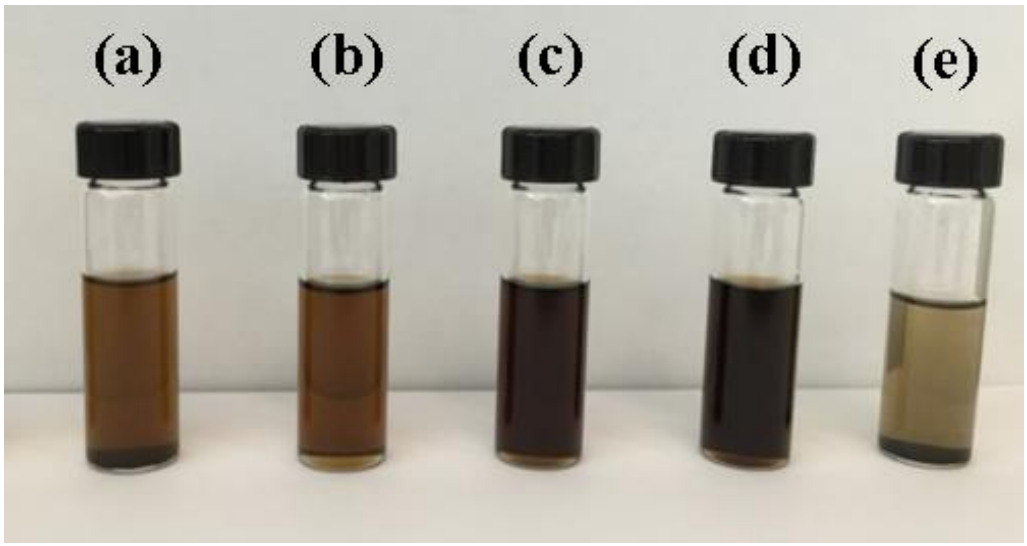

Figure 3.9 Digital image of colloidal PbTe HNCs dispersed in different organic solvents. (a) toluene, (b) chlorobenzene, (c) dimethylformamide, (d) dimethylacetamide, and (e) the introduction of ethanol into the PbTe HNP toluene solution (forming precipitates on the bottom of vial) (The color difference in the photograph is due to the different concentration of nanoparticles).

Besides, based on the TEM image of PbTe HNCs showing large area (**Figure 3.8**), they tend to self-assemble into hexagonally-packed array or disperse evenly in whole TEM image, indicating that solubility of as-synthesized PbTe HNCs capped with PS in organic solvent is comparable to that of PbTe NCs prepared from conventional PbTe NCs anchored with alkylphosphine (TOP, TBP or TOPO) as ligands. Dispersion of PbTe HNCs are stabilized by the presence of PS chains anchored on the surface of HNCs. This is substantiated by the fact that the flocculation of HNCs can be achieved through introduction of non-solvent (i.e., ethanol) for PS (**Figure 3.9e**). In addition, since most of alkylphosphine compounds are non-polar, the resultant semiconducting PbTe NCs prepared by conventional approaches displays very poor solubility in polar organic solvents, including DMF, dimethyl sulfoxide (DMSO) and dimethylacetamide (DMA).

Owing to the superb solubility of PS in various organic solvent, the as-synthesized PbTe HNCs display excellent solubility and stability in not only non-polar solvents (e.g., chlorobenzene, toluene, etc.) (**Figure 3.9a and b**) but also in various common polar solvents (e.g., DMF, DMA, etc.) (**Figure 3.9c and d**).

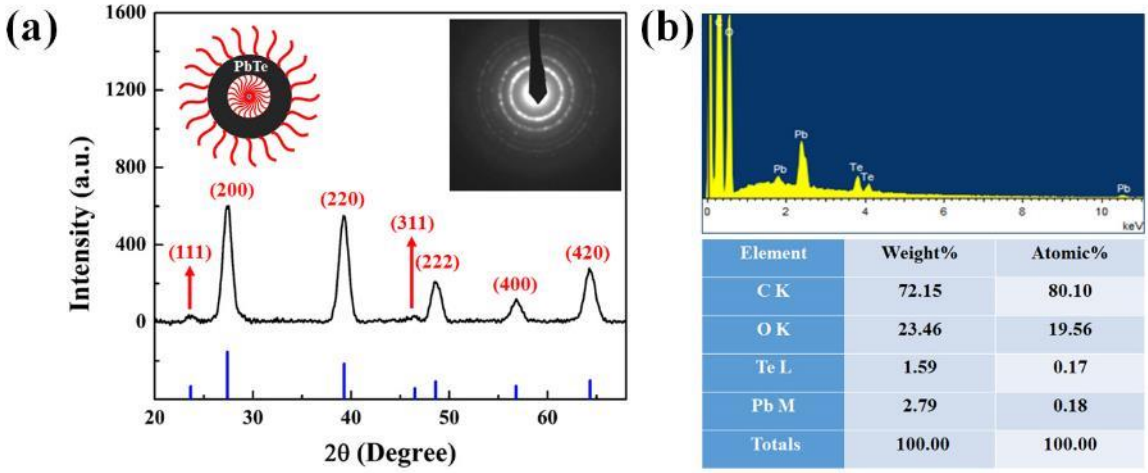

Element	Weight%	Atomic%
C K	72.15	80.10
O K	23.46	19.56
Te L	1.59	0.17
Pb M	2.79	0.18
Totals	100.00	100.00

Figure 3.10 (a) XRD profile of PbTe HNCs tethered with PS chains inside the hollow interior and outside the surface of HNP. The blue lines represent the standard diffraction pattern of bulk PbTe (reference code: 03-065-0324). The inset is the selective area electron diffraction (SAED) pattern of PS-capped PbTe HNCs crafted by utilizing amphiphilic star-like PS-*b*-PAA-*b*-PS as nanoreactors (Sample A in Table 3.2). (b) Energy-dispersive X-ray (EDX) analysis of PbTe HNCs capped with PS on the surface as the stabilizing ligand.

Figure 3.10a depicts the X-ray diffraction (XRD) pattern of PS capped PbTe HNCs prepared by using star-like PS-*b*-PAA-*b*-PS as nanoreactors. The characteristic diffraction peaks can be indexed to pure face-centered cubic phase of PbTe which is consistent with the standard XRD profile of bulk PbTe (**blue line in Figure 3.10a**). The broadening of diffraction peaks further confirms the small crystalline size of resulting PbTe HNCs. Energy dispersive X-ray spectroscopy (**Figure 3.10b**) performed on as-synthesized PbTe

HNCs capped with PS further substantiated that the atomic ration of Pb to Te was 1:1 which is consistent with ideal chemical composition ratio in crystalline PbTe.

Since the growth process of PbTe HNCs is directed by intermediate PAA block as opposed to be outmost PS block, this synthetic approach displays a great surface chemistry tunability compared to conventional PbTe NCs synthesis in which alkylphosphine ligands play a vital role in nucleation and growth process and tunable surface chemistry can only be obtained by post-synthesis ligand-exchange process. However, tunable surface chemistry of PbTe HNCs can be achieved via precise macromolecular design of amphiphilic star-like PS-*b*-PAA-*b*-PEDOT triblock copolymers prepared by combination of sequential ATRP and Cu (I)-catalyzed alkyne-azide cycloaddition reaction (click reaction), as illustrated in **Figure 3.1**.

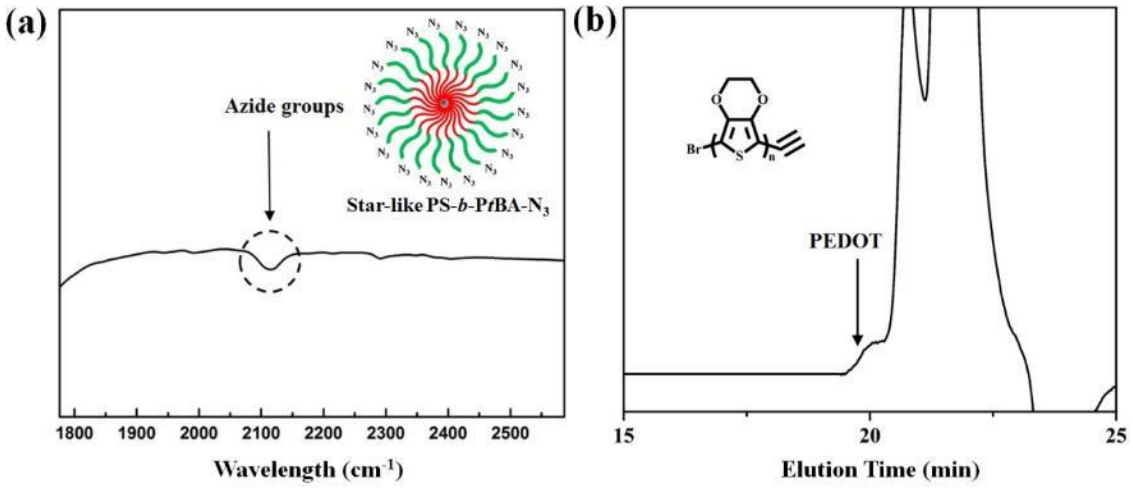

Figure 3.11 (a) FTIR spectrum of star-like PS-*b*-P*t*BA-N_3, and (b) GPC trace of ethynyl-terminated PEDOT.

Star-like PS-*b*-P*t*BA-N_3 is synthesized by sequential ATRP of St and *t*BA followed by postpolymerization S_N2 reaction of the halide terminus with sodium azide, thereby producing azide terminated star-like diblock copolymers from which alkyne terminated linear polymer can be grafted. The successful azidation reaction can be confirmed by the appearance peak around 2100 cm^{-1} in FTIR spectrum, which is corresponding to a characteristic stretching of $–N_3$ group (**Figure 3.11a**). And the successful polymerization of PEDOT via GRIM method can be characterized by DMF GPC (**Figure 3.11b**). Prior to the grafting of PEDOT, star-like PS-*b*-P*t*BA-N_3 diblock copolymers do not exhibit absorption in the visible range due to the insulating nature of copolymers. After grafting of conjugated PEDOT, star-like PS-*b*-PAA-*b*-PEDOT triblock copolymers should display absorption in the visible range due to the presence of semiconducting conjugated PEDOT blocks. Accordingly, the successful click reaction is confirmed by the appearance of absorption peak of star-like triblock copolymers in the visible range (**Figure 3.12**).

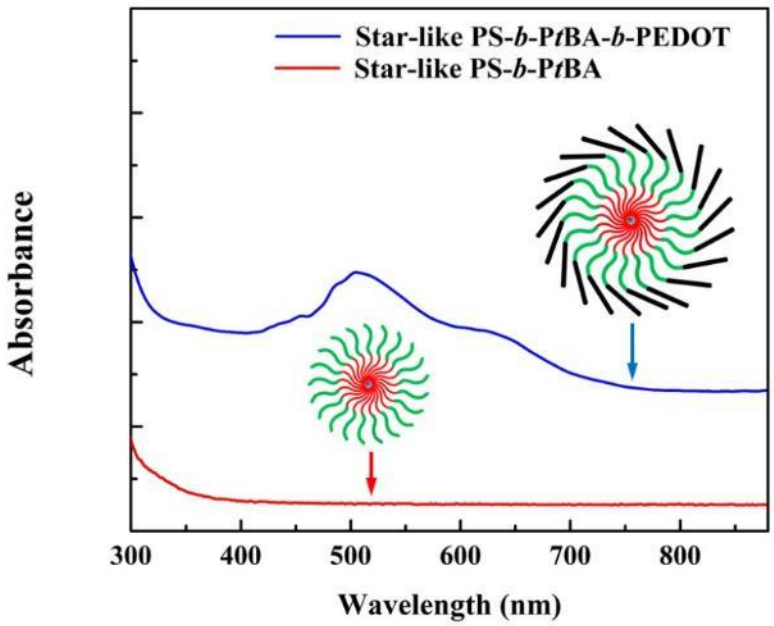

Figure 3.12 Comparison of UV-Vis spectra of star-like PS-*b*-P*t*BA diblock copolymers with star-like PS-*b*-P*t*BA-*b*-PEDOT triblock copolymers.

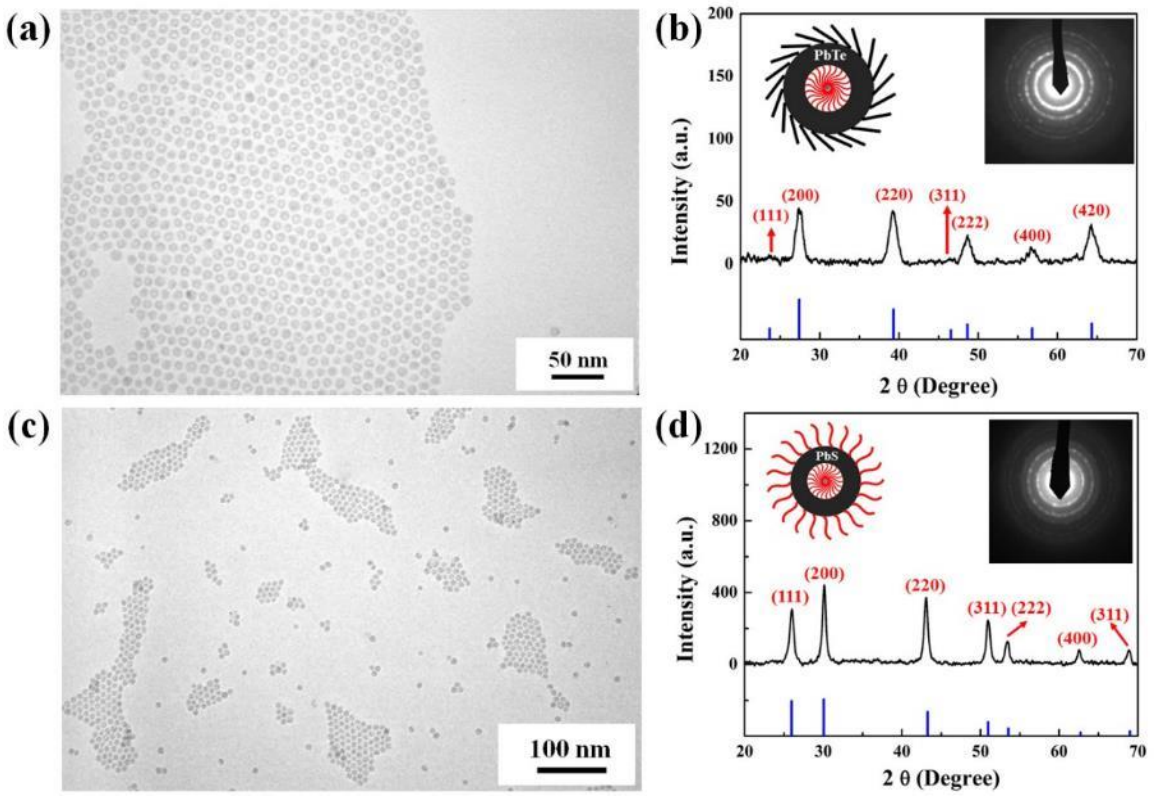

Figure 3.13 (a) TEM image and (b) XRD profile of conjugated PEDOT-capped PbTe HNCs with a shell thickness t = 3.1 ± 0.3 nm and a diameter of hollow interior D_{hollow} = 3.2 ± 0.3 nm crafted by employing star-like PS-*b*-PAA-*b*-PEDOT as nanoreactors. The blue lines represent the standard XRD pattern of bulk PbTe. The inset is the SAED pattern of PEDOT-capped PbTe HNCs. (c) TEM image and (d) XRD profile of PS-capped PbS HNCs with a shell thickness t = 2.9 ± 0.2 nm and a diameter of hollow interior D_{hollow} = 3.6 ± 0.2 nm crafted by utilizing star-like PS-*b*-PAA-*b*-PS as nanoreactors. The blue lines represent the standard XRD pattern of bulk PbS. The inset is the SAED pattern of PS-capped PbS HNCs.

Figure 3.13 depicts TEM image and XRD pattern of PbTe HNCs capped with PEDOT via utilizing star-like PS-*b*-PAA-*b*-PEDOT triblock copolymers as nanoreactors.

It is shown in TEM image that substitution of outer block hydrophobic PS with semiconducting conjugated PEDOT does not have any impact on the morphology of PbTe HNCs, suggesting that our template method enables a great surface chemistry tunability of HNCs. EDS analysis is also performed to substantiate chemical composition fidelity of resulting PbTe HNCs when outer PS blocks is changed from PS to PEDOT blocks (**Figure 3.14a**).

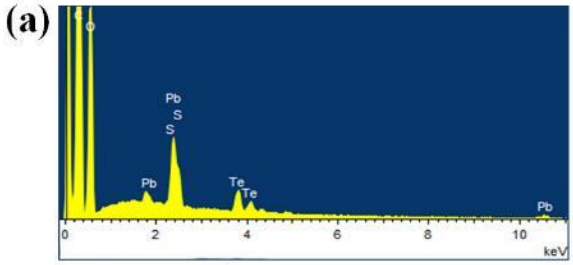

Element	Weight%	Atomic%
C K	72.06	80.35
O K	22.93	19.20
S K	0.17	0.07
Te L	1.87	0.20
Pb M	2.97	0.20
Totals	100.00	100.00

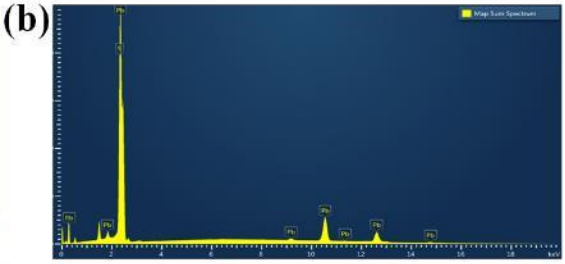

Element	Weight%	Atomic%
S K	13.3	51.00
Pb M	86.6	49.00
Totals	100.00	100.00

Figure 3.14 (a) EDX analysis of PEDOT-capped PbTe HNPs using star-like PS-*b*-PAA-*b*-PEDOT as nanoreactors, and (b) EDX analysis of PS-capped PbS HNPs using star-like PS-*b*-PAA-*b*-PS as nanoreactors.

Colloidal narrow band gap NCs synthesized from traditional methods are stabilized by insulating organic ligands (e.g., oleic acid, TOP or TOPO) which necessitates post-synthesis ligand exchange process in order to generate good interparticle coupling for the purpose of device application. Despite tremendous progress in NCs synthetic methodologies, ligand exchange approach to replace long hydrocarbon chains with

molecular metal chalcogenide complexes based on pioneering work by Talapin's group [34] relies on the utilization of hydrazine which is very toxic and explosive especially considering that anhydrous and high-purity hydrazine is necessary for effectively complete removal of surface insulating ligands. In contrast with this hydrazine-based ligand-exchange methodology, our method based on the usage of the well-designed star-like copolymers as nanoreactors provides an alternative route to this method and offer an one-pot hydrazine-free approach to achieve this goal. Besides, since the narrow band gap NCs, especially lead chalcogenides NCs, are prone to the oxidation or decomposition in the response to the external stimuli (e.g., oxygen and water), it is favorable to achieve the synthesis and surface functionalization of narrow band gap NCs in single one step. Moreover, since the surface chemistry tunability is accomplished by grafting the pre-synthesized alkyne terminated conjugated polymers onto azide terminated star-like diblock copolymers using click reaction, it is envisioned that this synthetic route can be readily extended to the preparation of PbTe HNCs capped with various conjugated polymers, like poly(3-hexylthiophene), or other clickable molecules while preserving the morphology and structural integrity of lead chalcogenides HNCs.

The general applicability of this synthetic strategy is demonstrated by extending this nanoreactor method to other lead chalcogenides HNCs (i.e., PbS). PbS HNCs can be easily generated using star-like PS-*b*-PAA-*b*-PS amphiphilic copolymers as nanoreactors (**Figure 3.13c**) and corresponding PbS precursors. It is shown in TEM that a clearly bright dot can be observed in the center of each individual NCs, indicating that triblock copolymers can also serve as nanoreactors to direct the growth of PbS HNCs with size dimension comparable to the case of PbTe HNCs. Structure and chemical composition of

resulting PS capped PbS HNCs are confirmed by XRD (**Figure 3.13d**) and EDS (**Figure 3.14b**), respectively.

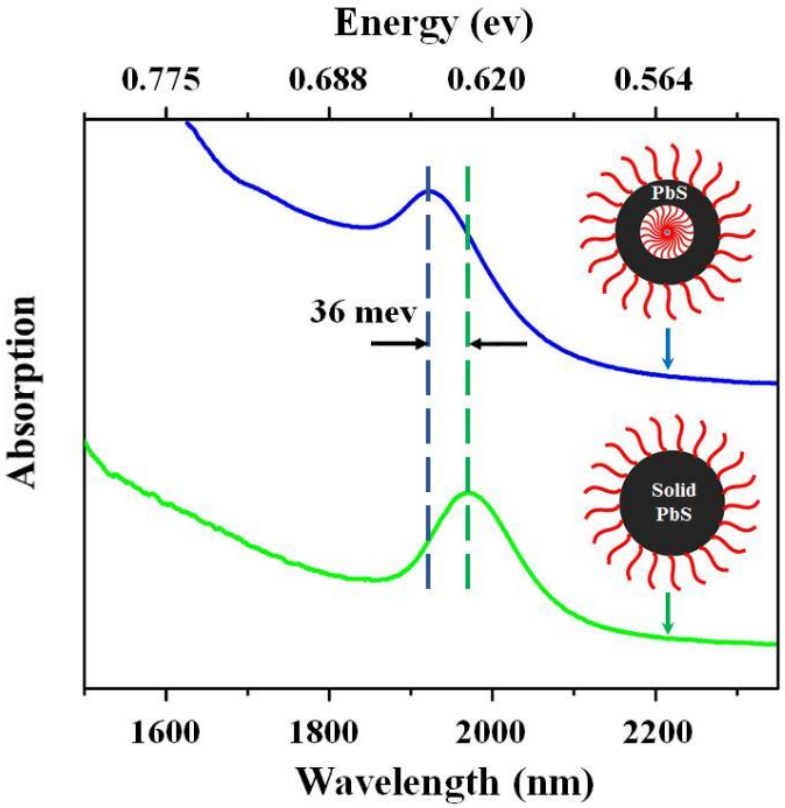

Figure 3.15 Near infrared (NIR) spectra of PS-capped PbS HNPs with a shell thickness t = 2.9 ± 0.2 nm and a diameter of hollow interior D_{hollow} = 3.6 ± 0.2 nm crafted by utilizing star-like PS-*b*-PAA-*b*-PS as nanoreactors, and PS-capped PbS solid NPs with the same external diameter prepared by utilizing star-like PAA-*b*-PS as nanoreactors.

More interestingly, the formation of hollow interior with negative curvature influences absorption spectrum of lead chalcogenides HNCs. It is well-established that shrinking the size of NC contributes to the increase in the fraction of surface atoms which possess lower coordination numbers (CNs) compared with atoms located in the core of the NCs. Notably, in comparison with a flat surface, the surface with positive curvature has

lower CNs whereas the surface with negative curvature has higher CNs. It is also worthwhile to note that the CNs of atom at surface with negative curvature is still lower compared with atoms in core region. The most pronounced distinction between HNCs and solid NCs is the increase in the fraction of uncoordinated atoms due to the presence of hollow interior with negative curvature, leading to the decrease in average CNs of individual HNC. The optical band gap originated from crystal potential is dependent upon the first Fourier coefficient of crystal filed which is proportion to the average cohesive energy per bond. The decrease in mean CNs of individual HNC due to the inner surface with negative curvature causes the increase in the average cohesive energy per bond which translates into the increase in optical bad gap of resulting lead chalcogenide HNCs. The blue shift of absorption peak of PbS HNCs (**Figure 3.15**) can be semi-quantitatively explained by equation 1 based on BOLS model. [114]

$$\Delta E_g(R,r) = E_g(B)\left\{\frac{z_b}{\langle z\rangle}\left[\tau_{in}\left(\sqrt{z_{in,B}}-1\right)+\tau_{out}\left(\sqrt{z_{out,B}}-1\right)+1\right]-\frac{z_b}{\langle z\rangle}\left[\tau\left(\sqrt{z_{s,B}}-1\right)+1\right]\right\}$$

where $\Delta E_g(R,r)$ is optical bandgap difference between HNPs and solid NPs, E_g (B) is bandgap of material in bulk, z_b is CNs of an atom in bulk, <z> is the mean CNs of atoms in HNPs, $z_{out,B}=Z_{out*}/Z_b$, $z_{in,B}= Z_{in*}/Z_b$, and $z_{S,B}= Z_{S*}/Z_b$ (Z_{out*}, Z_{in*} and Z_{S*} are the effective CNs of the outer and inner surfaces of HNP and solid NP, respectively). τ_{in} and τ_{out} are surface-to-volume ratios in inner and outer surfaces, respectively. $\tau = 6hc/D$, where h is diameter of an atom, D is outer diameter of HNP and c is bond contraction coefficient of the surface layer. The first term (underlined with black solid line) in equation (2) describes the optical bandgap of HNPs, and the second term (underlined with black dashed line) accounts for the optical bandgap of solid NPs with an external diameter same as HNPs.

Theoretical modeling based on this equations indicates$\Delta E_g(R,r) > 0$ [3, 4] suggesting an increased optical bandgap for HNPs with a hollow interior, and thus a blue-shift of absorption maximum for HNPs compared to solid counterpart.

3.4 Summary

In summary, we developed a viable star-like triblock copolymer nanoreactor strategy to in-situ craft uniform low bandgap lead chalcogenide HNPs with readily and independently tailorable dimensions (varied diameter of hollow interior and shell thickness), compositions (PbTe and PbS) and surface chemistry (hydrophobic PS-capped and conjugated PEDOT-capped), which are not easily accessible by conventional approaches. The growth of lead chalcogenides is facilitated by the strong coordination between the intermediate PAA blocks and the metal moieties of precursors. The presence of PS and PEDOT as intimately connected surface ligands renders the superior solubility of the resulting HNPs in organic solvents (i.e., oil-soluble HNPs). Importantly, compared to solid NPs with the same external diameter, lead chalcogenide HNPs exhibited an absorption maximum blue-shift due to the existence of hollow interior, which is in good agreement with the theoretical model based on the BOLS correlation mechanism. Clearly, in addition to PbTe and PbS HNPs demonstrated in this study, the star-like triblock copolymer nanoreactor strategy is viable and may afford in-situ synthesis of an exciting variety of, virtually unlimited, uniform polymer-capped HNPs of different sizes, materials, and surface functional ligands. As such, it represents a general and robust strategy for producing functional low bandgap HNPs and exploring how internal (e.g., dimension, composition, and surface ligand) and external (e.g., light, pH, temperature, and magnetic and electric fields) parameters influence the physical properties of HNPs and their

assemblies for a wide range of applications in solar energy conversion (e.g., quantum dot solar cells, light emitting diodes, and near-IR photodetectors due to tunable optoelectronic properties), thermoelectric devices, batteries (owing the presence of hollow interior for accommodating volume expansion and shortening the transport length for electrons and Li ions), sensors, bioimaging, and photothermal therapy.

CHAPTER 4. STABLE ORGANOLEAD HALIDE PEROVSKITE NANOCRYSTALS WITH MARKEDLY IMPROVED STABILITY VIA UTILIZING STAR-LIKE TRIBLOCK COPOLYMERS AS NANOREACTORS

4.1 Introduction

Organolead halide perovskite materials with typical chemical formula $APbX_3$ (A: monovalent organic ammonium cation, such as $CH3NH3^+$ or $CH(NH2)2^+$; X: Cl, Br or I) have attracted considerable attention as promising candidate for the next generation of material for photovoltaics [117], light emitting dioxides (LEDs) [52] and photodetectors [118] due to their excellent excitonic, optical and charge transport property. Nevertheless, the application of organolead halide perovskites is hindered by their intrinsic structural instability, leading to extreme sensitivity to external stimuli, including moisture, polar or protic solvent, UV light and oxygen. These inherent instability issues become more pronounced as the dimension of organolead halide perovskite shrinks to a couple of nanometer length-scale due to the significant increased surface to volume ratio. Pioneering works regarding the synthesis of colloidal organolead halide perovskite nanocrystals (PNCs) have been achieved through solution-based procedure, [55, 58, 67, 70] yielding high-quality PNCs with narrow size distribution, ultrahigh photoluminescence quantum yield, narrow full with at half maximum and wide tunable band gap through visible range. Accordingly, the advancement of the performance of the PNCs based state-of-the-art high-efficiency photovoltaic solar cells, [61] LEDs [119, 120] and laser devices [121] renders the improvement of perovskite stability an imperative task. Accordingly, several synthetic

strategies have been successfully employed to enhance the stability of PNCs in the response to the external stimuli, such as incorporation of PNCs in silica, silica/alumina monolith or amorphous alumina, [122-124] in-situ formation of PNCs in mesoporous silica matrix, [125, 126] swelling-deswelling microencapsulation in polymer matrix, [127] stabilization by nanocrystal surface [61] and passivation with protective ligands. [81, 128] Despite recent remarkable advancement of stable PNCs, there are several inherent limitations associated with these synthetic routes. For instance, encapsulation of PNCs in silica or silica/alumina monolith usually decreases the colloidal stability and the solution processability of as-synthesized protecting layer coated PNCs in different non-polar solvents. Furthermore, the preparation of PNCs, especially organoclead halide PNCs via LARP, necessitates the usage of dimethylformamide (DMF) or dimethyl sulfoxide (DMSO) as solvent due to the poor solubility of lead halide in most of organic solvents, which is likely to cause defects on the surface or intrinsic halide vacancies of PNCs, leading to increase in propensity to degradation of PNCs when exposed to air or polar solvents. [57] More importantly, conventionally prepared PNCs generally involve the utilization of weak protic solvents (e.g., hydrocarbon alcohol) or polar solvents as precipitants during purification process, which could inevitably pose a negative effect on structural integrity of PNCs [129] and render the preparation of highly sensitive organolead iodide PNCs a very challenging task especially considering that organolead iodide PNCs are fully ionic NCs and the trace amount of protic molecules can decompose PNCs. Besides, introduction of polar solvents during isolation and purification process causes loss of bright photoluminescence and colloidal stability due to highly dynamic binding of short-chain ligands on the surface of

PNCs. [130] To the best of our knowledge, a robust synthetic strategy to simultaneously address these stability issues remains elusive.

Here, in an effort to tackle all aforementioned issues, we employ two types of 21-arm star-like amphiphilic triblock copolymers (i.e., poly(4-vinylpyridine)-block-poly(tert-butyl acrylate)-block-polyethylene oxide, denoted as star-like P4VP-b-PtBA-b-PEO and poly(4-vinylpyridine)-block-poly(tert-butyl acrylate)-block-polystyrene, denoted as star-like P4VP-b-PtBA-b-PS) as nanoreactors to craft polymer tethered organolead halide/silica core/shell NCs (CSNCs) with methylammonium lead bromide/silica (MAPbBr3/silica) as a typical example. In comparison to well-established conventional hot-injection method [58] and ligand assisted reprecipitation approach, [70] our nanoreactors strategy based on star-like triblock copolymers exhibits several advantages, which confers superior colloidal stability, chemical composition stability, photostability, moisture and protic polar solvents resistance and tunable surface chemistry. First, our nanoreactors strategy enables the preparation of organolead halide PNCs through *in-situ* conversion of lead halide nanocrystals, thereby giving rise to the possibility of preparation of various organolead PNCs, because the lead halide can readily react with organic halide salt to produce corresponding perovskite materials. Accordingly, our synthetic route is of general applicability and can be exploited for various chemical compositions, in particular, for methaylammonium lead halide. Second, our nanoreactors strategy offers an elegant route to purify PNCs solely based on non-polar solvent with very low polarity (e.g., hexane or heptane functioning as precipitants as opposed to be solvents), thereby minimizing potential damage during purification process and preserving the structural integrity of organolead halide PNCs, which is an impossible task for conventional methods,

considering that traditionally synthesized PNCs are usually stabilized with short ligands, such as oleylamine and oleic acid, which have high solubility in a wide range of non-polar solvents. Third, our nanoreactors strategy demonstrate a facile and robust way to realize tunable surface chemistry of PNCs (i.e., ligands can be tuned from hydrophilic polymer (e.g. hydrophilic PEO) to sterically hindered linear polymer with bulky pendant groups (e.g., hydrophobic PS)), which has not been demonstrated by conventional methods. Moreover, since star-like triblock copolymers are prepared via ATRP in combination with click reaction, our strategy presents a facile route to grafting any polymers that can be prepared via ATRP or click reaction onto the surface of PNCs, thereby giving rise to an exciting variety of polymer-PNCs nanohybrids. Furthermore, permanently and covalently tethered polymer ligands conserve the solution processability of silica passivated PNCs in comparison to conventionally synthesized protecting layer coated PNCs. Fourth, in contrast to conventional methods, our nanoreactors strategy does not rely on any high boiling point solvents (e.g., octadecene used in hot injection method for preparing all-inorganic PNCs) or the usage of non-volatile solvent (e.g., dimethylformamide used in LARP method for crafting organic-inorganic hybrid PNCs) is completely exempted. All solvents involved in current synthesis process are low-boiling point, volatile, which is beneficial for potential device fabrication. More importantly, the aforementioned advantages endows a superior stability to PNCs in terms of colloidal stability (owing to viable and versatile surface chemistry offered by third block of triblock copolymer nanoreactors), chemical composition stability, moisture and protic polar organic solvents resistance (owing to well-controlled silica shell protection and the protic solvent-repellent

third block in triblock copolymers) as well as descent structural stability (owing to complete absence of DMF during synthesis process).

4.2 Experimental Details

4.2.1 Materials

Methanol (99.8%), ethanol (99.8), isopropyl alcohol (>98.0%), tert-butanol (>99.0%), toluene (99.5%), chloroform (99.8%), dichloromethane (DCM, >99.5%), tetrahydrofuran (THF, GR ACS grade), anisole (99.0%), acetone (ACS reagent, >99.5%), γ-butyrolactone (GBL, >99.0%), dimethyl sulfoxide (DMSO, >99.0%), N,N-diethylformamide (DEF, 99.0%), anhydrous N,N-dimethylformamide (DMF, >99.8%), anhydrous 1-methyl-2-pyrrolidinone (NMP, 99.5%), heptane (99.0%), anhydrous n-hexane (95.0%), anhydrous 2-propanol (99.5%), α-bromoisobutyryl bromide (99.0%), sodium azide (>99.5%), diphenyl ether (DPE, 99.0%), methylamine solution (33 wt. % in absolute ethanol), formamidine acetate salt (99.0%), hydrobromic acid (48 wt. % in water, >99.99%), hydriodic acid (contains no stabilizer, distilled, 57 wt. % in H_2O, 99.99% trace metals basis), anhydrous diethyl ether (>99.0%), sodium bicarbonate (>99.7%), copper (II) chloride ($CuCl_2$, 99.999% trace metals basis), tris[2-(dimethylamino)ethyl]amine (97.0%) (Me_6TREN), N,N,N′,N″,N″-pentamethyldiethylenetriamine (PMDETA, 99.0%) tetramethyl orthosilicate (TMOS, 98.0%), naphthalene (99.0%), potassium (chunk, 98.0%), diphenylmethane (99.0%), hydrochloric acid solution (volumetric, 0.1 M, endotoxin free), propargyl bromide solution (80 wt. % in xylene), poly (ethylene glycol) methyl ether (Mw=5000 g/mol), trifluoroacetic acid (99.0%), tetraoctylammonium bromide (98.0%), lead acetate trihydrate ($Pb(CH_3CO_2)_2 \cdot 3H_2O$, 99.999% trace metals

basis), aluminum oxide powder (activated, neutral, Brockmann Activity I), α-bromoisobutyryl bromide (98.0%), tetrabutylammonium iodide (regent grade, 98.0%), oleylamine (technical grade, 70.0%) and oleic acid (technical grade, 90.0%) were purchased from Sigma-Aldrich and used as received. β-cyclodextrin (β-CD, >97.0%, Sigma-Aldrich) was recrystallized twice from water and dried under vacuum for 48 hours at 50°C. The traces of water were removed by azeotropic distillation in toluene for 2 hours at 110°C prior to the bromination reaction. Copper (I) bromide (CuBr, 99.999%, trace metals basis) and copper (I) chloride (CuCl, 99.995% trace metals basis) were stirred overnight in acetic acid, filtered, rinsed with ethanol and diethyl ether successively and dried in vacuum for overnight to remove any impurities prior to polymerization. Lead oleate was synthesized by reacting lead acetate with oleic acid under vacuum. Styrene (St, Sigma-Aldrich) and *tert*-butyl acrylate (*t*BA, Sigma-Aldrich) were washed with aqueous sodium hydroxide and DI water to remove inhibitors followed by drying by $MgSO_4$ and distilled over CaH_2 under reduced pressure prior to use. 4-vinylpyridine (4VP, Sigma-Aldrich) was distilled over CaH_2 under reduced pressure. All three monomers were stored in sealed ampoules under nitrogen and kept in the dark at 0°C. All other reagents were purified by common purification procedure.

4.2.2 Synthesis of Various Star-like Copolymers

Synthesis of Heptakis[2,4,6-tri-O-(2-bromo-2-methylpropionyl)-β-cyclodextrin) (i.e., 21Br- β-CD). β-CD (5.683 g, 5 mmol) was dried through azeotropic distillation and dissolved in 100 ml anhydrous NMP. α-bromoisobutyryl bromide (48.279 g, 210 mmol) was added drop-wise at 0°C to this mixture solution under magnetic stirring

using a dropping funnel. The reaction temperature was kept at 0°C for 2 h and then gradually increased to ambient temperature. The reaction solution was maintained at ambient temperature for 22 h for complete bromination reaction. The brown solution was transferred to separation funnel and diluted with 200 ml dichloromethane. The resulting solution was washed sequentially with saturated $NaHCO_3$, aqueous solution and DI water until the pH was above 4.5 to remove HBr produced in bromination reaction. The product was retrieved from the resulting solution by rotary evaporation, re-dissolved in acetone and precipitated in cold water three times to remove other impurities. The precipitant was re-dissolved in dichloromethane and dried with anhydrous $MgSO_4$. The final product was obtained by removing solvent by rotary evaporation.

Synthesis of Star-like Poly (4-vinlypyridine) Homopolymer (i.e., Star-like P4VP) Using 21Br-β-CD as Macroinitiators. Polymerization of 4-vinyl pyridine (4VP) was performed using standard Schlenk line. A mixture solution consisting of 21Br- β-CD (0.02 mmol), CuX (0.42 mmol, X=Cl or Br), CuX_2 (0.042 mmol), Me_6TREN (1.1 mmol), anhydrous 2-propanol (40 mL) and 4VP (40 mL) was undergone five freeze-pump-thaw cycles in an 150 mL ampoule to remove dissolved oxygen in solution and then placed in an oil bath preheated to 40°C for desired time. The 4VP homopolymerization was stopped by quenching in liquid N_2 and exposed to the air. The brown red solution was diluted with DMF and passed through an activated neutral alumina column to remove copper catalyst. The resulting solution was dried by rotary evaporation to remove excess 4VP monomer and solvent. The resulting dark brown solid was re-dissolved in 2-propanol and precipitated in cold hexane, yielding a yellow-red powder. The products were further purified by repeating this dissolution/precipitation process using 2-propanol as solvent and cold

hexane as precipitator until a white powder was obtained. This white product was dried over vacuum and stored at 0°C prior to the following chain extension reaction.

Synthesis of Star-Like Poly (4-vinlypyridine)-*block*-Poly (*tert*-butyl acylate) (i.e., Star-like P4VP-*b*-P*t*BA) by ATRP Using Star-Like P4VP as Macroinitiators. All chain extension reactions performed in an ampoule were conducted via using well-defined chlorine terminated star-like P4VP synthesized above as macroinitiators. The solution consisting of *t*BA, star-like P4VP, CuCl, $CuCl_2$, Me_6TREN (molar ratio=8000:10:10:1:11) in anhydrous DMF (1 mL *t*BA in 2 mL solvent) were degassed by three freeze-pump-thaw cycles in liquid N_2 and then placed in oil bath preheated to 60°C for desired time. The polymerization was quenched by immersing in liquid N_2 and then exposed to air. The crude product was diluted with DMF and passed through a neutral activated alumina column to remove copper catalyst. The raw product was obtained by removing the excess *t*BA and solvent (DMF) by rotvap. The resulting product was further purified by fractional precipitation using cold hexane as precipitator to remove residual *t*BA monomer and oligomer. The resulting white powder-like star-like PS-*b*-P*t*BA was dried at 40°C under vacuum to obtain pure star-like PS-*b*-P*t*BA. The final white product was stored at 0°C for the following chain extension reaction.

Synthesis of Azide-Functionalized Star-Like Poly (4-vinlypyridine)-*block*-Poly (*tert*-butyl acylate) (i.e., Star-like P4VP-*b*-P*t*BA-N_3). Purified star-like PS-*b*-P*t*BA (0.5 g) was dissolved in anhydrous DMF (10 mL) and sonicated for the complete dissolution of star-like diblock copolymers in DMF. Sodium azide (the molar ratio of Cl in star-like PS-*b*-P*t*BA : sodium azide =1:100) was added to the reaction solution and kept stirring for 24 h at ambient temperature. After that, the original reaction solution was diluted with DMF.

The product was obtained by precipitating in mixture solution consisting of water/methanol at 0°C (the volume ratio=1:1). This dissolution/precipitation process was repeated three times to remove excess NaN_3. The purified product was dried at ambient temperature under vacuum to remove any residual solvent and stored at 0°C prior to click reaction.

Synthesis of Alkyne Terminated Polyethylene Oxide (PEO). Diphenylmethylpotassium (DPMK) was prepared as describe elsewhere. [131] Briefly, 200 mL freshly dried THF and 15.4 g (120 mmol) naphthalene were added into 500 mL three-neck flask under argon protection. Freshly cleaned potassium (4.68 g, 120 mmol) was added into mixture solution and kept stirring for 4 h followed by addition of 22.2 g (132 mmol) diphenylmethane. The reaction temperature was gradually increased to refluxing temperature for 36 h. The mixture solution was titrated with 0.1 M HCl and the final concentration of DPMK is 0.5 M.

Alkyne terminated PEO was prepared by nucleophilic substitution of the hydroxyl group on poly (ethylene glycol) methyl ether into the alkyne group. Typically, 10 g poly(ethylene glycol) methyl ether (2 mmol) and 60 mL dry THF was added into 250 mL flask. The DPMK solution was introduced to this mixture solution under the protection of argon at 0°C. The solution was kept stirring at this temperature for 1h before 10 mmol propargyl bromide was added using a syringe pump for 2 h. The reaction temperature was gradually increased to ambient temperature and allowed the reaction for 24 h. After that, the solution was removed by a rotvap and alkyne terminated PEO was obtained by separation of the formed salts and precipitating in diethyl ether. The pure product was obtained by washing the raw product using diethyl ether twice, yielding a white powder

like sample. ^{1}H-NMR ($CDCl_3$) δ ppm: 2.44 (t, 1H, -$OCH_2C{\equiv}C\mathbf{H}$), 4.20 (d, 2H, -$OC\mathbf{H}_2C{\equiv}CH$), 3.38 (s, 3H, $C\mathbf{H}_3$-O-PEO), 3.60-3.70 (m, -$C\mathbf{H}_2C\mathbf{H}_2O$- of PEO main chain).

Synthesis of Star-Like Poly (4-vinlypyridine)-*block*-Poly (*tert*-butyl acylate)-*block*-Polyethylene Oxide by Click Reaction (i.e., Star-Like P4VP-*b*-P*t*BA-*b*-PEO). Star-like P4VP-*b*-P*t*BA-*b*-PEO was prepared by grafting alkyne terminated PEO onto star-like P4VP-b-PtBA-N_3 via the copper (I)-catalyzed alkyne-azide cycloaddition reaction. Briefly, 1 g star-like P4VP-b-PtBA-N_3 was dissolved into 40 mL anhydrous DMF followed by addition of 0.5 g alkyne terminated PEO and the system was purged by argon for 30 min before CuCl and Me_6TREN (molar ratio=1:1.1:1:2) were added into the reaction solution. The dissolved oxygen was removed by three freeze-pump-thaw cycles in liquid N_2 and then placed in oil bath preheated to 40°C for 24 h. After that, the crude product was diluted with 60 mL DMF and passed through a neutral activated alumina column to remove copper catalyst. The raw product was obtained by removing DMF by a rotvap and purified by washing with diethyl ether, yielding a white powder. The final product was dried under vacuum and stored at 0°C prior to perovskite nanoparticle (PNCs) synthesis.

Synthesis Linear P4VP-*b*-P*t*BA-*b*-PEO Triblock Copolymer for Control Experiment. Synthesis of linear P4VP-*b*-P*t*BA-*b*-PEO triblock copolymer was prepared in a similar way to star-like P4VP-*b*-P*t*BA-*b*-PEO. The only difference was 21Br- β-CD was replaced by α-bromoisobutyryl bromide used as initiator.

Synthesis of Star-Like Poly (4-vinlypyridine)-*block*-Poly (*tert*-butyl acylate)-*block*-Polystyrene (i.e., Star-like P4VP-*b*-P*t*BA-*b*-PS) by ATRP Using Star-Like P4VP-*b*-P*t*BA as Macroinitiators. Chain extension reactions with St was similar to the synthesis of star-like P4VP-*b*-P*t*BA. Briefly, the solution composed of St, star-like P4VP-*b*-P*t*BA, CuCl, $CuCl_2$, Me_6TREN (molar ratio=8000:10:10:1:11) in anhydrous DMF (1 mL St in 2 mL solvent) were charged into an ampoule, degassed by three freeze-pump-thaw cycles in liquid N_2 and then placed in oil bath preheated to 80°C for desired time. The polymerization was stopped by immersing in liquid N_2 and then exposed to air. The crude product was diluted with DMF and passed through a neutral activated alumina column to remove copper catalyst. The raw product was obtained by removing the excess St and DMF by rotvap. The resulting product was further purified by fractional precipitation using cold methanol/water (volume ratio=1:1) as precipitator and DMF as solvent to remove residual St monomer and oligomer. The resulting white powder-like star-like PS-*b*-P*t*BA-*b*-PS was dried at 40°C under vacuum to obtain white powder-like sample. The final white product was stored at 0°C prior to PNCs synthesis.

Synthesis of Star-like Poly (*tert*-butyl acylate) Homopolymer (i.e., Star-like P*t*BA) Using 21Br-β-CD as Macroinitiators. Polymerization of *tert*-butyl acylate (*t*BA) was performed in a way similar to star-like P4VP. A mixture solution consisting of 21Br-β-CD (0.04 mmol), CuBr (0.84 mmol), PMDETA (1.68 mmol), anisole (40 mL) and *t*BA (40 mL) was undergone three freeze-pump-thaw cycles in an 150 mL ampoule to remove dissolved oxygen in solution and then placed in an oil bath preheated to 60°C for desired time. The homopolymerization was stopped by quenching in liquid N_2 and exposed to the air. The resulting solution was diluted with chloroform and passed through an activated

neutral alumina column to remove copper catalyst. The resulting solution was dried by rotary evaporation to remove excess *t*BA monomer and solvent. The raw product was re-dissolved in acetone and precipitated in cold methanol/water (volume ratio=1:1), yielding a white powder. The products were further purified by repeating this dissolution/precipitation process using acetone as solvent and cold methanol/water as precipitator to remove linear P*t*BA homopolymer generated as side product during ATRP procedure.

Synthesis of Azide-Functionalized Star-Like Poly (*tert*-butyl acylate) (i.e., Star-like P*t*BA-N_3). Synthesis of star like P*t*BA-N_3 was followed similar procedure as that of star-like P4VP-*b*-P*t*BA-N_3.

Synthesis of Star-Like Poly (*tert*-butyl acylate)-*block*-Polyethylene Oxide by Click Reaction (i.e., Star-Like P*t*BA-*b*-PEO). Synthesis of star-like P*t*BA-*b*-PEO was followed similar procedure as that of star-like P4VP-*b*-P*t*BA-*b*-PEO via copper(I)-catalyzed alkyne-azide cycloaddition except that ligand was changed from Me_6TREN to PMDETA.

Synthesis of Star-Like Poly (acrylic acid)-*block*-Polyethylene Oxide (i.e., Star-Like PAA-*b*-PEO) by *in-situ* Hydrolysis of Poly (*tert*-butyl acylate) Block to Poly (acrylic acid) Block. *In-situ* conversion of P*t*BA to PAA was catalyzed by TFA. Typically, 400 mg star-like P*t*BA-*b*-PEO was dissolved in 20 mL DCM followed by addition of 1 mL TFA. The system was kept stirring at ambient temperature for 24 h before solvent and excess TFA were removed by a rotvap. The raw product was purified by washing with

mixture solution composed of DCM/ethanol (volume ratio=1:1), yielding a white product. The purified star-like PAA-*b*-PEO was stored at 0°C prior to PNCs synthesis.

Preparation of methylammonium halide (CH_3NH_3X, X=Br or I). CH_3NH_3X was synthesized by reaction of the methylamine with the corresponding acid. First, methylamine in absolute ethanol was cooled to 0°C and stirred at this temperature with the addition of HBr or HI using a dropping funnel. The molar ratio of CH_3NH_2 to corresponding acid is 1:1.2 for the complete consumption of CH_3NH_2. The mixture solution was kept stirring at 0°C for 2 h before the solvent was removed by a rotovap. The resulting product was recrystallized in ethanol twice and washed by anhydrous diethyl ether to yield white product. The residual solvent was removed by drying under vacuum prior to use.

Synthesis of Lead Bromide Nanoparticles ($PbBr_2$ NCs) tether with Poly (*tert*-butyl acylate)-*block*-Polyethylene oxide via Using Star-Like P4VP-*b*-P*t*BA-*b*-PEO as Nanoreactors. Poly (*tert*-butyl acylate)-*block*-Polyethylene oxide-capped $PbBr_2$ NCs (denoted as P*t*BA-*b*-PEO-capped $PbBr_2$ NCs) were prepared by employing star-like P4VP-*b*-P*t*BA-*b*-PEO as nanoreactors. Typically, 10 mg star-like P4VP-*b*-P*t*BA-*b*-PEO was dissolved in mixed solution consisting of 20 mL choloroform, 5 mL isopropanol and 3 mL methanol followed by addition of 385.06 mg Pb-oleate (0.5 mmol) under argon protection. The system was kept stirring for 2 h before 546.8 mg tetraoctylammonium bromide (1 mmol) was added into reaction solution, yielding light milky colloidal solution within 10 min. The solution was kept stirring at ambient temperature for another 2 h. The P*t*BA-*b*-PEO-capped $PbBr_2$ NCs were purified by washing with methanol twice and centrifuged at 6000 rpm. Preparation of P*t*BA-*b*-PS-capped $PbBr_2$ NCs was achieved via using star-like

P4VP-*b*-P*t*BA-*b*-PS as nanoreactors. The formation mechanism is similar to P*t*BA-*b*-PEO-capped $PbBr_2$ NCs.

Synthesis of Lead Bromide Nanoparticles ($PbBr_2$ NCs) tether with Poly (acrylic acid)-*block*- Polyethylene oxide via *in-situ* hydrolysis of P*t*BA-*b*-PEO-capped $PbBr_2$ NCs. Poly (acrylic acid)-*block*-Polyethylene oxide-capped $PbBr_2$ NCs (PAA-*b*-PEO-capped $PbBr_2$ NCs) were fabricated by *in-situ* hydrolysis of tethered diblock copolymer ligands (P*t*BA-*b*-PEO) into PAA-*b*-PEO in high boiling point organic solvent. Briefly, P*t*BA-*b*-PEO-capped $PbBr_2$ NCs were dissolved in diphenyl ether under strong sonication for 4 h to generate homogeneous solution. The solution was transferred into a three neck flask and the system was purged by argon for 20 min. After that, the solution was gradually heated to 200°C in 1 hour and maintained at this temperature for 1 h. The resulting $PbBr_2$ NCs were extracted via a separatory funnel twice and washed by water. The water soluble PAA-*b*-PEO-capped $PbBr_2$ NCs were obtained by removing water by a rotvap, yielding a white powder-like sample. In order to facilitate the formation of PNCs, the trace amount of water was further removed by a freeze dryer for 24 h. Preparation of PAA-*b*-PS-capped $PbBr_2$ NCs was followed exactly same procedure as to that of PAA-*b*-PEO-capped $PbBr_2$ NCs.

Synthesis of Methylammonium Lead Bromide/Silica Core/Shell Nanoparticles ($MAPbBr_3$/Silica CSNCs) tether with Polyethylene oxide as Ligands via Using PAA-*b*-PEO-capped $PbBr_2$ NCs as Nanoreactors. Synthesis of $MAPbBr_3$/silica CSNCs was achieved by *in-situ* conversion of $PbBr_2$ into $MAPbBr_3$ in the presence of MABr followed by hydrolysis of TMOS in the space occupied by PAA chains. In the typical synthesis of CSNCs, PAA-*b*-PEO-capped $PbBr_2$ NCs were dissolved in 20 mL mixture solution

composed of toluene and chloroform (volume ration=1:1) under argon protection. 0.16 M MABr solution (in isopropanol) was added dropwisely into this solution under vigorous stirring via a syringe pump for 1 h. The solution was kept stirring at 40°C for another 2 h before the excess of MABr was removed by centrifuge. Subsequently, 0.1 mL TMOS was added into the supernatant under vigorous stirring followed by purification using toluene as solvent and hexane as precipitator for three times. The purified $MAPbBr_3$/silica CSNCs were re-dissolved in toluene and can maintained stable for several weeks. Synthesis of PS-capped $MAPbBr_3$/silica CSNCs was followed exactly same procedure as to that of PEO-capped $MAPbBr_3$/silica CSNCs except that star-like P4VP-*b*-P*t*BA-*b*-PS was employed as nanoreactors instead of star-like P4VP-*b*-P*t*BA-*b*-PEO and heptane was used as precipitator during purification of PS-capped $MAPbBr_3$/silica CSNCs as opposed to be hexane.

Synthesis of Other Lead Based (i.e., Methylammonium Lead Iodide ($MAPbI_3$) PNCs Using Star-Like PAA-*b*-PEO as Nanoreactors. Preparation of PEO-capped $MAPbI_3$ PNCs was followed similar procedure as to that of P*t*BA-*b*-PEO-capped $MAPbBr_3$ PNCs. Briefly, 10 mg star-like PAA-*b*-PEO was dissolved in 10 mL methanol followed by addition of 331 mg $Pb(NO_3)_2$ (1 mmol) under argon protection. The system was kept stirring for 2 h before 166 mg KI (1 mmol) was added into reaction solution. The solution was kept stirring at ambient temperature for another 2 h. The PEO-capped PbI_2 NCs were purified by washing with methanol twice and centrifuged at 6000 rpm to discard any precipitants. The solvent was removed by a rotvap and the resulting $PbBr_2$ NCs solid were re-dissolved in toluene followed by addition of solution composed of MAI and isopropanol. The reaction solution was kept stirring at ambient temperature for another 2

h to enable complete conversion of PEO-capped PbI_2 NCs to PEO-capped $MAPbI_3$ PNCs. The $MAPbI_3$ PNCs was purified by centrifuge at 6000 rpm to remove excess of MAI. The further purification was achieved by using toluene as solvent and hexane as precipitator.

Synthesis of Oleylamine or Oleic Acid Capped $MAPbX_3$ (X=Br or I) PNCs for Control Experiment. All oleylamine or oleic acid capped $MAPbX_3$ PNCs were prepared by LARP according to well-established method.[2] In a typical synthesis of $MAPbBr_3$ PNCs, a mixture solution composed of MABr (0.16 mmol), $PbBr_2$ (0.2 mmol), octylamine (20 uL), oleic acid (0.5 mL) and DMF (5 mL) was dropped into 10 mL toluene which was poor solvent for organic-inorganic hybrid perovskite. Small short-chain ligand capped $MAPbBr_3$ PNCs were formed instantaneously with vigorous stirring, displaying very bright green color. The resulting PNCs were purified by centrifuge at 8500 rpm for 5 min. The supernatant was obtained, yielding a yellow-green solution with strong green PL emission. To maintain the colloidal stability of as-synthesized PNCs solution, no further purification step was performed. To preserve $MAPbI_3$ PNCs structural integrity and decomposition of PNCs, similar LARP procedure was conducted in glove box. The purification step was performed once and colloidal solution was used as control experiment.

4.2.3 Characterization

The molecular weight of hydrophobic star-like copolymers was measured by an agilent-1100 gel permeation chromatography (GPC) equipped with a G1362A refractive detector and a G1314A variable wavelength detector with one 5 μm LP gel column (500 Å, molecular range: 500 ~ 2×10^4 g/mol) and 5 μm LP gel mixed bed columns (molecular

range: 200 ~ 3×10^6 g/mol) with THF as mobile phase. The molecular weight of amphiphilic star-like copolymers was measured by a Shimadzu system (CTO-20A column oven, LC-20A pump and RID-10A refractive index detector) with DMF (stabilized with LiBr) as mobile phase. Both THF and DMF GPC were calibrated with PS standard samples. ^{1}H-NMR spectra were characterized by a Varian VXR-300 nuclear magnetic resonance spectroscopy. FT-IR spectra were obtained by a Magna-550 Fourier transform infrared spectrometer. The hydrodynamic size of analysis of star-like P4VP-*b*-PtBA-*b*-PS and P4VP-*b*-PtBA-*b*-PS triblock copolymers in DMF was performed using a DynaPro Nanostar (Wyatt Technology). For the purpose of accuracy, each dynamic light scattering measurement was performed on condition that a good correlation function was obtained. The X-ray diffraction (XRD) pattern was collected by a PANalytical X'Pert PRO X-ray diffractometer using Cu $K\alpha_1$ radiation (λ=1.541 Å) operating at 40 kV and 40 mA. The morphologies of $MAPbBr_3$/silica core/shell nanocrystals was imaged using a JEOL 100CX transmission electron microscopy (TEM) operating at 100 keV. UV-Vis spectra were recorded by Shimadzu UV-Vis spectrophotometer (UV-2600) with slit width=5.0 nm. The contact angle was measured at ambient (25°C) in air by a Ramé-hart Model 250 goniometer with distillation water used as contact angle analysis on regular glass substrate pre-treated by oxygen plasma in the clean room. Each contact angle measurement was repeated for three times in different locations. Photoluminescence (PL) spectra of PNCs solutions were collected using a Shimadzu RF-5301PC spectrofluorophotometer with the excitation wavelength of 380 nm. The photostability measurement test of the colloidal PS-capped $MAPbBr_3$/silica CSNCs toluene solutions were analyzed using all-transparent, quartz cuvette with total volume fixed at 1.5 mL. Prior to illumination, this colloidal solution was

checked to ensure that the maximum of PL intensity was below the highest value of instrument. The ultra-violet light source employed in the photostability investigations was provided by UVGL-25 UV lamp with 365 nm wavelength and power intensity of 720 $\mu W/cm^2$. The colloidal PS-capped $MAPbBr_3$/silica CSNCs toluene solutions was directly in contact with UV light source during continuous illumination. The evaporation of toluene due to the heat generated by UV lamp was replenished to guarantee the concentration of colloidal solution was constant. Therefore, the variation of intensity of PL spectra was independent upon the concentration. Every periodic interval, the PL spectra of the colloidal CSNCs toluene solutions after illuminating with 365 nm LED light were recorded. The moisture stability of PS-capped $MAPbBr_3$/silica CSNCs was measured in similar way by which colloidal solutions were intentionally exposed to certain level of humidity under the room light. Then, the PL spectra of the colloidal CSNCs toluene solutions were recorded.

4.3 Results and Discussions

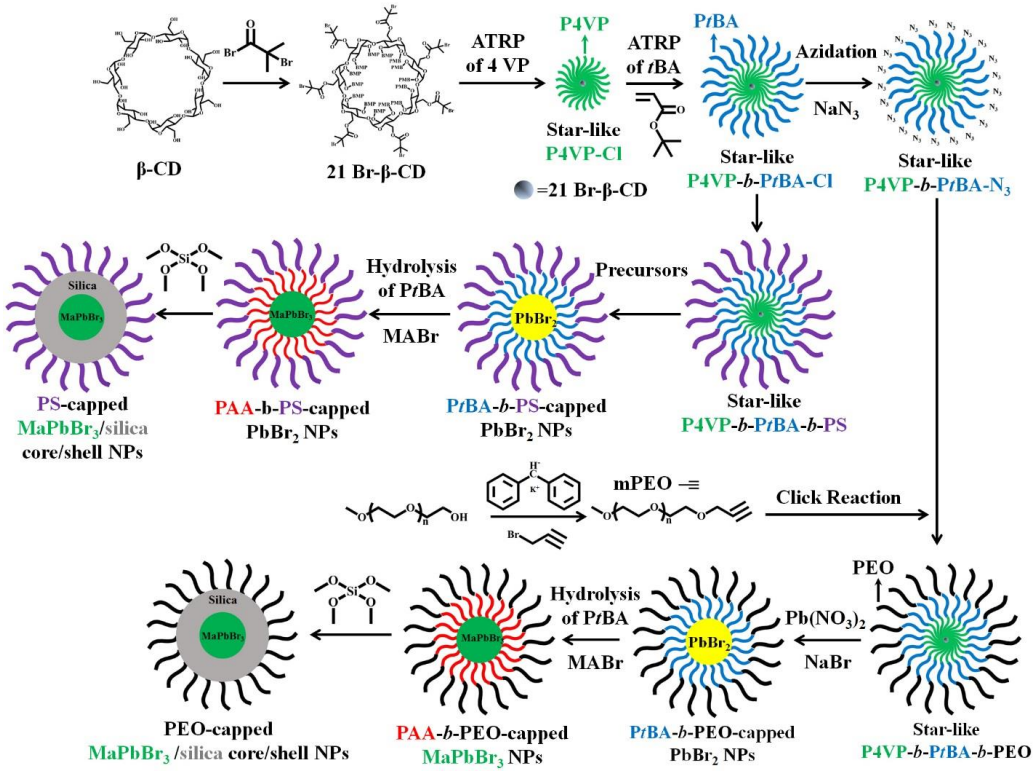

Figure 4.1 Schematic representation of synthetic approach for crafting PS-capped $MAPbBr_3$/silica core/shell NCs and PEO-capped $MAPbBr_3$/silica CSNCs utilizing star-like P4VP-*b*-P*t*BA-*b*-PS and P4VP-*b*-P*t*BA-*b*-PEO as nanoreactors, respectively.

Figure 4.1 described the schematic illustration of synthetic strategy for crafting different polymer capped organolead halide perovskite/silica CSNCs via using judiciously designed 21-armed star-like amphiphilic triblock copolymers as nanoreactors. Starting from β-cyclodextrin with 21 hydroxyl groups, almost 100% conversion of these hydroxyl groups to ω-bromide terminals (i.e., ATRP initiation sites) was confirmed by proton NMR. The resulting brominated β-cyclodextrin (denoted as 21-Br-β-CD) was then used as macroinitiator to prepare 21-arm star-like amphiphilic triblock copolymers with CuCl and $CuCl_2$ serving as co-catalysts. It is worthwhile to note that commonly used catalyst for

metal-mediated ATRP (e.g., CuBr or $CuBr_2$) is not a good candidate for preparing copolymer bearing pyridine groups due to the significant tendency for coupling between ω-bromide terminals and pyridine groups in P4VP block during polymerization, [23] which caused not only low solubility of copolymer in organic solvent but also intermolecular coupling issue (**Figure 4.2**) leading to ill-defined polymer gel or polymer network.

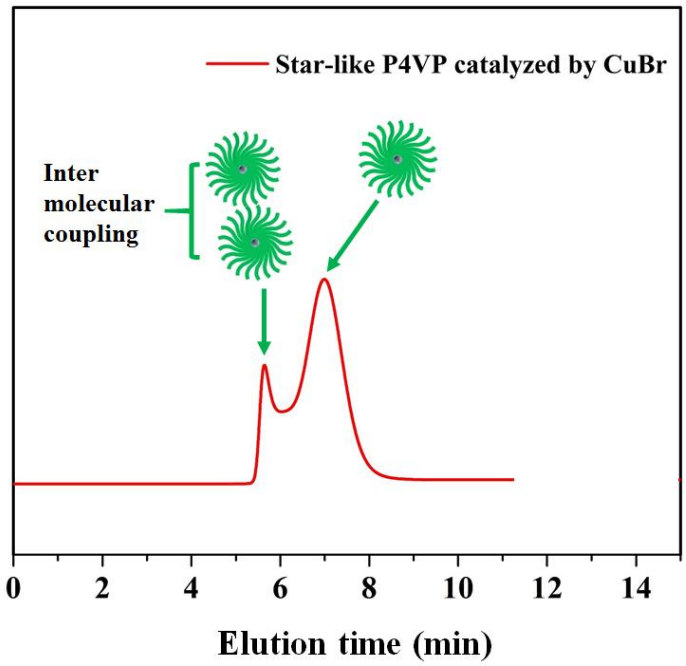

Figure 4.2 GPC (LiBr and DMF as mobile phase) trace of star-like P4VP-Br homopolymer prepared by utilizing CuBr and Me_6TREN as catalysts. The shoulder appeared in high molecular weight range suggests the inter-molecular coupling among star-like P4VP homopolymers.

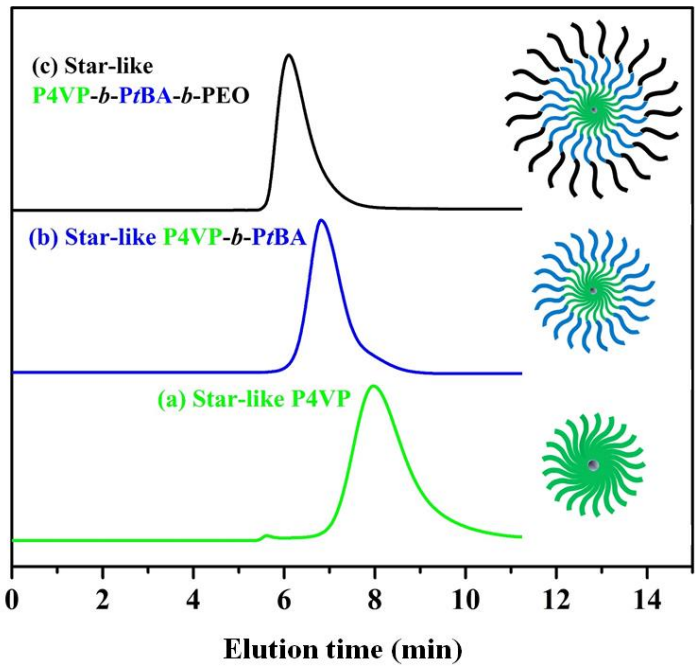

Figure 4.3 GPC (LiBr and DMF as mobile phase) traces of star-like homopolymer and block copolymers. (a) star-like P4VP, (b) star-like P4VP-*b*-P*t*BA and (c) star-like P4VP-*b*-P*t*BA-*b*-PEO.

However, substitution of CuBr and $CuBr_2$ with CuCl and $CuCl_2$ substantially suppressed the tendency for intermolecular coupling, leading to well-defined star-like P4VP homopolymer (**Figure 4.3**). In addition, instead of capitalizing on N,N,N′,N″,N″-pentamethyldiethylenetriamine or 2,2′-bipyridyl (commonly used ligands for ATRP of *t*BA and styrene), the preparation of star-like triblock copolymer via chain extension reaction or copper(I)-catalyzed alkyne-azide cycloaddition (CuAAC click reaction) was achieved in the presence of tris[2-(dimethylamino)ethyl]amine (Me_6TREN) serving as ligand owing to its bridged cyclam structure and strong coordination ability to copper catalyst compared to pyridine groups in P4VP block, thereby leading to high equilibrium constant of Cu(I)Cl/Me_6TREN complex (i.e., high polymerization rate). [1] As a result, the tendency for

thermopolymerizaation is largely suppressed. The utilization of Me_6TREN as ligand for ATRP of *t*BA or PS can also prevent the coordination of copper chloride catalyst with pyridine groups in P4VP block.

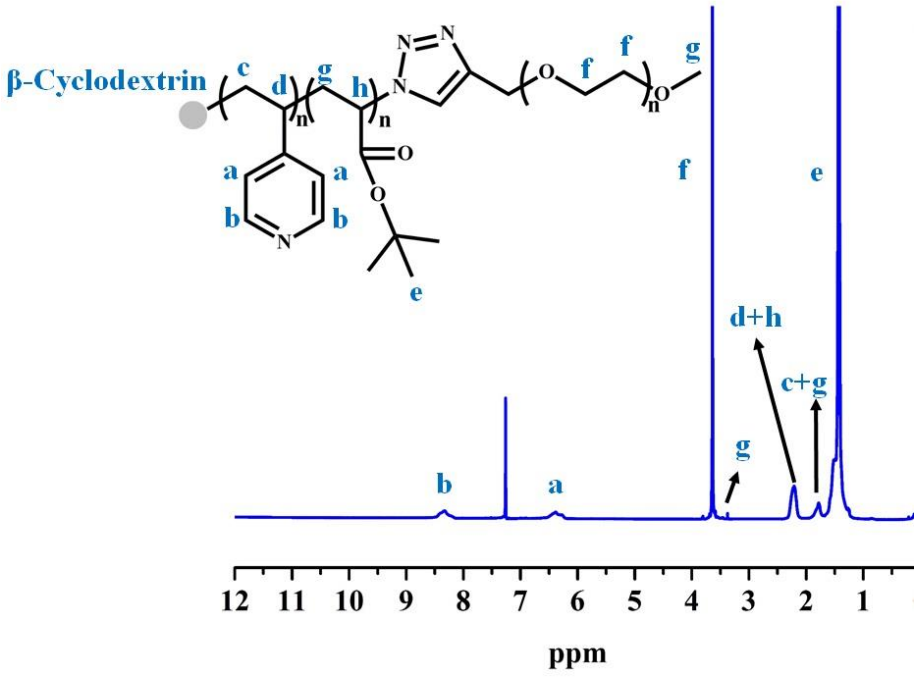

Figure 4.4 ^{1}H NMR spectra of well-defined star-like P4VP-*b*-P*t*BA-*b*-PEO triblock copolymer prepared by utilizing CuCl and Me_6TREN as catalyst.

Accordingly, star-like triblock copolymer P4VP-*b*-P*t*BA-*b*-PEO was successfully prepared by successive ATRP of 4VP and *t*BA in conjunction with click reaction with Cu(I)Cl+ $Cu(II)Cl_2$ /Me_6TREN serving as catalysts and ligand, respectively (**Figure 4.4**). Notably, all star-like polymers (i.e., homopolymer P4VP, diblock copolymer P4VP-*b*-P*t*BA and triblock copolymer P4VP-*b*-P*t*BA-*b*-PEO exhibited the monomodal gel permeation chromatograph (GPC) traces (**Figure 4.3**), suggesting there was no intermolecular coupling or residual homopolymer in the purified products.

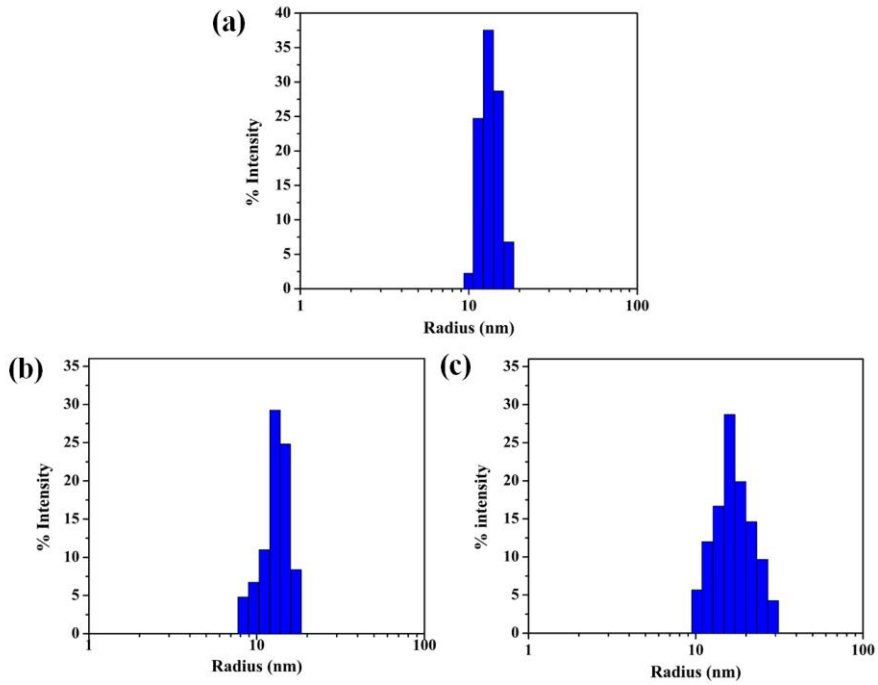

Figure 4.5 Dynamic light scattering (DLS) characterization of a series of star-like triblock copolymers in DMF (a) star-like P4VP-*b*-P*t*BA-*b*-PEO, (b) P4VP-*b*-P*t*BA-*b*-PS with M_{wPS}= 5 K and (c) P4VP-*b*-P*t*BA-*b*-PS with increased PS molecular weight to 10 K.

The successfully formation of unimolecular nanoreactors in organic solvent (e.g., dimethylformamide) via 21-arm star-like triblock copolymer P4VP-*b*-P*t*BA-*b*-PEO was further confirmed by dynamic light scattering (DLS), showing an unimolecular spherical micelles with narrow size distribution (**Figure 4.5**).

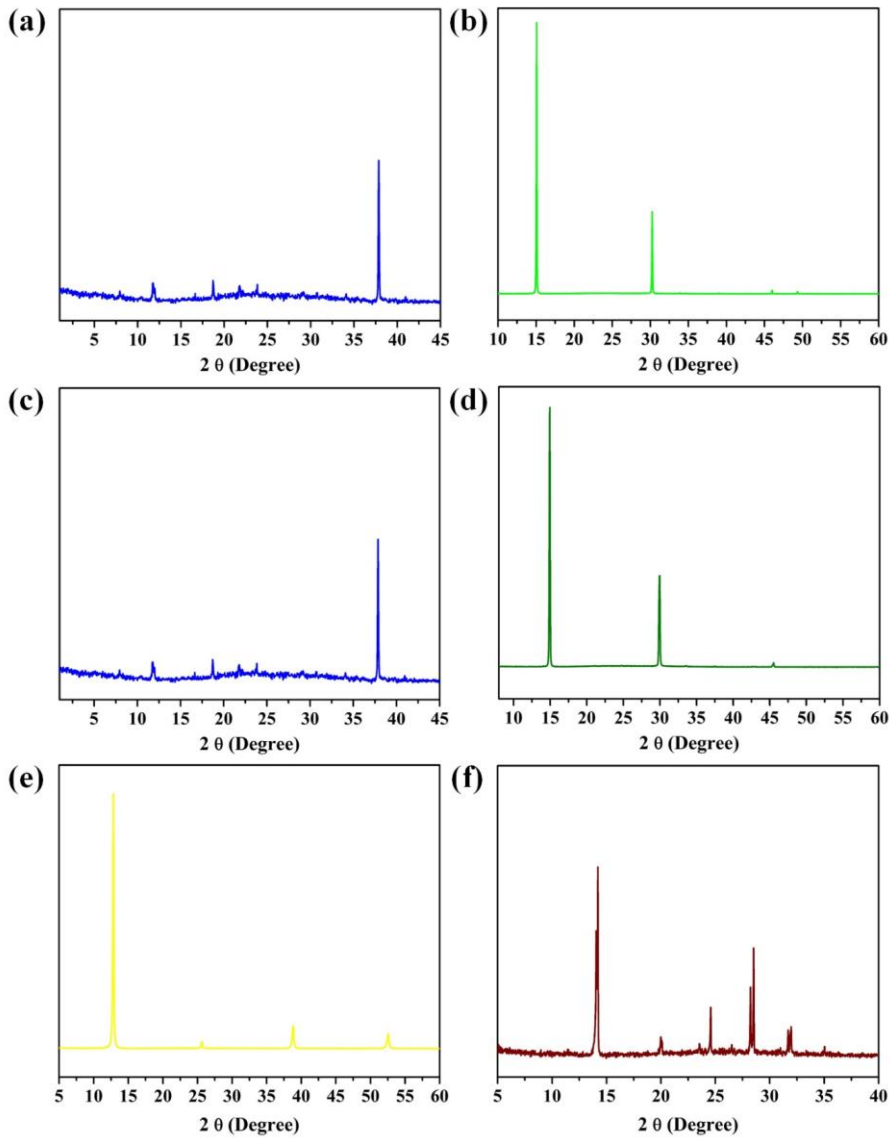

Figure 4.6 Two-step method for preparing organolead perovskite from lead halide thin film (a) XRD profile of spin coated $PbBr_2$ thin film on silicon substrate (b) XRD profile of $MAPbBr_3$ thin film prepared by spin-coating MABr isopropanol solution onto $PbBr_2$ thin film on silicon substrate (c) XRD profile of spin coated $PbBr_2$ thin film on silicon substrate (d) XRD profile of $FAPbBr_3$ thin film prepared by spin-coating FABr isopropanol solution onto $PbBr_2$ thin film on silicon substrate (e) XRD profile of spin coated PbI_2 thin film on silicon substrate (f) XRD profile of $MAPbI_3$ thin film prepared by spin-coating MAI isopropanol solution onto PbI_2 thin film on silicon substrate.

Judiciously designed 21-arm star-like triblock copolymer P4VP-*b*-P*t*BA-*b*-PEO was then utilized as nanoreactors for crafting $MAPbBr_3$ PNCs/silica core/shell nanocrystals (denoted as CSNCs). $MAPbBr_3$ PNCs/silica CSNCs formation was accomplished in a mixture solution composed of chloroform, isopropanol and methanol (chloroform/isopropanol/methanol=20/5/3, v/v/v) (see experimental section). Thermodynamically stable nanoreactors with narrow size distribution (i.e., unimolecular micelles) was formed in this co-solvent, leading to fully expanded P4VP chains and collapse of P*t*BA and PEO chains due to the fact that chloroform is good solvent for P4VP, P*t*BA and PEO whereas isopropanol and methanol are poor solvents for both P*t*BA and PEO. Under argon protection, pre-synthesized lead oleate was introduced into solution composed of co-solvent and star-like P4VP-*b*-P*t*BA-*b*-PEO triblock copolymer with vigorous stirring and preferentially formed complex with pyridine groups in the innermost P4VP blocks owing to strong coordination ability of pyridine groups to metal precursors whereas lead oleate had no interaction with P*t*BA and PEO blocks, both of which did not possess any functional groups to coordinate with lead oleate precursor. Subsequent introduction of tetraoctylammonium bromide (1 M in chloroform) prompted the ionic metathesis reaction [58] in the space populated by P4VP blocks, where lead oleate was selectively partitioned in P4VP blocks and eventually produced $PbBr_2$ NCs tethered with P*t*BA-*b*-PEO followed by thermolysis of P*t*BA blocks to obtain PAA-*b*-PEO-tethered $PbBr_2$ NCs. [132] One advantage of preparation of $MAPbBr_3$ PNCs via using pre-synthesized $PbBr_2$ NCs as template is that the thermolysis necessary to convert to P*t*BA to PAA has to be performed at high temperature which is sufficient to destroy PNCs, whereas $PbBr_2$ NCs are able to survive in this harsh environment. Since the bulk lead halide can be readily

converted to organolead halide perovskite by reacting with the corresponding organic salt (**Figure 4.6**), PAA-*b*-PEO-tethered $PbBr_2$ NCs was *in-situ* converted to PAA-*b*-PEO-tethered $MAPbBr_3$ NCs via mixing with methaylammonium bromide. Passivation of PNCs with silica shell was then accomplished via *in-situ* hydrolysis of tetramethyl orthosilicate (TMOS) in the space occupied by PAA chains. Because of this, thickness and growth of passivating layer are dictated by the PAA chains. It is worthwhile to note that the choice of alkoxide of silicon plays an essential role in formation of perovskite/silica CSNCs. Alkoxide of silicon precursor with comparatively slow hydrolysis rate (i.e., tetraethyl orthosilicate) resulted in quenching of the perovskite core NCs by destroying the structural integrity whereas alkoxide of silicon with high hydrolysis rate tended to preserve the structural integrity of PNCs, [122] thereby rendering formation of perovskite/silica CSNCs possible.

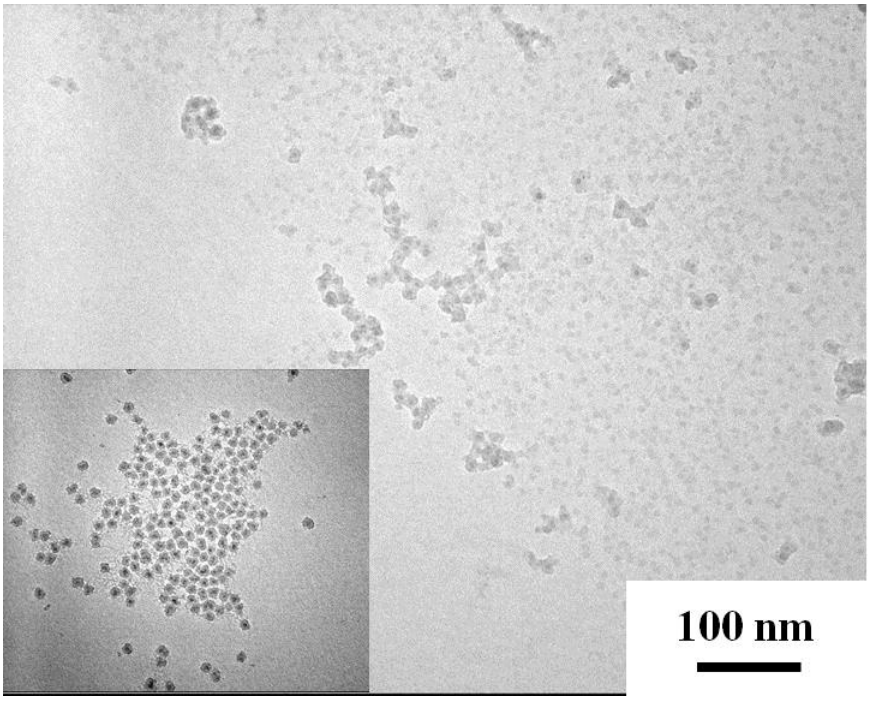

Figure 4.7 TEM images of $MAPbBr_3$/silica CSNCs crafted by exploiting the star-like triblock copolymer P4VP-*b*-P*t*BA-*b*-PEO as nanoreactors.

A representative transmission electron microscopy (TEM) image of $MAPbBr_3$/silica CSNCs crafted by exploiting the star-like triblock copolymer P4VP-*b*-P*t*BA-*b*-PEO as nanoreactors is shown in **Figure 4.7**, where the core-shell nanostructure is clearly evident owing to differential electron scattering ability of perovskite and silica. The excellent architectural control of the star-like copolymers originated from dynamic equilibria between dormant species and propagating radicals in ATRP not only secures the narrow molecular weight distribution (i.e., low polydispersity), thereby controlling the uniformity of as-synthesized NCs but also enables the readiness control of the length of individual block which dictates the dimension of CSNCs. [1] To further substantiate the essential role played by star-like P4VP-*b*-P*t*BA-*b*-PEO in the formation of $MAPbBr_3$/silica CSNCs, linear P4VP-*b*-P*t*BA-*b*-PEO prepared via similar methods is utilized to direct the growth of $MAPbBr_3$ NCs as control experiment. Not surprisingly, the use of linear triblock copolymer fails to mediate the growth of $MAPbBr_3$ NCs, yielding large particles with poor colloidal stability due to the failure of construction of thermodynamically stable unimolecular nanoreactors in mixture solution with addition of perovskite precursors (**Figure 4.8**).

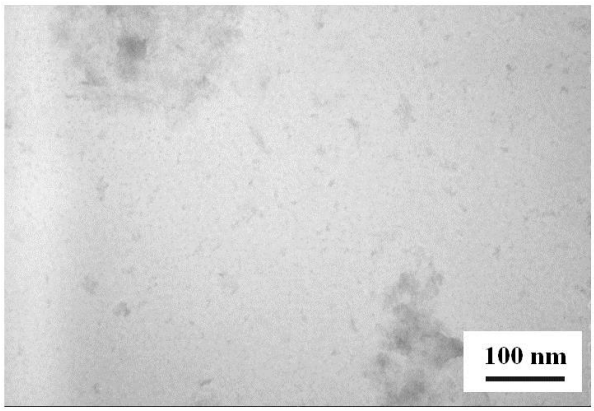

Figure 4.8 Preparation of $MAPbBr_3$ PNCs using linear P4VP-*b*-P*t*BA-*b*-PEO as nanoreactors.

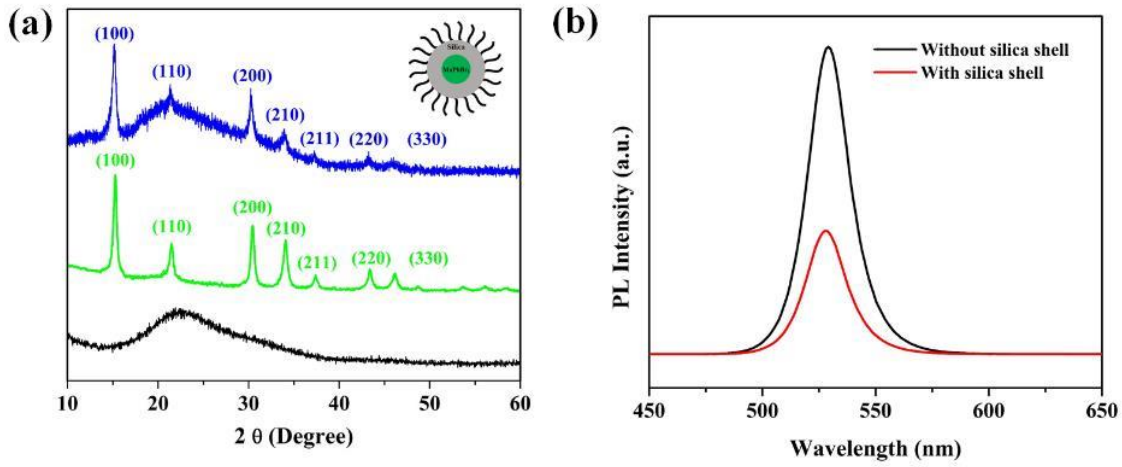

Figure 4.9 (a) XRD patterns and (b) PL spectra of $MAPbBr_3$ PNCs before and after coating of silica shell.

Figure 4.9 depicts the X-ray diffraction (XRD) profile of $MAPbBr_3$/silica CSNCs using star-like P4VP-*b*-P*t*BA-*b*-PEO as nanoreactors before and after passivation with silica shell as well as pure bulk silica as a control. Prior to the growth of silica shell, the position of characteristic peaks of XRD pattern (**Figure 4.9a**) is identical to bulk $MAPbBr_3$ perovskite, [55, 122] indicating the successful preparation of $MAPbBr_3$ NCs. The

pronounced broaden of diffraction peak further confirms the nature of nano-crystallinity of the as-synthesized product. After the successful growth of silica shell on the surface of $MAPbBr_3$ NCs, the diffraction pattern remains unchanged indicating that the structural integrity is preserved, while new diffraction peak appears in comparison to pristine $MAPbBr_3$ NCs without silica shell. This phenomenon in conjunction with XRD pattern of pure silica (lowest profile in **Figure 4.9a**) confirms the successful preparation of $MAPbBr_3$/silica CSNCs. The PL spectra prior to and after silica encapsulation was recorded (**Figure 4.9b**), indicating the position of peak of PNCs was located at 529 nm. More importantly, the position of PL peak did not exhibit appreciable peak shift after the growth of silica shell. This phenomenon further confirmed the structural integrity was preserved during silica coating process via *in-situ* hydrolysis of alkoxide of silicon precursor with high hydrolysis rate. UV-Vis spectrum of PEO-capped $MAPbBr_3$/silica CSNCs also exhibited a clear absorption peak at 525 nm.

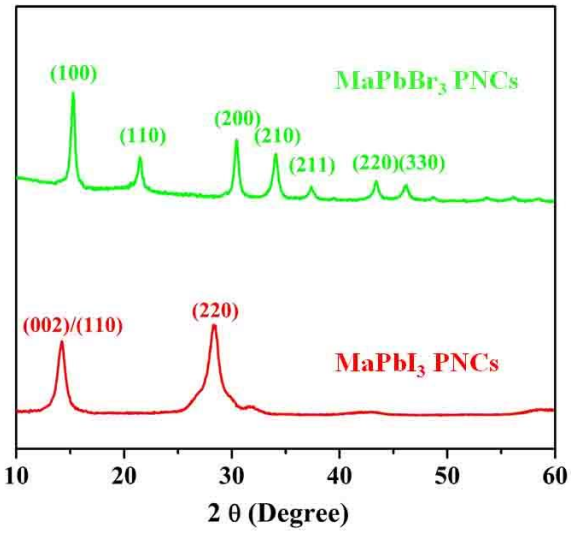

Figure 4.10 Comparison of XRD profile of $MAPbBr_3$ and $MAPbI_3$ PNCs prepared by using star-like PAA-*b*-PEO as nanoreactors.

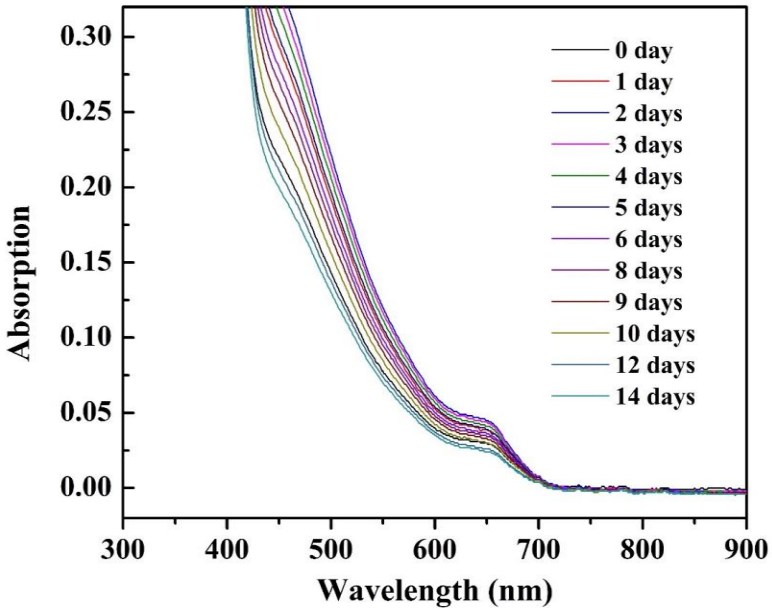

Figure 4.11 Time evolution of UV-Vis absorption spectra of 10 nm $MAPbI_3$ PNCs prepared via star-like PAA-*b*-PEO as nanoreactors under ambient condition.

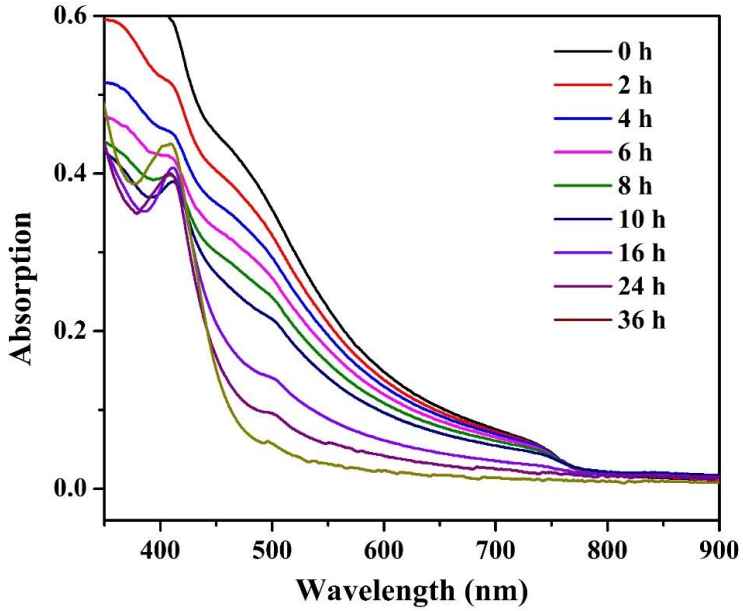

Figure 4.12 Time evolution of UV-Vis absorption spectra of $MAPbI_3$ PNCs prepared by dropping $MAPbI_3$ precursor solution (in DMF) into toluene with stirring in glove box.

Current successful preparation of $MAPbBr_3$/silica CSNCs inspires us to explore the possibility of general applicability of our approach by extending this method to iodide-substituted counterparts which are extremely sensitive to moisture and undergo rapid degradation even under ambient condition. For the simplicity, star-like PAA-*b*-PEO was employed as nanoreactors to direct the growth of $MAPbI_3$ PNCs. $MAPbI_3$ PNCs was prepared by *in-situ* conversion of PEO-capped PbI_2 NCs into corresponding PNCs by mixing with methylammonium iodide. XRD profile confirms the successful preparation of $MAPbI_3$ PNCs (**Figure 4.10**). More importantly, it is shown that the stability of as-synthesized $MAPbI_3$ PNCs is largely enhanced (**Figure 4.11**) in comparison to that of $MAPbI_3$ PNCs prepared via LARP route in glove box (**Figure 4.12**). On the contrary, preparation of $MAPbI_3$ PNCs via dropping perovskite precursor solution (in DMF) into toluene in open air encounters a challenge of fast degradation, resulting only $MAPbI_3$-H_2O intermediate (white flocculent precipitates) displaying no $MAPbI_3$ PNCs characteristic UV-Vis absorption peak.

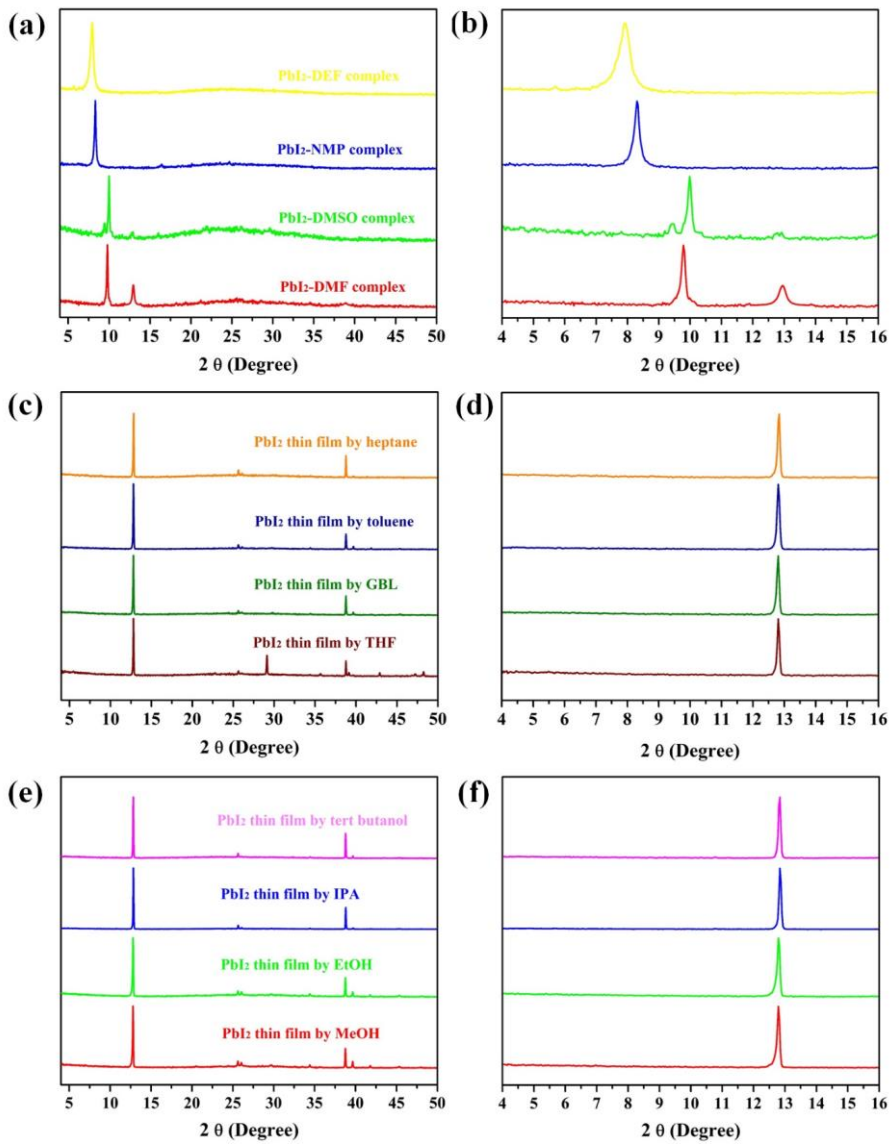

Figure 4.13 (a) XRD pattern of PbI_2 thin films spin-coated from various coordinate organic solvents (b) low diffraction angle of PbI_2 thin films spin-coated from coordinate solvents (c) XRD pattern of PbI_2 thin films spin-coated from various non-coordinate organic solvents (hydrocarbon solvents) (d) low diffraction angle of PbI_2 thin films spin-coated from non-coordinate organic solvents (e) XRD pattern of PbI_2 thin films spin-coated from various non-coordinate organic solvents (short-chin alcohols) (f) low diffraction angle of PbI_2 thin films spin-coated from non-coordinate organic solvents.

Previous studies indicated that good solvents for dissolving $PbBr_2$ or PbI_2 tended to coordinate with lead halide to form lead halide-solvent intermediate. It is shown that lead iodide has a strong propensity for forming lead halide-intermediate with various polar solvents, such as N,N-dimethylformamide (DMF), N-methyl-2-pyrrolidone (NMP), dimethyl sulfoxide (DMSO) and N,N-diethylformamide (DEF) (**Figure 4.13a and b**). Although lead halide has a decent solubility in these solvents especially DMF which is used for preparing perovskite precursor solution in LARP method, XRD patterns substantiate that the final product prepared from this precursor solution is PbI_2-solvent intermediate as opposed to be crystalline PbI_2 which has first primary diffraction peak at 12.7 °. However, all thin films casted from PbI_2-DMF solutions exhibited first primary diffraction peak below 12.7 °, suggesting the formation of PbI_2-solvent intermediate. The possible fast degradation mechanism is attributed to the fact that $MAPbI_3$ PNCs formed by co-precipitation of PbI_2-solvents intermediate with methyammonium iodide inevitably contain residual solvents molecules or intrinsic iodine vacancies in the crystal during the formation of PNCs. These vacancies and vacancies generated during the removal of solvent molecules and formation of PNCs process could transform $MAPbI_3$ PNCs into the $MAPbI_3$-water complex in the presence of trace amount of water from solvents or open air and cause degradation as well as the loss of PL. [57] To illustrate the solvent effects in stability of $MAPbI_3$ PNCs, we investigate the crystal structure of PbI_2 thin film casted from short chain alcohols and common hydrocarbon solvents. Systematic XRD patterns confirm that short chain alcohols (e.g., methanol, ethanol and isopropanol, etc.) and common hydrocarbon solvents (e.g., toluene, hexane, heptane, etc.) do not have coordination ability with lead halide to form intermediate (i.e., the first primary peaks are always located at

12.7 ° in **Figure 4.13 d, e and f**). As such, in order to decrease the defects in the PNCs, it is better to avoid using solvents (e.g., DMF) that can coordinate with lead halide to produce the intermediates. Therefore, the enhancement of stability of as-synthesized $MAPbI_3$ PNCs via our triblock copolymer nanoreactors strategy is owing to the fact that our method manages to craft PNCs in the absence of any organic solvents which can form intermediate with lead halide, thereby eliminating the possible crystal defects which can cause the rapid degradation of PNCs.

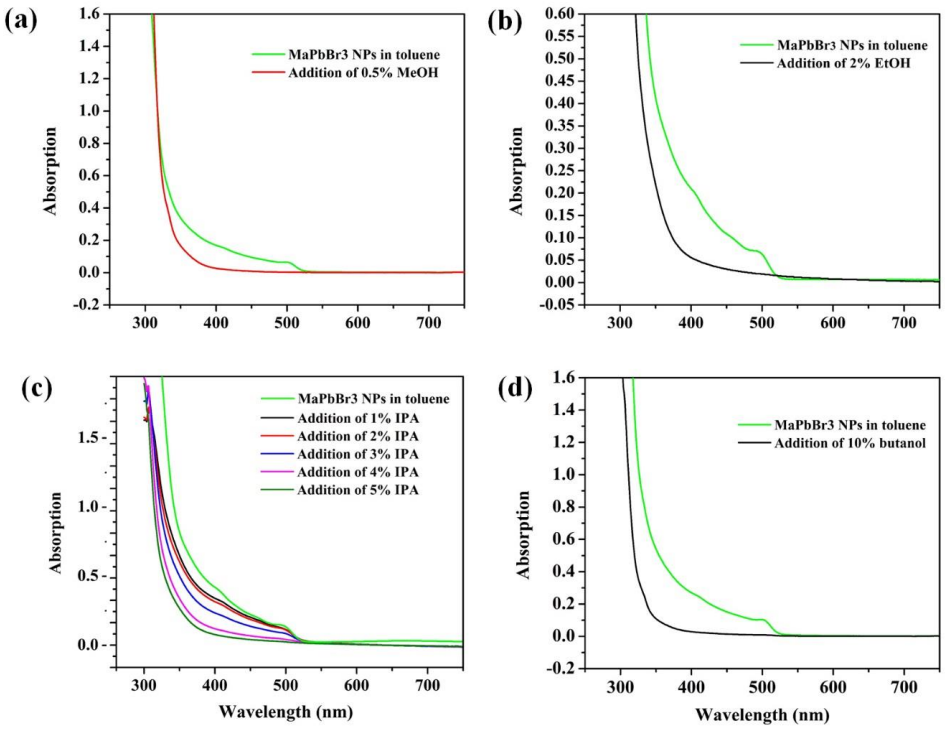

Figure 4.14 Stability of $MAPbBr_3$ NCs exposed to various common polar organic solvents (a) UV-Vis spectrum of $MAPbBr_3$ NCs in contact of MeOH, (b) UV-Vis spectrum of $MAPbBr_3$ NCs in contact of EtOH, (c) UV-Vis spectrum of $MAPbBr_3$ NCs in contact of IPA and (d) UV-Vis spectrum of $MAPbBr_3$ NCs in contact of butanol.

Meanwhile triblock copolymer nanoreactors offer not only a robust way to craft $MAPbI_3$ PNCs but also a gentle and non-destructive route to purify organolead iodide PNCs. It is still a great challenging task to translate conventional NCs purification method of organolead halide PNCs in light of their highly unstable surfaces and strong tendency for decomposition in several of polar solvents due to the fact that they are fully ionic nanocrystals. [133] Consequently, the highly ionic nature and dynamic binding of short-chain ligands on the surface of PNCs necessitate the delicate selection of destabilizing polar antisolvents to prevent damaging of PNCs during purification process. Saturated short-chain hydrocarbon alcohols used as precipitant in traditionally synthesized PNCs purification tend to partially damage the structural integrity of NCs depending on the dosage (**Figure 4.14**). Saturated short chain alcohols with longer hydrocarbon chains tend to have less negative effect on the degradation of PNCs. However, short chain alcohols with long hydrocarbon chains possess weak precipitating ability in comparison to alcohols with short hydrocarbon chains because the polarity of alcohols has an inverse correlation with the length of hydrocarbon chins. Nevertheless, introduction of 10% volume of butanol into purified PNCs colloidal solution is still sufficient to induce the full degradation (**Figure 4.14d**) due to the presence of hydroxyl groups. Previous DFT calculation indicated that oxygen and water molecules or OH ions have a strong tendency to bond to surface defects (e.g., halide vacancy and halide-ammonium vacancy) on $MAPbBr_3$ (010) plane due to the formation of hydrogen bonding, which is likely to reduce formation energy of other defects accelerating perovskite decomposition. [134] Experimental results in combination with DFT calculation indicate that deliberate efforts (i.e., the amount and type of alcohol) should be taken during PNCs purification to prevent damage of PNCs. Another widely

used solvent during purification process is acetone which has a decent precipitation ability and will not damage the surface of PNCs. Unfortunately, ligands required to stabilize the PNCs are also washed off during purification, causing the loss of colloidal stability and aggregation. On the contrary, our copolymer nanoreactors strategy circumvents both of these issues by the minimal using of weakly polar solvents during the formation of PNCs and completely avoiding the utilization of any destabilizing polar or protic antisolvents (i.e., acetone, methanol, ethanol, isopropanol or butanol), which is inaccessible to conventional purification methods. The presence of third block in triblock copolymers (i.e., PEO for star-like P4VP-*b*-P*t*BA-*b*-PEO) not only bestows an excellent colloidal stability due to the covalently bonding to PNCS but also first enables PNCs purification using solely nonpolar solvent (i.e., hexane in this case). As one of antisolvent for PEO, n-hexane with dipole moment and relative polarity as low as 0.08 D and 0.009 is an ideal candidate for serving as destabilizing solvent during PNCs purification process while preserving the integrity of surface of PNCs. The chemical properties of common organic solvents used in PNCs synthesis and purification are summarized in **Table 4.1**. It can be seen that the dipole moment and relative polarity of hexane is even lower than that of toluene which is widely used good solvent for PNCs prepared from conventional LARP method. In stark contrast to conventional purification method where hexane is used as good solvent, our synthetic route first achieves a goal where hexane is used as non-polar destabilizing antisolvents for PNCs (i.e., hexane as precipitant), thereby giving rise to excellent colloidal stability of PNCs and maintaining structural integrity without damaging the surface, causing the aggregation or dissolution issue of PNCs.

Table 4.1 Dipole moment and normalized polarity of common organic solvents.

Organic Solvent	Dipole Moment (D) [a]	Normalized Polarity [b]
Cyclohexane	0	0.0006
n-Hexane	0.08	0.0009
Toluene	0.31	0.099
n-Heptane	N/A	0.0012
Dichloromethane	1.14	0.309
Chloroform	1.15	0.259
Ethyl Ether	1.16	0.117
Chlorobenzene	1.54	0.188
Ethyl Alcohol	1.66	0.654
Isopropyl Alcohol	1.66	0.654
Tetrahydrofuran	1.75	0.207
Ethyl Acetate	1.88	0.228
Acetone	2.69	0.355
Methanol	2.87	0.762
Acetonitrile	3.44	0.46
N,N-Dimethylformamide	3.56	0.386
Tert-butyl Alcohol	3.9	0.389
Dimethyl Sulfoxide	4.1	0.444

a The values of dipole moment are collected from the following online source:

http://murov.info/orgsolvents.htm and http://www1.biologie.uni-hamburg.de/b-online/library/newton/Chy251_253/Lectures/Solvents/Solvents.html

b The normalized values are measured from the long-wavelength UV/Vis charge transfer absorption band of the negatively solvatochromic pyridinium N-phenolate betaine dyes and are calculated from the following equation:

$$E_T = h \times c \times \tilde{\nu} \times N_A$$

where *h* is Planck's constant, *c* is the velocity of light, $\tilde{\nu}$ is the wavenumber of the photon which produces the electronic excitation and N_A is Avogadro's number. The value is collected from *Solvents and Solvent Effects in Organic Chemistry*, Wiley-VCH Publishers, 3rd ed., 418-424, 2003.

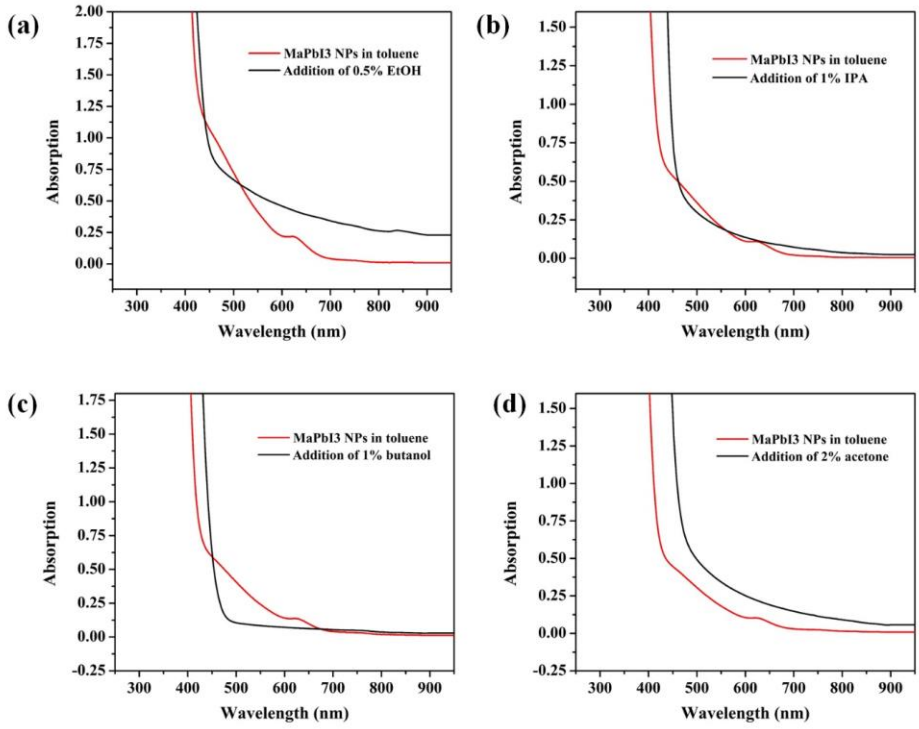

Figure 4.15 Stability of $MAPbI_3$ PNCs exposed to various common polar organic solvents (a) UV-Vis spectrum of $MAPbI_3$ NCs in contact of EtOH, (b) UV-Vis spectrum of $MAPbI_3$ NCs in contact of IPA, (c) UV-Vis spectrum of $MAPbI_3$ NCs in contact of butanol and UV-Vis spectrum of $MAPbI_3$ NCs in contact of acetone.

In comparison to bromine anions, the soft basic nature of iodine anions results in the weak acid-base interaction between halide anions and octylammonium ligands, thereby leading to the fact that the tendency for the loss of ligands is strong in iodine substituted PNCs isolation process compared to bromine substituted PNCs. The absorption peak of

$MAPbI_3$ PNCs exposed to different short chain alcohols is tracked by UV-Vis spectroscopy. It is shown that $MAPbI_3$ PNCs are more unstable compared to bromide-substituted counterparts (**Figure 4.15**), indicating the more stringent purification steps should be taken during PNCs washing procedure. It is worthwhile to note that even the addition of ACS grade acetone into $MAPbI_3$ PNCs in toluene is also likely to cause the degradation possibly probably due to the residual water in acetone, which causes the loss of UV-Vis absorption peak and transforms perovskite into white perovskite-water intermediate. Nevertheless, since the hydrogen bonding in PEO chains result in the insolubility of PEO in non-polar solvents (e.g., n-hexane), n-hexane with very low polarity and water content (**Table 4.1**) is exploited as precipitant, which preserves the structural integrity of $MAPbI_3$ PNCs during purification.

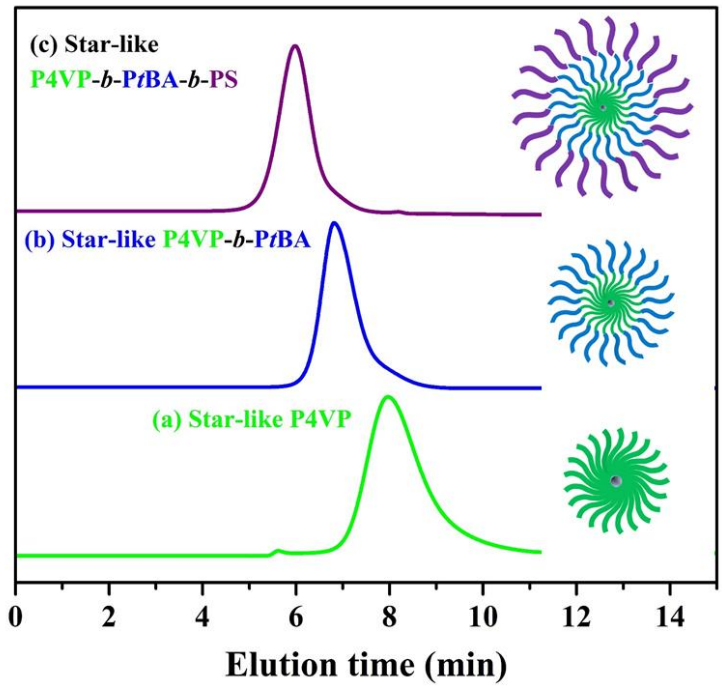

Figure 4.16 GPC (LiBr and DMF as mobile phase) traces of star-like homopolymer and block copolymers. (a) star-like P4VP, (b) star-like P4VP-*b*-P*t*BA (c) star-like P4VP-*b*-P*t*BA-*b*-PS.

The livingness nature of ATRP offers an unconventional strategy to readily tune the surface ligands of resulting $MAPbBr_3/SiO_2$ CSNCs prepared from star-like triblock copolymers without altering the core-shell morphology and damaging perovskite itself. Well-established ligand exchange strategies used in classical chalcogenide quantum dots fail to extend to PNCs because these ligand exchange processes involves exposing PNCs to harsh environment (e.g., involving use of protic solvent, like methanol), which can decompose or cause dissolution of PNCs. And highly dynamic ligand binding to PNC surface further renders surface post-functionalization a daunting task. [135] Unlike traditional ligand exchange approach, the inner (i.e., P4VP) and intermediate blocks (i.e., P*t*BA) of star-like triblock copolymer direct the growth of $MAPbBr_3$ and silica shell, respectively, whereas the outer blocks (i.e., PEO) serve as stabilizing ligands and can be substituted by other polymers without altering the morphology of CSNCs. PS-capped $MAPbBr_3/SiO_2$ CSNCs can be readily prepared by using star-like P4VP-*b*-P*t*BA-*b*-PS as nanoreactors via sequential ATRP of 4VP, *t*BA and St as (leftmost panel in **Figure 4.1**). Monomodal GPC traces (**Figure 4.16**) in conjunction with DLS measurement (**Figure 4.5b**) substantiate successful preparation of well-defined star-like P4VP-*b*-P*t*BA-*b*-PS triblock copolymers with narrow PDI, indicating the formation of unimolecular nanoreactors confirmed by DLS measurement (**Figure 4.5b**). Star-like P4VP-*b*-P*t*BA-*b*-PS was exploited as nanoreactors to craft PS-capped $MAPbBr_3$/silica CSNCs. In addition to achieve tunable surface chemistry in PNCs, star-like triblock copolymer nanoreactors also render $MAPbBr_3$/silica CSNCs compatible with different polymers (i.e., high processability), leading to hybrid

material consisting of stable PS-capped $MAPbBr_3$/silica CSNCs as nano-fillers and PS as matrix. [135] The versatility of polymer ligands is virtually unlimited (e.g., any polymer that can be grafted via ATRP or click reaction onto star-like copolymers can be utilized as ligands capping onto surface of PNCs), which affords a facile protocol to circumvent the issue regarding to conventional ligand exchange approach and integration PNCs into color conversion in LEDs.

More importantly, the stability of PS-capped $MAPbBr_3$/silica CSNCs was then tested under circumstances which are expected to degrade PNCs: repeated solvent washing, mixing different PNCs with different composition (i.e., chemical composition stability), mixing or immersion in protic polar solvents (i.e., moisture and protic polar solvents resistance), ultraviolet light irradiation (i.e., photostability).

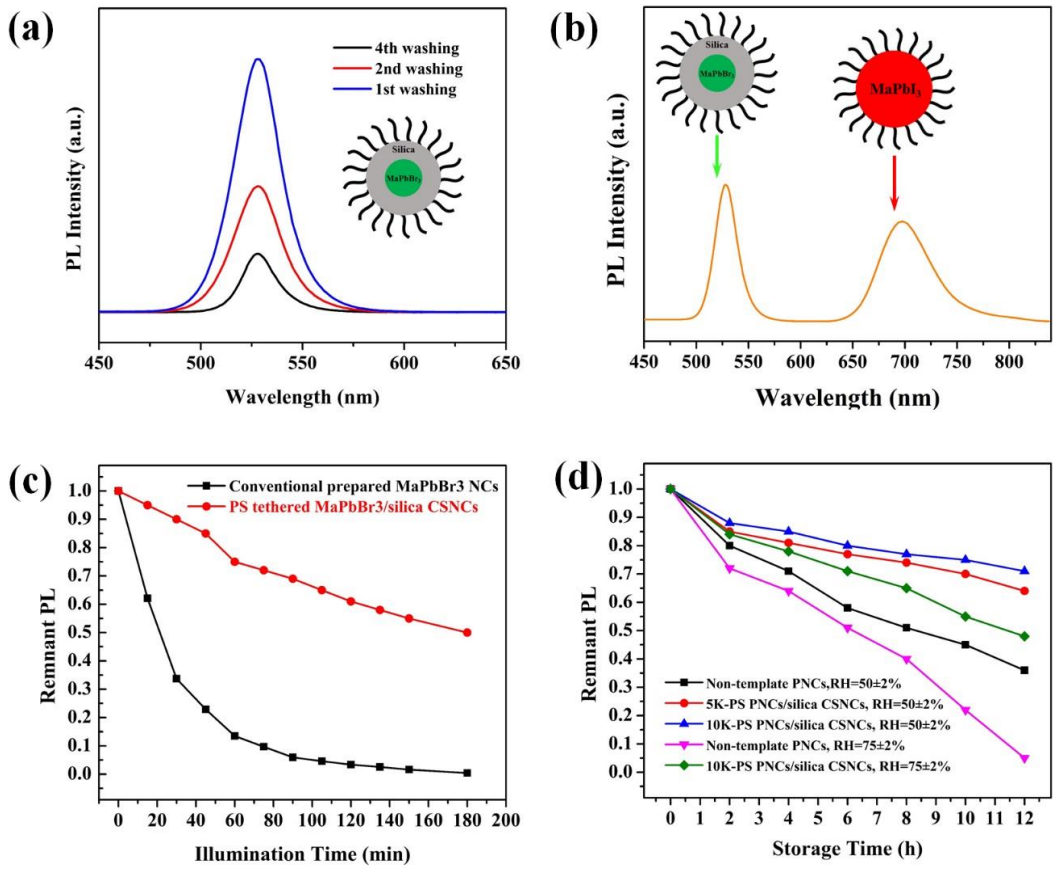

Figure 4.17 Stability test of PS-tethered $MAPbBr_3$/silica CSNCs in terms of (a) colloidal stability during repeated solvent washing, (b) chemical composition stability preventing anion exchange reaction, (c) photostability in response to continuous illumination of UV light at RH=55 ± 2% and (d) protic and moisture stability test of CSNCs stored in different moistures.

First, the PS-capped $MAPbBr_3$/silica CSNCs was exposed to repetitive organic solvent washing (**Figure 4.17**). It is well-established that conventionally prepared PNCs (e.g., all-inorganic or organic inorganic hybrid) tend to lose surface capped ligands (e.g., oleic acid or oleylamine) due to the highly dynamic binding of short-chain capping ligands, which can cause severe aggregation and decrease in PL. However, it is necessary to perform repetitive washing involving using good solvents and precipitants to purify as-

synthesized PNCs. Therefore, conventional methods require great deliberation during purification process to obtain clean PNCs colloidal solution while preventing the aggregation of PNCs. In contrast, our synthetic approach based on star-like P4VP-*b*-P*t*BA-*b*-PS triblock copolymer enables permanent and covalent bonding of PS onto the surface of $MAPbBr_3$/silica CSNCs, thereby conferring good colloidal stability to the CSNCs. Figure 4a indicates that the PL peak of $MAPbBr_3$/silica CSNCs does not exhibit appreciable position change even after four times of washing whereas conventionally prepared PNCs generally tend to aggregate, causing pronounced PL peak shift.

One advantage of PNCs in comparison to traditional cadmium based NCs is that the halide element of PNCs can be readily substituted, thereby giving rise to tunable wavelength throughout whole visible range. However, this anion exchange reaction may not be always favorable. One previous study demonstrated that this anion exchange process can be deterred via capping with branched short ligands. **Figure 4.17b** indicates the PL spectrum of mixing PS tethered $MAPbBr_3$/silica CSNCs with PEO-capped $MAPbI_3$ PNCs. The PL spectrum clearly shows two distinct peaks from $MAPbBr_3$/silica CSNCs and PEO-capped $MAPbI_3$ PNCs, respectively, suggesting the absence of anion exchange process. The appearance of these two distinct PL peaks as opposed to be only one peak due to anion exchange can be ascribe to the encapsulation of silica shell on the surface of $MAPbBr_3$ PNCs and PS tethered on the CSNCs. Silica encapsulation serves as a protection barrier to the exchange of halide anion between $MAPbBr_3$ PNCs and $MAPbI_3$ PNCs while surface tethered PS with bulky pendant groups (i.e., benzene groups) is also able to prevent this anion exchange process. In other word, our nanoreactors strategy achieves a core/shell-1/shell-2 morphology consisting of $MAPbBr_3$ PNCs as core, silica coating which can

preserve the chemical fidelity of PNCs as shell-1 and PS with abundant bulky pendant groups as shell-2 which is also beneficial for the prevention of anion exchange.

Moreover, the photostability of PS-capped $MAPbBr_3$/silica CSNCs is measured under the continuous illumination of 365 nm UV light with the short-chain ligands tethered $MAPbBr_3$ PNCs as control (**Figure 4.17c**). Conventionally prepared $MAPbBr_3$ PNCs underwent significantly PL drop under the continuous UV illumination at RH=55 ± 2% with the intensity of PL decreasing to almost zero after 120 min. On the contrary, the remnant of PL intensity of PS-capped $MAPbBr_3$/silica CSNCs still retained 50% of original value, suggesting excellent photostability of PS-capped CSNCs.

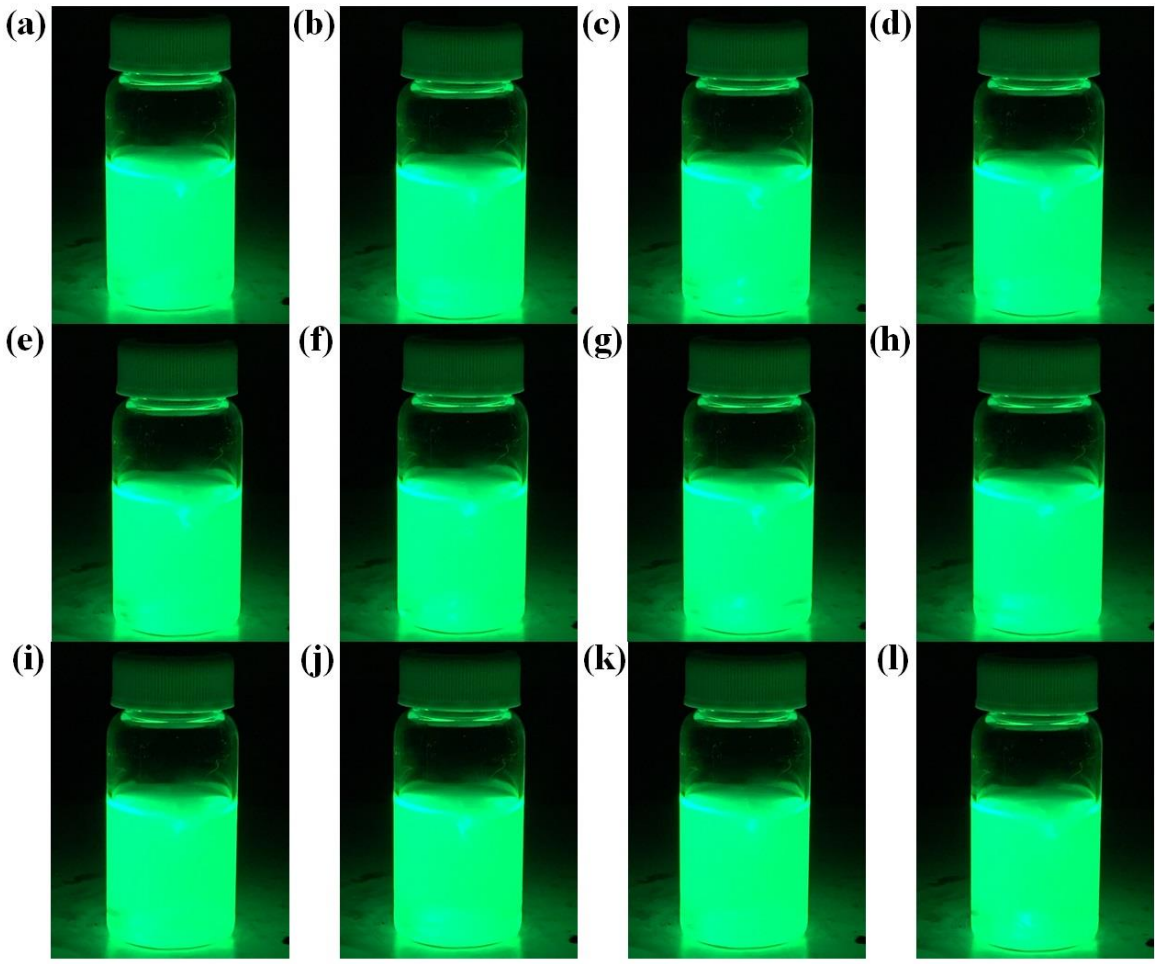

Figure 4.18 Time evolution of PS-capped $MAPbBr_3$/silica CSNCs dispersed in toluene with addition of 20% (volume) water under UV light (wavelength=370 nm) (a) 1 min (b) 3 min (c) 10 min (d) 30 min (e) 60 min (f) 90 min (g) 120 min (h) 150 min (i) 180 min (j) 210 min (k) 240 min (l) 300 min.

The moisture stability of PS-capped $MAPbBr_3$/silica CSNCs is measured under the different relative humidity. Not surprisingly, oleylamine and oleic acid capped $MAPbBr_3$ PNCs prepared from conventional route undergoes significant PL intensity drop when the PNCs are exposed to humid air. The PL intensity is almost decreased to zero in the environment with relative humidity of 75 ±2% after 12 h (**Figure 4.17d**). The presence of silica shell in conjunction with hydrophobic polystyrene with bulky pendent groups (i.e., core/shell-1/shell-2 morpholgoy) serves as an excellent diffusion barrier to confer moisture resistance to PNCs, thereby substantially increasing the stability of PNCs. Enhancement of stability can be ascribe to the presence of silica coating and the hydrophobic PS capped on the surface of CSNCs. The PS-capped $MAPbBr_3$/silica CSNCs toluene solution can still maintain very bright green color under the illumination of UV light with addition of water (**Figure 4.18**). The fact that capping hydrophobic PS onto $MAPbBr_3$/silica CSNCs is beneficial for the moisture stability is confirmed by the result that increasing the molecular weight of PS from 5 K to 10 K tends to improve the moisture stability with fixed RH.

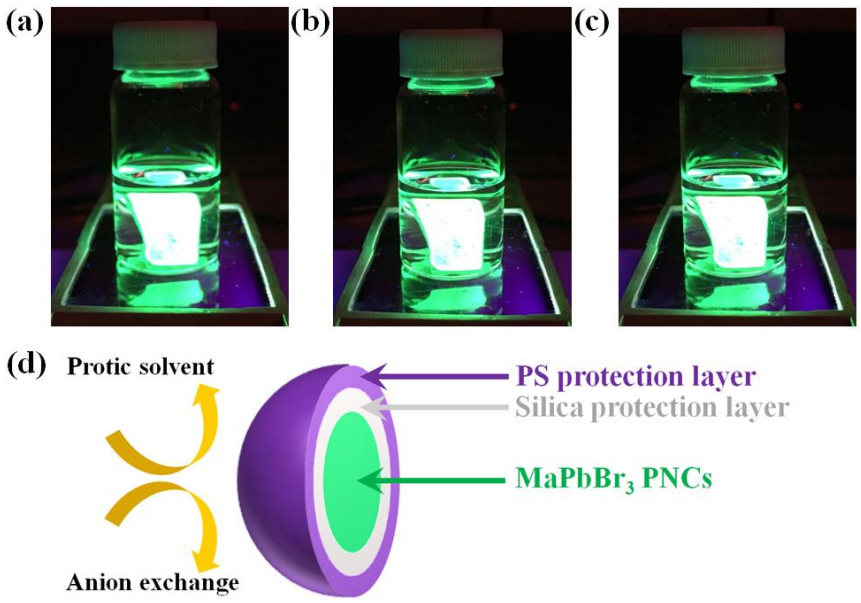

Figure 4.19 Time evolution of immersion of PS-tethered $MAPbBr_3$/silica CSNCs nanocomposite thin film spin-coated on SiO_2 substrate in DI water (a) 0 min, (b) 15 min, (c) 30 min and (d) schematic illustration of $MAPbBr_3$/silica/PS core/shell-1/shell-2 structure.

To further demonstrate our nanoreactors strategy retain the processability and stability of organic-inorganic hybrid PNCs, we fabricate 10 K PS-capped $MAPbBr_3$/silica CSNCs into thin film on oxygen plasma treated glass substrate by spin-coating. The emersion of the resulting nano-composite into DI water exhibited bright green light under the illumination of UV light after 30 min (**Figure 4.19a, b and c**). The reason for the superior water stability can be ascribe to the core/shell-1/shell-2 morphology whose silica encapsulation and collapsed PS chains can better shield $MAPbBr_3$ PNCs in contact with water molecules. Another possible explanation for enhanced photostability is the absence of photoinduced surface ligands which causes the formation of carrier trapping defects. [124]

4.4 Summary

We develop a novel and facile synthetic strategy based on judiciously designed star-like triblock amphiphilic P4VP-*b*-P*t*BA-*b*-PEO or P4VP-*b*-P*t*BA-*b*-PS copolymers for crafting perovskite/silica CSNCs with well morphology control, general applicability, tunable surface chemistry (i.e., stabilizing ligands can be tuned from hydrophilic PEO to hydrophobic PS with bulky pendent groups) and enhanced stability, which are not easily accessible to conventional routes (e.g., hot injection, LARP or currently available strategies for preparing stable PNCs). Distinct blocks in star-like triblock copolymers play different functions. The innermost P4VP and P*t*BA (hydrolyzed into PAA) blocks which can be readily tuned by ATRP process serve to govern the growth of methylammonium lead bromide PNCs owing to the strong coordination ability of pyridine groups and carboxylic acid groups in PAA, respectively. Silica passivation layer significantly improves the resistance ability to moisture and protic polar solvents by forming a protecting layer which impedes the diffusion of detrimental molecules to the core of CSNCs. The third blocks (e.g., PEO or PS) covalently tethered on methylammonium lead bromide PNCs not only function as stabilizing ligands, rendering excellent colloidal stability and non-polar solvent-based purification method possible, but also form an extra protecting layer consisting of PS with bulky benzene groups which repulse polar or protic solvent molecules (e.g., water and alcohol), thereby leading to the core/shell-1/shell-2 complex morphology. High-quality $MAPbBr_3$/silica CSNCs based on capitalizing on judiciously designed triblock copolymers as nanoreactors contribute to the fact that the structural integrity is largely preserved (i.e., enhancement of colloidal stability, chemical composition stability, moisture, polar or protic solvent resistance and photostability) while the solution

processability (i.e., solution processability is dependent upon the solubility of polymer ligands) and tunable surface chemistry (i.e., any polymer that can be prepared through ATRP or click reaction) are still maintained. We envision that our triblock copolymer nanoreactors strategy offer a robust platform for crafting diverse stable organic-inorganic hybrid PNCs/silica CSNCs covalently tethered with polymers bearing different functionalities (e.g., protecting function in our case or even conjugated polymers) for wide range application in solar energy harvesting, diverse LED devices and photonic application.

CHAPTER 5. DESIGN AND SYNTHESIS OF PLASMONIC/SEMICONDUCTOR CORE/SHELL NANOCRYSTALS WITH LARGE LATTICE MISMATCH AND THEIR ENERGY HARVESTING APPLICATION

5.1 Introduction

Nano-heterogeneous structures consisting of dissimilar components unique have been of interest to fundamental science and multifunctional device application due to the fascinating interaction of different components, leading to unique coupling effects. [136-139] For instance, Xu *et al.* reported the synthesis of Fe_3O_4/Au core/shell nanoparticles with shift of plasmonic peak owing to the increase in charge density and the amplitude of the free electron oscillation within the nanoparticles. [140] Generally, there are two ways to prepare nano-heterogeneous structures. One is through the epitaxial growth, which requires the moderate lattice mismatches. Obviously, the small lattice mismatches necessary for epitaxial growth severely restrict the general applicability of this method in fabrication of heterogeneous structures. The difficulty of epitaxy fabrication of CSNCs can be demonstrated by referring to the lattice parameter mismatches of common metallic materials and semiconducting materials. As can be seen from **Table 5.1**, the lattice mismatches between Au and cadmium based semiconducting materials are generally large than 40%.

Table 5.1 Lattice mismatch between common metallic NCs and semiconducting NCs. The lattice mismatch is calculated by (shell lattice parameter-core lattice parameter)/core lattice parameter. [141]

Core materials	Shell materials	Mismatch
Au (111)	CdS	42.7%
Au (111)	CdSe	49.1%
Au (111)	CdTe	58.9%
FePt (111)	CdS	49.5%
Pt (100)	CdS	48.3%
Pd (111)	CdS	49.6%

Another approach that can be used for preparing heterogeneous structures is via nonepitaxial growth. Currently, there is only one available nonepitaxial synthetic approach capable of preparing heterogeneous structure (e.g., core/shell structure) consisting of two components, especially metal-semiconducting, with very large lattice mismatch. [141] This non-epitaxial growth is achieved via preparation of metal NCs and deposition of silver shell on metal NCs followed by conversion of silver shell to diverse semiconducting shells. This pioneering work firstly demonstrated the successful nonepitaxial preparation of core/shell NCs (CSNCs) with very large lattice mismatches and superior dimension control (i.e., core diameter and shell thickness). However, this synthetic route did not demonstrate the CSNCs with relatively large size (i.e., total diameter>15 nm).

One issue regarding to the application of CSNCs in functional device is the efficient NC-to-NC carrier transportation. Traditionally prepared Au/CdS CSNCs are generally capped with long-chain hydrocarbon amines (e.g., oleyamine), [142] which isolate CSNCs from surrounding environment and impede effective carrier transportation. Moreover, the surface-capped ligands offering good colloidal stability and processability to CSNCs may

be detrimental to the chemical stability of active materials in optoelectronic devices (e.g., organic-inorganic hybrid perovskite), which can form unfavorable defects.

To address these issues mentioned above, in this chapter, we develop a facile and robust ***nonepitaxial*** synthetic strategies based on 21-arm star-like amphiphilic triblock copolymers (i.e., poly(4-vinylpyridine)-*block*-poly(*tert*-butyl acrylate)-*block*-oligomeric polyethylene oxide), denoted as star-like P4VP-*b*-P*t*BA-*b*-oligomeric PEO) as nanoreactors to craft Au/CdS CSNCs with length tunable ligands (e.g., the chain-length of PEO situated on the surface of CSNCs can be tuned from M_w=5000 to 550) and precise control over the dimension of core size and shell thickness. The lattice mismatch in this core/shell case is as large as 42.7% (**Table 5.1**), which is far beyond the lattice parameter required by epitaxial growth. Our triblock copolymer nanoreactors strategy offers another very effective alternative to the classic non-epitaxial growth method, preparing metal/semiconducting CSNCs with amphiphilic ligands. [142] The PEO or oligomeric-PEO blocks in triblock copolymers tethered on the surface of the as-synthesize Au/CdS CSNCs not only endow superior colloidal stability in various organic solvents, thereby leading to good processability, but also enable efficient carrier transportation owing to the short length of PEO without performing ligand exchange, as well as excellent chemical compatibility with perovskite material in optoelectronic devices. Furthermore, our triblock copolymer nanoreactors strategy demonstrates a potential way to achieve tunable surface chemistry in a sense that diverse, or virtually unlimited, clickable polymers with functionalities are able to be grafted onto the surface of CSNCs, which is inaccessible to classic non-epitaxil growth method. [141, 142] Finally, because of the aforementioned advantages of our approach, incorporation of as-synthetized short-chain oligomeric PEO capped Au/CdS CSNCs with well-controlled dimension is proved to be effective manner to enhance the power conversion efficiency of perovskite solar cells owing to the

significant photoinduced charge separation generated at the interface of metallic core and semiconducting shell.

5.2 Experimental Details

5.2.1 Materials

Gold(III) chloride hydrate (99.995% trace metal basis), Cadmium acetylacetonate (>99.5%), oleylamine (technical grade, 70%), sodium chunk, Poly(ethylene glycol) methyl ether(molecular weight=550) and borane tert-butylamine (>97.0%) were obtained from Sigma-Aldrich and used without purification. The chemicals necessary for crafting well-defined star-like P4VP-*b*-P*t*BA-*b*-PEO can be found in experimental section in chapter 4.

5.2.2 Star-like Copolymer Synthesis

The detailed synthesis procedure of various star-like polymers (e.g., star-like P4VP, P4VP-*b*-P*t*BA, azide terminated P4VP-*b*-P*t*BA and P4VP-*b*-P*t*BA-*b*-PEO) can be found in chapter 4 using copper mediated click reaction.

Synthesis of Alkyne Terminated Polyethylene Oxide and Alkyne Terminated oligomeric-PEO (PEO and oligomeric-PEO). Diphenylmethylpotassium (DPMK) was prepared as describe elsewhere. [131] The synthesis of alkyne terminated PEO followed same procedure reported in chapter 4. Diphenylmethylsodium (DPMNa) was prepared using the similar procedure of DPMK. The synthesis of alkyne terminated oligomeric-PEO was prepared by nucleophilic substitution of the hydroxyl group using DPMNa instead of DPMK due to the high reaction rate of DPMK.

Synthesis of Star-Like Poly (4-vinlypyridine)-*block*-Poly (*tert*-butyl acylate)-*block*-Oligomeric-Polyethylene Oxide by Click Reaction (i.e., Star-Like P4VP-*b*-P*t*BA-*b*-oligomeric-PEO). Star-like P4VP-*b*-P*t*BA-*b*-oligomeric-PEO was prepared by grafting alkyne terminated oligomeric-PEO onto star-like P4VP-b-PtBA-N_3 via the copper (I)-catalyzed alkyne-azide cycloaddition reaction. Briefly, 1 g star-like P4VP-b-PtBA-N_3 was dissolved into 40 mL anhydrous DMF followed by addition of 0.5 g alkyne terminated oligomeric-PEO and the system was purged by argon for 30 min before CuCl and Me_6TREN (molar ratio=1:1.1:1:2) were added into the reaction solution. The dissolved oxygen was removed by three freeze-pump-thaw cycles in liquid N_2 and then placed in oil bath preheated to 40°C for 24 h. After that, the crude product was diluted with 60 mL DMF and passed through a neutral activated alumina column to remove copper catalyst. The raw product was obtained by removing DMF by a rotvap and purified by washing with diethyl ether, yielding a white powder. The final product was dried under vacuum and stored at 0°C prior to CSNCs synthesis.

Synthesis of Gold Nanoparticles (Au NCs) tether with Poly (*tert*-butyl acylate)-*block*-Oligomeric-Polyethylene Oxide via Using Star-Like P4VP-*b*-P*t*BA-*b*-oligomeric-PEO as Nanoreactors. In a typical synthesis, 10 mg star-like P4VP-*b*-P*t*BA-*b*-oligomeric-PEO was dissolved in a mixture of dimethylformamide (DMF) and diphenyl ether (DPE) at DMF: DPE =9 : 1 (by volume) at room temperature under vigorous stirring for 24 h to form unimolecular nanoreactors followed by addition of an appropriate amount of HAuCl4. The mixture solution was kept stirring at ambient temperature for another 12 h to allow gold precursor selectively incorporated into the compartment composed of inner star-like P4VP blocks via the strong coordination interaction between pyridine groups

presented in P4VP blocks of star-like P4VP-b-PtBA-b-oligomeric-PEO and the metal moieties of Au precursors. Subsequent reduction of Au precursor in the presence of tBAB in the mixed solvents consisting of DMF/DPE (9/1, volumn) at room temperature for 2 h yielded Au NCs intimately and permanently tethered with PtBA-b-oligomeric-PEO blocks

Synthesis of Gold Nanocrystals (Au NCs) tether with Poly (acrylic acid)-*block*-Oligomeric-Polyethylene Oxide via in-situ Hydrolysis Surface-Capped Polymer Ligands. Synthesis of Au NCs tether with PAA-*b*-oligomeric-PEO was achieved via in-situ conversion of P*t*BA to PAA. P*t*BA-*b*-oligomeric-PEO capped Au NCs were hydrolyzed into PAA-*b*-oligomeric-PEO capped Au NCs with trifuoroacetic acid (TFA).

Synthesis of Au/CdS CSNCs Using PAA-*b*-oligomeric-PEO Capped Au NCs as Nanoreactors. Briefly, PAA-*b*-oligomeric-PEO capped Au NCs were dissolved in mixture solution consisting of DMF/DPE (volume ratio=9/1) followed by addition of cadmium acetylacetonate under argon protection. The solution was kept under vigorous stirring for 12 h to facilitate the coordination interaction between carboxylic acid groups in PAA chains and cadmium precursor cations. Sulfur dissolved in oleylamine was injected into reaction solution at room temperature followed by gradual increasing of temperature to 160 C to allow the crystallization of CdS on the surface of surface of Au NCs, thereby leading to the formation of plasmonic/semiconducting Au/CdS CSNCs. The PEO capped Au/CdS CSNCs were prepared in a similar way using star-like P4VP-*b*-P*t*BA-*b*-oligomeric-PEO as nanoreactors.

5.3 Results and Discussions

Figure 5.1 demonstrates the schematic illustration of synthetic strategy for crafting plasmonic/semiconducting CSNCs via using judiciously designed 21-armed star-like amphiphilic triblock P4VP-*b*-P*t*BA-*b*-oligomeric-PEO or P4VP-*b*-P*t*BA-*b*-PEO copolymers as nanoreactors. In chapter 4, we proved that the good ATRP control of P4VP contained copolymers relied on the utilization of copper (I) chloride and Me_6TREN to avoid formation of polymer gel or polymer coupling. In this chapter, all P4VP contained star-like copolymers were mediated via using CuCl as catalyst and Me_6TREN as ligand. The detailed information of various star-like amphiphilic star-like triblock copolymers is summarized in Table 5.2 Summary of molecular weight of amphiphilic star-like triblock copolymers and the corresponding dimension information of Au/CdS CSNCs.Table 5.2.

Table 5.2 Summary of molecular weight of amphiphilic star-like triblock copolymers and the corresponding dimension information of Au/CdS CSNCs.

Dimensions of Au/CdS CSNCs	$M_{n,P4VP}$	$M_{n,PtBA}$	$M_{n,PEO}$	PDI
13 ± 0.9 nm/ 1.5 ±0.4 nm	11,800	3,000	550	1.18
13 ± 0.9 nm/ 4 ±0.6 nm	11,800	9,600	550	1.17
13 ± 0.9 nm/ 4 ±0.6 nm	11,800	9,600	5000	1.12

M_n of each arm was calculated from ^{1}H-NMR data. The calculation method can be found in chapter 4. The polydispersity index, PDI of star-like triblock copolymer was determined by GPC.

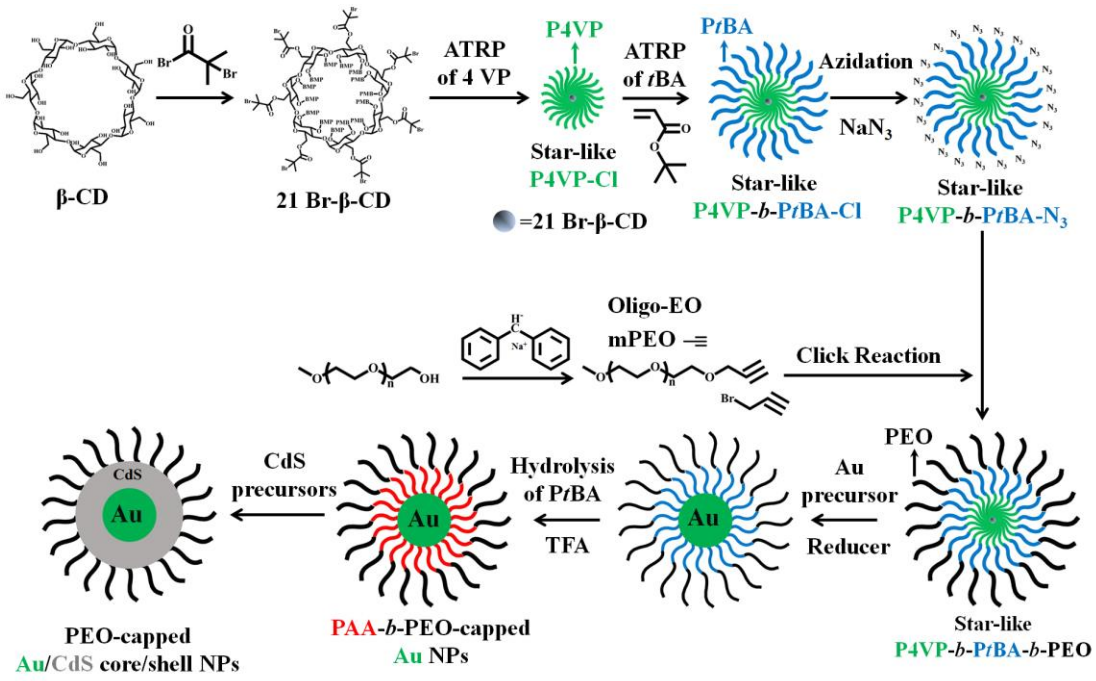

Figure 5.1 Schematic representation of synthetic approach for crafting PEO and oligomeric-PEO-capped Au/CdS core/shell NCs utilizing star-like P4VP-*b*-P*t*BA-*b*-PEO and P4VP-*b*-P*t*BA-*b*-oligomeric-PEO as nanoreactors.

Judiciously designed 21-arm star-like triblock copolymer P4VP-*b*-P*t*BA-*b*-oligomeric-PEO was then employed as nanoreactors for crafting plasmonic/semiconducting CSNCs. Thermodynamically spherical shaped nanoreactors with narrow size distribution (i.e., unimolecular micelles) was formed in mixed solution composed of DMF and DPE with volume ratio of 9:1. Unimolecular nanoreactors consisted of fully expanded P4VP chains and collapse of P*t*BA and oligomeric-PEO chains since DMF is good solvent for P4VP, P*t*BA and oligomeric-PEO whereas DPE is aniti-selective solvent for both of these blocks. Under argon protection, Au precursor was added into mixture solution composed of DMF/DPE and star-like P4VP-*b*-P*t*BA-*b*-oligomeric-PEO triblock copolymer with vigorous stirring and preferentially formed complex with

pyridine groups in the innermost P4VP blocks owing to strong coordination ability of pyridine groups to gold precursors whereas Au precursor had no interaction with P*t*BA and PEO blocks. Subsequent introduction of *t*BAB (i.e., reducing agent) prompted the reduction of Au precursor in the space occupied by P4VP in star-like triblock copolymers. The coating of CdS shell on Au core was realized by *in-situ* hydrolysis of P*t*BA to PAA in the presence of TFA followed by addition of CdS precursor and high temperature reflux.

A representative transmission electron microscopy (TEM) image of P*t*BA-*b*-oligomeric-PEO capped Au NCs with an average diameter of 13 ± 0.9 nm crafted by exploiting the star-like triblock copolymer P4VP-*b*-P*t*BA-*b*-oligomeric-PEO as nanoreactors is shown in **Figure 5.2a**. It is clearly evident that the well-defined amphiphilic star-like P4VP-*b*-P*t*BA-*b*-oligomeric-PEO triblock copolymers enable the successful fabrication of P*t*BA-*b*-oligomeric-PEO capped Au NCs with narrow size distribution. The formation of highly uniform Au NCs is attributed to the strong interaction of auric acid with pyridine groups in P4VP blocks as well as the second and third blocks not only serving as polymers ligands and controlling the growth of Au NCs but also imparting good colloidal stability in various organic solvent. Moreover, as-synthesized P*t*BA-*b*-oligomeric-PEO capped Au core NCs exhibited very pronounced plasmonic peak in visible range confirmed by UV-Vis absorption spectrum (**Figure 5.3**). Then, P*t*BA-*b*-oligomeric-PEO capped Au NCs was converted into PAA-*b*-oligomeric-PEO capped Au NCs for the subsequent growth of CSNCs. Generally, there are two different strategies capable of accomplishing this transformation. One is based on hydrolysis of P*t*BA via high temperature and another is based on hydrolysis with the aid of strong acid at room temperature. It was found that high temperature (i.e., around 200 °C for 2 h) necessary for

complete hydrolysis had a negative effect on the morphology of as-synthesized Au NCs (**Figure 5.2b**) due to the fact that the melting point of Au NCs was decreased due to the high surface energy. [143] The shape change of Au NCs from almost perfect sphere to distorted sphere also posed a negative effect on the morphology-dependent plasmonic properties of Au NCs, displaying wide the LSPR peak. In addition, this shape change effect can be clearly detected by UV-Vis absorption spectrum (**Figure 5.3**). However, hydrolysis of P*t*BA in the presence of TFA at room temperature had negligible effect on the shape of Au NCs without deforming Au NCs, thereby preserving the plasmonic property. Furthermore, the colloidal stability in terms of excellent solubility in diverse organic solvents (e.g., chloroform, toluene, dichlorobenzene and DMF) is owing to the presence of P*t*BA-*b*-oligomeric-PEO capped Au NCs.

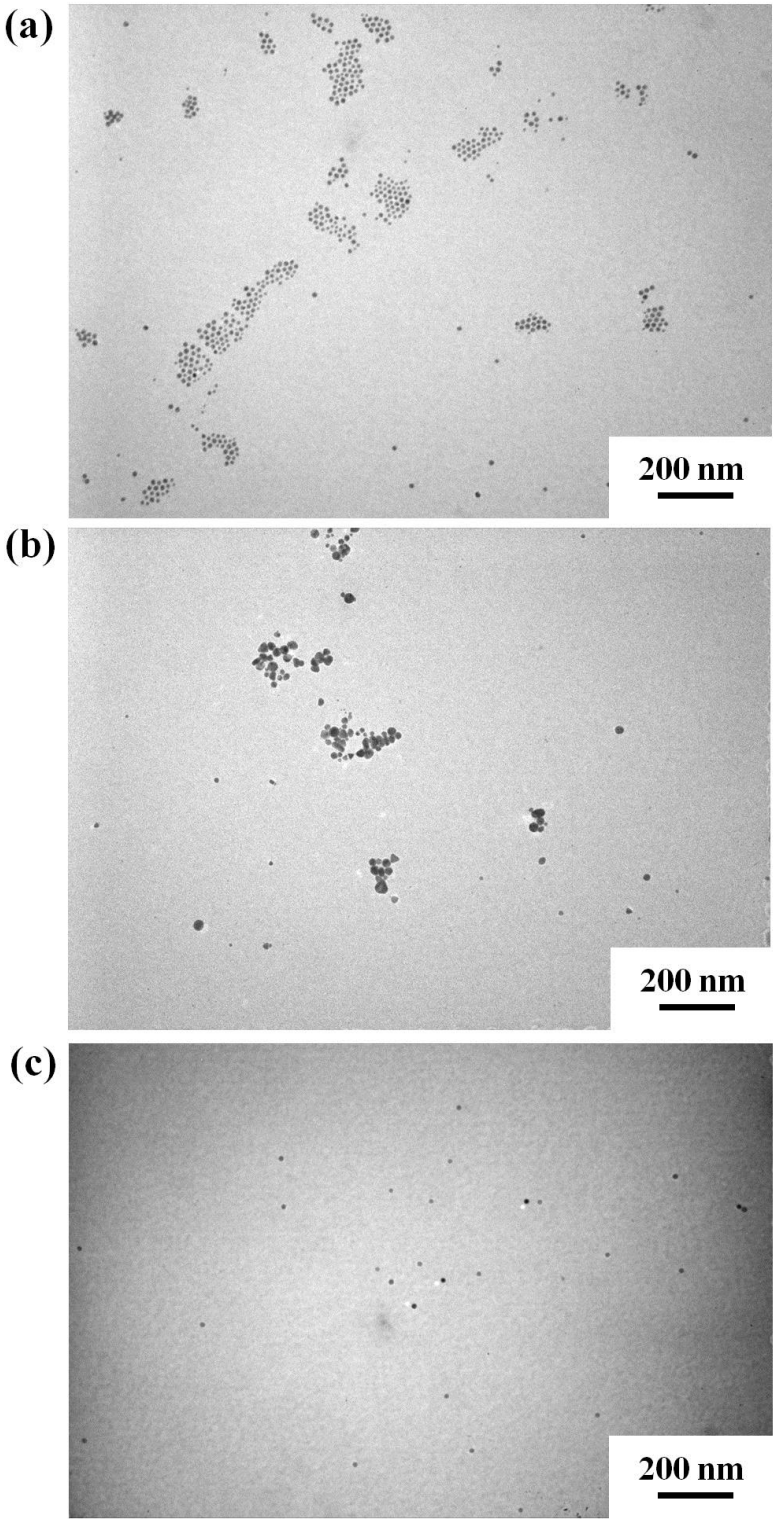

Figure 5.2 TEM images of (a) P*t*BA-*b*-oligomeric-PEO capped Au core NCs with diameter=13 ± 0.9 nm (b) PAA-*b*-oligomeric-PEO capped Au core NCs prepared by

thermolysis method and (c) PAA-*b*-oligomeric-PEO capped Au core NCs prepared by hydrolysis of TFA.

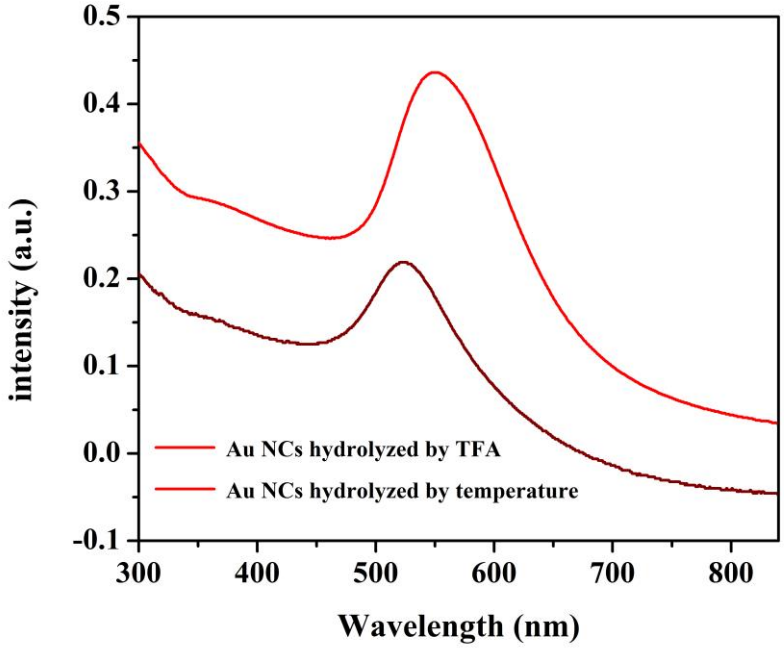

Figure 5.3 UV-Vis absorption spectra of (a) P*t*BA-*b*-oligomeric-PEO capped Au core NCs in toluene solution and (b) PAA-*b*-oligomeric-PEO capped Au core NCs via high temperature hydrolysis method in DMF solution.

Subsequently, PAA-*b*-oligomeric-PEO capped Au core NCs were employed as nanoreactors to fabricate oligomeric-PEO capped Au/CdS CSNCs with addition of CdS precursors. The successful preparation of oligomeric-PEO capped Au/CdS CSNCs can be ascribe to the strong coordination ability between carboxylic acid groups in PAA chains and metal moieties. Because of this, PAA-*b*-oligomeric-PEO capped Au core NCs were able to selectively coordinate CdS precursors from surrounding reaction medium and eventually lead to crystallization of CdS on Au NCs at high temperature. It is worthwhile to note that the reaction temperature for growing CdS shell is below refluxing temperature

of mixture solution (DMF/DPE) to ensure that the Au NCs will not undergo shape change during the shell growth step. Refluxing colloidal Au NCs in DMF/DPE for long time is still sufficient to induce unfavorable morphology change, which in turn alternates LSPR property of Au NCs. The successful preparation of Au/CdS is clearly evident in Figure 5.4a, displaying dark core with diameter=13 ± 0.9 nm and light shell with thickness=1.5 ±0.4 nm. The pronounced image contrast is ascribe to the significantly different electron scattering ability of metallic Au and semiconducting CdS. In contrast to conventional synthetic routes to CSNCs, our nanoreactors strategy offers a facile and robust nonepitaxial way to readily control the dimension of core diameter and shell thickness via simply varying the length of P*t*BA (i.e., subsequently hydrolyzed into PAA) blocks of star-like triblock copolymers, which can be easily achieved by controlling the polymerization time. For instance, increasing molecular weight of P*t*BA from 3K to 9.6K enables the fabrication of Au/CdS CSNCs with increased shell thickness (i.e., from 1.5 ±0.4 nm to 4 ±0.6 nm) (Figure 5.4b).

Another interesting phenomenon is that although there is NCs aggregation due to the short length of oligomeric-PEO (i.e., molecular weight=550), oligomeric-PEO is still sufficient to impart a descent colloidal stability to Au/CdS CSNCs. The purified colloidal solution can maintain stability over several weeks without noticeable precipitate. Admittedly, traditionally synthesized CSNCs exhibited excellent colloidal stability due to the surface tethered ligands (e.g., oleylamine and oleic acid) with high surface capping density. Nonetheless, ligand exchange process has to be performed to substitute this high density, long-chain ligands to facilitate the carrier transportation. The low molecular weight of oligomeric-PEO not only enables the preparation of CSNCs with good colloidal

stability and investigation of coupling effect between metal and semiconductor, but also imparts amphiphilicity to Au/CdS CSNCs because oligomeric-PEO has superior solubility in polar solvents (e.g., water, DMF and methanol) as well as non-polar solvents (e.g., chloroform and toluene), which is inaccessible to conventional synthetic routes.

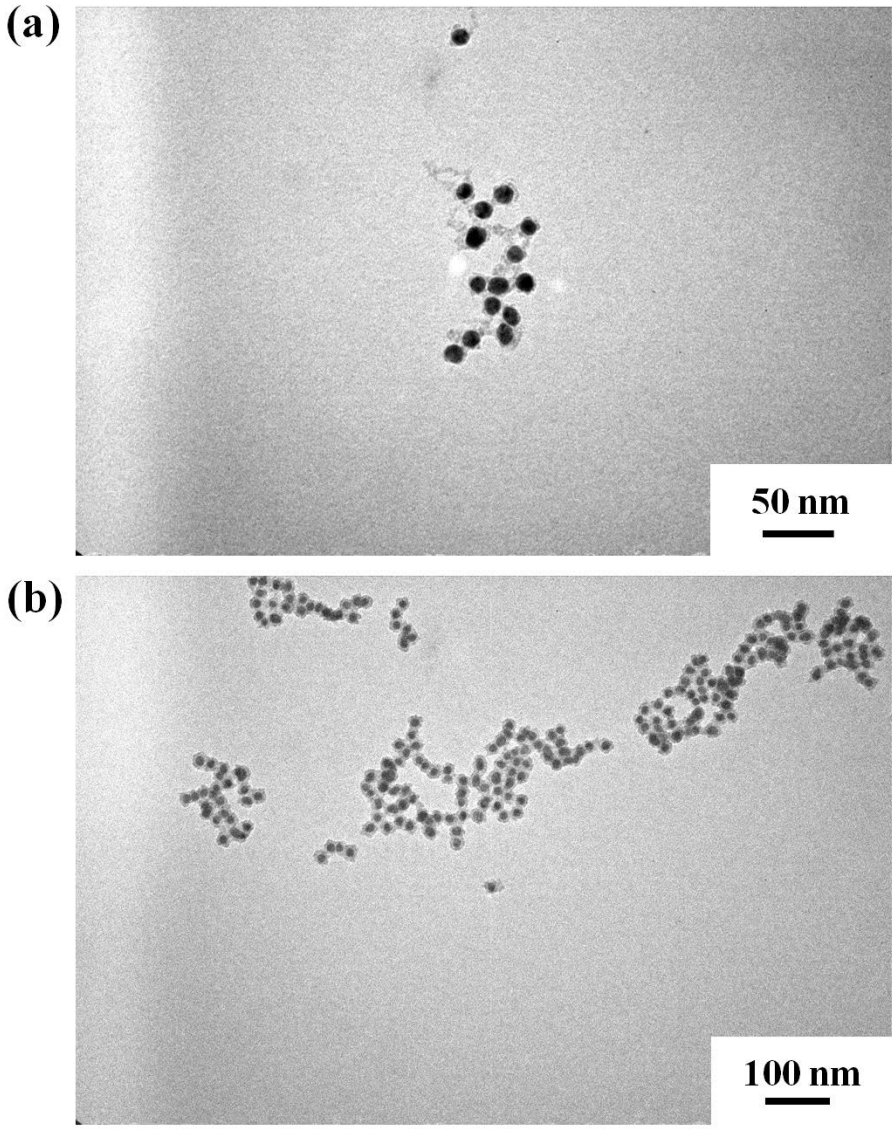

Figure 5.4 TEM images of (a) oligomeric-PEO capped Au/CdS CSNCs with core diameter=13 ± 0.9 nm and shell thickness=1.5 ±0.4 nm and (b) oligomeric-PEO capped Au/CdS CSNCs with core diameter= 13 ± 0.9 nm and shell thickness= 4 ±0.6 nm.

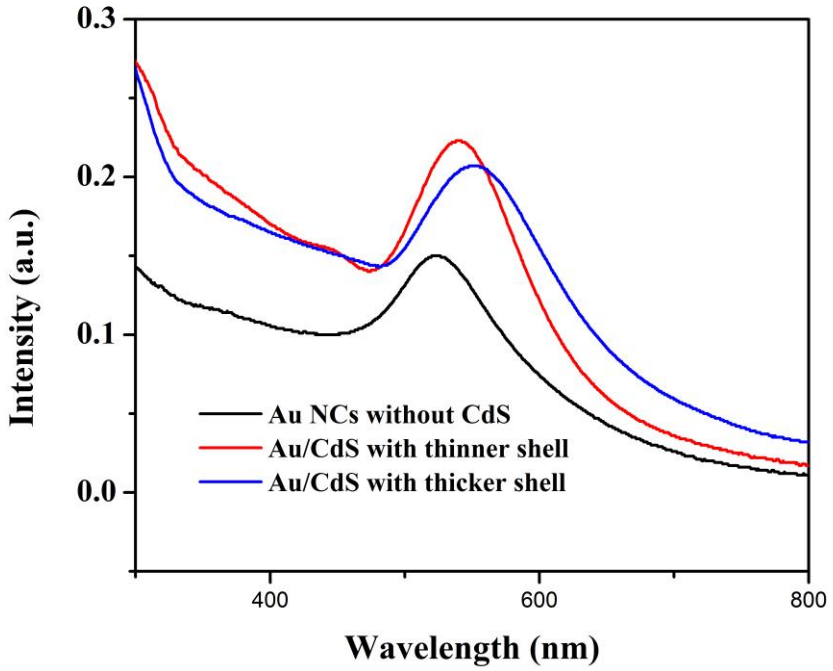

Figure 5.5 UV-Vis spectra of absorption peaks of (a) Au core NCs and (b) oligomeric-PEO capped Au/CdS CSNCs.

One interesting phenomenon after the growth of semiconducting CdS shell is that the LSPR peak is shifted to the longer wavelength and the increasing the thickness of CdS shell causes the further red-shift in the LSPR peak of Au NCs. It is well-established that the LSPR position peak of the Au NCs is dependent upon the surrounding medium. Surface coating dielectric tends to cause the shift of LSPR peak and red-shift in the LSPR absorption peak is due to the coating of materials possessing high refractive index. [144] The similar tendency has been reported in silica-coated Au CSNCs colloidal solution. [145-148]

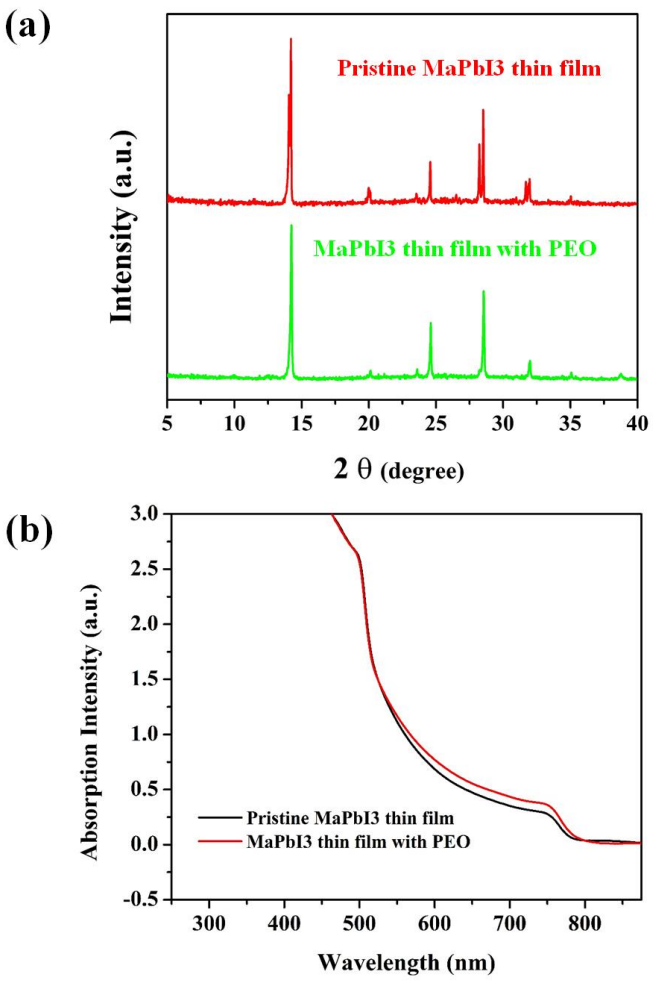

Figure 5.6 Highly chemical compatibility of PEO with $MAPbI_3$ organic-inorganic hybrid perovskite (a) XRD patterns of $MAPbI_3$ perovskite thin film with and without the presence of PEO and (b) UV-Vis absorption spectra of $MAPbI_3$ perovskite thin film with and without the presence of PEO.

One advantage of preparing oligomeric PEO-capped Au/CdS CSNCs is that the surface capped short ligands (i.e., oligomeric PEO) not only enable the superior solubility in polar or non-polar solvents (e.g., cyclohexane, toluene and even water), thereby leading to excellent processability but also confer good chemical compatibility with organolead halide perovskite to CSNCs, which provides possibility of practical application in

optoelectronic devices. Figure 5.6a shows the XRD patterns of organolead iodide perovskite prior to and after the mixing with PEO linear polymer. XRD patterns clearly indicate that there is no appearance of new phase or decomposition of perovskite material. UV-Vis spectra further indicate that mixing PEO with perovskite will not cause any negative effect on structural integrity of perovskite because the thin film consisting of $MAPbI_3$ and PEO linear polymer still displays characteristic absorption peak similar to pristine perovskite.

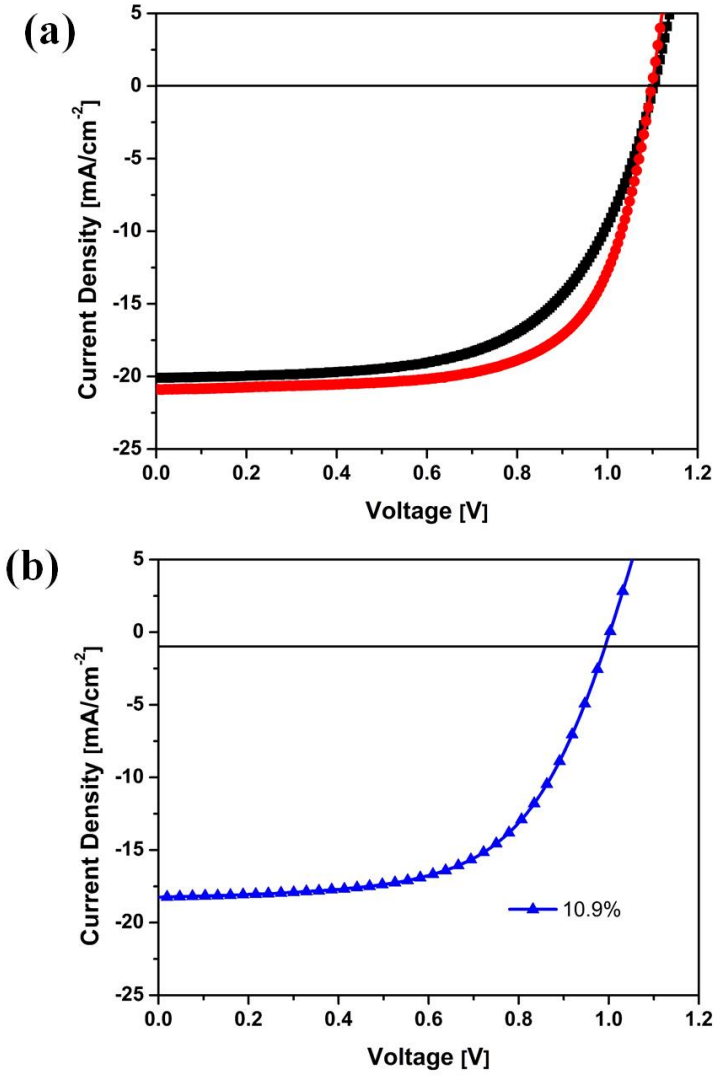

Figure 5.7 Power conversion efficiency of (a) $MAPbI_3$ perovskite solar cell with and without incorporation of oligomeric-PEO capped Au/CdS CSNCs with core diameter= 13 ± 0.9 nm and shell thickness= 4 ±0.6 nm prepared from triblock copolymers as nanoreactors and (b) $MAPbI_3$ perovskite solar cell with incorporation of PEO (Mw=5000) capped Au/CdS CSNCs with core diameter= 13 ± 0.9 nm and shell thickness= 4 ±0.6 nm.

As synthesized oligomeric PEO-capped Au/CdS CSNCs was incorporated into the $MAPbI_3$ based perovskite solar cells without futher treatment **(Figure 5.7**). It was found that incorporation oligomeric PEO-capped Au/CdS CSNCs led to the increase in the power conversion efficiency (15.5%) in comparison to perovskite solar cell without Au/CdS CSNCs (13.5%). The possible reason for this increase in performance is attributed to the difference in the band structure of semiconducting CdS and metallic Au core NCs, leading to the fact that there is a pronounced photoinduced charge separation located at the bounday of Au core and CdS shell, resulting in the hole-charged Au core and the eletron-enriched CdS shell. An experiment with incorporation of PEO-capped Au/CdS CSNCs (molecular weight=5000) into perovskite solar cell was also conducted, displaying decrease in power conversion efficiency (10.9%). This decrease in efficiency is due to the long PEO capping on the CSNCs surface, which blocks the efficient electron transportation.

5.4 Summary

In conclusions, we developed a facile and robust ***non-epitaxial*** growth approach for preparing metal/semiconducting CSNCs with excellent core size and shell thickness control and length-tunable polymer ligands. The surface capped oligomeric PEO not only enabled the good solubility in various organic solvents, thereby giving rise to good solution processability, but also exhibited excellent chemical compatibility with organolead halide

perovskite. We envision that this triblock copolymer nanoreactors strategy can be readily extended to produce other core/shell structures with large lattice mismatch.

CHAPTER 6. GENERAL CONCUSIONS AND BROADER IMPACT

6.1 General Conclusions

Tremendous advancement of reversible-deactivation radical polymerization or living radical polymerization (e.g., ATRP, RAFT and NMP) enables preparation of macromolecules with pre-determined molecular weight, very narrow size distribution (i.e., low polydispersity), well-defined shape and complex architectures (e.g., star-like, bottle brush-like, necklace-like and hyper-branch). In this dissertation, we successfully demonstrated that nanostructured materials with fascinating properties (e.g., semiconducting, light emissive and plasmonic properties), diverse morphologies (e.g., hollow and core/shell nanocrystals) can be synthesized via an unconventional synthetic strategies based on utilizing a series of well-defined star-like triblock copolymers as nanoreactors. This nanoreactors synthetic approach circumvented several inherent limitations of traditional routes, thereby crafting diverse functional nanocrystals which were inaccessible to conventional routes.

In the first part of this dissertation, semiconducting narrow band gap hollow lead chalcogenides NCs (e.g., lead telluride and lead sulfide), which cannot be prepared by conventional hollow nanocrystals synthetic routes (e.g., Kirkendall method, galvanic replacement method, chemical etching route and template-assisted approach), was crafted via utilizing well-defined star-like polystyrene-*block*-poly(*tert*-butyl acrylate)-*block*-polystyrene (i.e., coil-*b*-coil-*b*-coil) and polystyrene-*block*-poly acrylic acid-*block*-poly(3,4-ethylenedioxythiophene) (i.e., coil-*b*-coil-*b*-rod) as nanoreactors. Our synthetic strategy also offered an robust, environmental-friendly, one-pot approach for substituting insulating polymer ligands with semiconducting conjugated polymer ligands with 100%

efficiency, which offered an alternative to classic molecular metal chalcogenides complex method involving usage of highly toxic and explosive hydrazine. Because of the successful preparation of uniform narrow band gap semiconducting hollow nanocrystals, for the first time, we experimentally verified the enlargement of optical band gap of hollow semiconducting nanocrystals with near-IR absorption in comparison to semiconducting solid counterparts.

In the second part of this dissertation, polymer ligands-capped silica-coated organic-inorganic hybrid perovskite nanocrystals, with improved size uniformity in comparison to conventionally prepared perovskite nanocrystals, were crafted via using a series judiciously designed poly(4-vinylpyridine)-*block*-poly(*tert*-butyl acrylate)-*block*-polyethylene oxide and poly(4-vinylpyridine)-*block*-poly(*tert*-butyl acrylate)-*block*-polystyrene, prepared from ATRP and click reaction, as nanoreactors. This strategy offered not only a facile alternative to the currently used ligand assisted reprecipitation method with improved size uniformity and morphology control but also proposed a powerful approach for achieving tunable surface chemistry by tuning hydrophilic ligands to hydrophobic ligands without causing any damage to the structural integrity. The resulting polymer ligands-capped silica-coated organic-inorganic hybrid perovskite nanocrystals exhibited markedly improved colloidal stability, chemical composition stability, photostability and moisture stability compared with other stable perovskite nanocrystals.

In the third part of this dissertation, metal/semiconducting core/shell nanocrystals with large lattice mismatch were crafted via using novel star-like poly(4-vinylpyridine)-*block*-poly(*tert*-butyl acrylate)-*block*-oligomeric polyethylene oxide as nanoreactors. This synthetic strategy provided an essential ***nonepitaxial*** approach for controlled preparing gold/cadmium sulfide core/shell nanocrystals with precise dimension control and tunable length of ligands capped on nanocrystals. The optical property of core/shell nanocrystals can be readily tuned by varying the semiconducting shell thickness. The short-length

oligomeric PEO ligands situated on the surface of core/shell nanocrystals not only enabled the superior processability and colloidal stability, but also efficient nanocrystal-to-nanocrystal contact. Then, the power conversion efficiency of perovskite solar cells were enhanced by incorporation of as-synthesized core/shell nanocrystals without any post-treatment owing to the photoinduced charge separation taken place at the interface of metal and semiconducting materials.

6.2 Broader Impact

The findings presented in this dissertation may provide fundamental insights or practical synthetic strategies for rational design of organic-inorganic nanohybrids consisting of well-designed nanostructured materials as nano-fillers and diverse polymers as matrix, leading to the potential application in energy conversion and harvesting.

In the first part of this dissertation, semiconducting poly (3,4-ethylenedioxythiophene) capped hollow lead chalcogenides nanocrystals exhibit great application in thermoelectric devices, which convert heat into electricity. In principle, to achieve high performance, it requires high Seebeck coefficient, high electrical conductivity and low thermal conductivity. [149, 150] However, the quantities of these three parameters for conventional 3-dimension crystalline materials are often interrelated in such a way that it is very difficult to tune one variable independently without adversely affecting the other two. As a result, it is quite difficult to realize this situation in traditional bulk materials. However as the dimension of materials decreases and approaches nanometer length scales, it is possible to vary these three parameters quasi-independently. Organic-inorganic thermoelectric nanocomposites consisting of hollow lead chalcogenide nanocrystals and semiconducting poly(3,4-ethylenedioxythiophene) may

exhibit enhanced thermoelectric performance owing to the low thermoelectric conductivity originated from conjugated polymer matrix and high electrical conductivity and Seeback coefficient imparted by inorganic nanocrystals. Furthermore, the intimately and permanently tethered conjugated polymer onto surface of inorganic nanocrystals achieves a good interface, thereby improving the phonon scattering while facilitating the electron transportation.

In addition, a few theoretical studies on nanoporous materials indicate appreciable reduction in thermal conductivity while slight decrease in electrical conductivity owing to the presence of hollow structures. [151] And the thermal conductivity of material can be further reduced via decreasing the size of porous comparable to the mean free path of phonon even though the porosity is fixed. [152] Although this equation sheds light on the reduction of thermal conductivity in nanoporous material, a more comprehensive and realistic model should be considered, especially considering that thermal conductivity approaches zero when the size of nanopores becomes extremely small compared to the length of mean free path of phonons. Therefore, the hollow interior presented in hollow lead chalcogenide nanocrystals may be beneficial for the further decrease in thermal conductivity via scattering the transportation of electron (i.e., increasing performance of thermoelectric devices). We believe that judiciously designed thermoelectric hybrids consisting of tunable molecular weight of conducting polymer matrix and dimension of semiconducting inorganic nanocrystals with hollow interior will facilitate the fundamental understanding of interrelationship among electrical conductivity, thermal conductivity and Seebeck coefficient in thermoelectric nanocomposites.

In the second part of this dissertation, as-synthesized polystyrene-capped silica-coated methylammonium lead bromide nanocrystals displays remarkable stability enhancement,

which is a promising candidate for light emitting diodes application. Light emitting diodes devices can be divided into two categories based on the lighting mechanism. In photoluminescence, the luminescence is generated from the radiative recombination of photo-excited carriers (i.e., electrons and holes) by exposure to a sufficient intense light source. In electroluminescence, the process of luminescence generation is very similar to that of photoluminescence except that radiative recombination of carriers is excited by current injection. In comparison to electroluminescence, photoluminescence is pretty simple in a sense that the photoluminescence is largely dependent upon the optical property of active material as opposed to be several factors, including physical structure of the optically active layers and the electrical properties of cathode and anode contacts. We believe that polymer-capped silica-coated organic-inorganic hybrid perovskite nanocrystals will display potential applications in photoluminescence via mixing with certain phosphors owing to excellent stability, high quantum yield and narrow emission band width.

In the third part of this dissertation, nanoreactors strategy based on triblock copolymers offers not only novel way to fabricate core/shell structure with large lattice mismatch but also exhibits potential application in photocatalytic reaction under visible light illumination. Short-chain oligomeric polyethylene oxide capped gold/cadmium sulfide core/shell nanocrystals can be utilized as an effective photocatalyst in visible light water splitting. Nano-hybrids consisting of two dissimilar materials possess pronounced advantage over single-component systems owing to the extended light absorption capability and improved catalytic properties generated from the synergistic effect. [153] In the case of metal/semiconducting, gold nanocrystals serve as sensitizer enabling the visible light utilization by cadmium sulfide wide band gap semiconductors. This judiciously design may be beneficial for photocatalytic reaction in water splitting.

DESIMINATION OF THE WORK

The work presented in this dissertation has been conveyed to the scientific community by the following publications and presentations.

Publication

1. **Y. He**, X. Pang, B. Jiang, C. Feng, Y.W. Harn, Y. Chen, Y.J. Yoon, S. Pan, C.H. Lu, Y.J. Chang, M. Zebarjadi, Z. Kang, N. Thadhani, J. Peng, Z. Lin, ***Angewandte Chemie International Edition,*** **(selected as very important paper and inside back cover), 56,** 12946 (2017)

2. X. Pang, **Y. He**, J. Jaehan and Z. Lin, ***Science***, **323,** 1268 (2016)**.**

3. **Y. He**. X. Pang and Z. Lin, in preparation.

4. Y. Chen, D. Yang, Y. Yoon, X. Pang, Z. Wang, J. Jung, **Y. He**, Y. Harn, M. He, S. Zhang, G. Zhang and Z. Lin, ***Journal of American Chemical Society***, 139, 12956 (2017)

5. X. Cui, P. Xiao, J. Wang, M. Zhou, W. Guo, Y. Yang, **Y. He**, Z. Wang, Y. Yang, Y. Zhang and Z. Lin, ***Angewandte Chemie International Edition,*** **129,** 4559 (2017)

6. B. Jiang, **Y. He**, B. Li, S. Zhao, S. Wang, Y.B. He and Z. Lin, ***Angewandte Chemie International Edition,*****56,** 1869 (2017)

7. S. Zhao, Z. Wang, **Y. He**, B. Jiang, Y. Harn, X. Liu, F. Yu, F. Feng, Q. Shen and Z. Lin, ***ACS Energy Letters,*** **2**, 111 (2016)

8. Y. Chen, Y. Yoon, X. Pang, **Y. He**, J. Jung, C. Feng, G. Zhang and Z. Lin, ***Small,*** **12**, 6714 (2016)

9. M. He, B. Li, X. Cui, B. Jiang, **Y. He**, Y. Chen, D. O'neil, P. Szymanski, M.A. EI-Sayed, J. Huang and Z. Lin, ***Nature Communication,*** **8,** 2017

10. M. He, X. Pang, X. Liu, B. Jiang, **Y. He**, H. Snaith and Z. Lin, ***Angewandte Chemie International Edition.*** **128,** 4352 (2016)

11. B. Jiang, C. Han, B. Li, **Y. He** and Z. Lin, ***ACS Nano***. 10, 2728 (2016)

12. M. Wang, X. Pang, D. Zheng, **Y. He**, L. Sun, C. Lin and Z. Lin, ***Journal of Materials Chemistry A***. **4**, 7190 (2016)

13. D. Yang, X. Pang, **Y. He**, Y. Wang, G. Chen, W. Wang, and Z. Lin, ***Angewandte Chemie International Edition.* 127,** 12259 (2015)

14. D. Zheng, X. Pang, M. Wang, **Y. He**, C. Lin, and Z. Lin, ***Chemistry of Materials***. **27**, 5271 (2015)

15. C. Feng, X. Pang, **Y. He**, Y. Chen, G. Zhang, Z. Lin, ***Polymer Chemisty***, 6, 5190 (2015)

16. H. Tang, **Y. He**, B. Li, J. Jung and Z. Lin, ***Nanoscale***, DOI: 10.1039/C5NR01492A

17. C. Han, D. Yang, Y. Yang, B. Jiang, **Y. He**, M. Wang, A. Song, Y. He, B. Li, and Z. Lin, ***Journal of Materials Chemistry A***. **3**, 13340 (2015)

18. X. Hui, X. Pang, **Y. He**, M. He, J. Jung, H. Xia and Z. Lin, ***Angewandte Chemie International Edition,* 127**, 4719 (2015).

19. X. Hui, Y. Xu, X. Pang, **Y. He**, J. Jung, H. Xia and Z. Lin, ***Science Advances***, 1, e1500025 (2015).

20. C. Feng, X. Pang, **Y. He**, B. Li, and Z. Lin, ***Chemistry of Materials***, **26**, 6058 (2014).

21. 21. X. Pang, **Y. He**, B. Jiang, J. Iocozzia, L. Zhao, H. Guo, J. Liu, M. Akinc, N. Bowler, X. Tan, Z. Lin, ***Nanoscale***, **5**, 8695 (2013).

Presentation

1. **Y. He** and Z. Lin, "Improvement of stability of methylammonium lead halide nanocrystals via precise molecular design of star-like triblock copolymers", **Oral presentation**, Materials Research Society, Phoenix, AZ, April 21, 2017.

2. **Y. He** and Z. Lin, **"**Robust strategy for crafting for crafting metal telluride hollow nanocrystals using star-like triblock copolymers as nanoreactors", **Oral presentation**, American Chemical Society, Division of polymeric materials and science, San Diego, CA, March 16, 2016.

REFERENCES

1. Matyjaszewski, K. Atom Transfer Radical Polymerization (ATRP): Current Status and Future Perspectives. *Macromolecules* **45**, 4015-4039 (2012).

2. Nicolas, J. et al. Nitroxide-mediated polymerization. *Prog Polym Sci* **38**, 63-235 (2013).

3. O'Donnell, J.M. Reversible addition-fragmentation chain transfer polymerization in microemulsion. *Chem Soc Rev* **41**, 3061-3076 (2012).

4. Matyjaszewski, K. & Xia, J.H. Atom transfer radical polymerization. *Chem Rev* **101**, 2921-2990 (2001).

5. Dadashi-Silab, S., Tasdelen, M.A. & Yagci, Y. Photoinitiated Atom Transfer Radical Polymerization: Current Status and Future Perspectives. *J Polym Sci Pol Chem* **52**, 2878-2888 (2014).

6. Wang, J.S. & Matyjaszewski, K. Controlled Living Radical Polymerization - Atom-Transfer Radical Polymerization in the Presence of Transition-Metal Complexes. *J Am Chem Soc* **117**, 5614-5615 (1995).

7. Wang, J.S. & Matyjaszewski, K. Controlled Living Radical Polymerization - Halogen Atom-Transfer Radical Polymerization Promoted by a Cu(I)Cu(Ii) Redox Process. *Macromolecules* **28**, 7901-7910 (1995).

8. Patten, T.E., Xia, J.H., Abernathy, T. & Matyjaszewski, K. Polymers with very low polydispersities from atom transfer radical polymerization. *Science* **272**, 866-868 (1996).

9. Chauvin, F. et al. Nitroxide-mediated polymerization: The pivotal role of the k(d) value of the initiating alkoxyamine and the importance of the experimental conditions. *Macromolecules* **39**, 5238-5250 (2006).

10. Iddon, P.D., Robinson, K.L. & Armes, S.P. Polymerization of sodium 4-styrenesulfonate via atom transfer radical polymerization in protic media. *Polymer* **45**, 759-768 (2004).

11. Yang, L. et al. Zwitterionic Poly (Cysteine Methacrylate) Functional Polysulfone Via ATRP and Their Anti-protein Fouling Property. *Text Bioeng Inform S*, 70-74 (2017).

12. Wu, J., Zhang, B.J., Zhang, L.F., Cheng, Z.P. & Zhu, X.L. Photoinduced Iron-Based Water-Induced Phase Separable Catalysis (WPSC) ICAR ATRP of Poly(ethylene glycol) Methyl Ether Methacrylate. *Macromol Rapid Comm* **38** (2017).

13. Wu, Y.W. et al. Synthesis and characterization of carbon fibers functionalized with poly (glycidyl methacrylate) via atom transfer radical polymerization. *Iop Conf Ser-Mat Sci* **87** (2015).

14. Qian, X.L., Fan, H., Wang, C.Z. & Wei, Y.M. Preparation of high-capacity, weak anion-exchange membranes by surface-initiated atom transfer radical polymerization of poly(glycidyl methacrylate) and subsequent derivatization with diethylamine. *Appl Surf Sci* **271**, 240-247 (2013).

15. Robinson, K.L., Khan, M.A., Banez, M.V.D., Wang, X.S. & Armes, S.P. Controlled polymerization of 2-hydroxyethyl methacrylate by ATRP at ambient temperature. *Macromolecules* **34**, 3155-3158 (2001).

16. Coca, S., Jasieczek, C.B., Beers, K.L. & Matyjaszewski, K. Polymerization of acrylates by atom transfer radical polymerization. Homopolymerization of 2-hydroxyethyl acrylate. *J Polym Sci Pol Chem* **36**, 1417-1424 (1998).

17. Wang, F., Wan, L.S. & Xu, Z.K. Graft polymerization of 2-hydroxyethyl methacrylate via ATRP with poly(acrylonitrile-co-p-chloromethyl styrene) as a macroinitiator. *Sci China Chem* **55**, 1125-1133 (2012).

18. Huang, Z.C., Chen, J., Zhang, L.F., Cheng, Z.P. & Zhu, X.L. ICAR ATRP of Acrylonitrile under Ambient and High Pressure. *Polymers-Basel* **8** (2016).

19. Liang, E.X. et al. Photoinduced ATRP of acrylonitrile with aniline as photoinitiator. *J Macromol Sci A* **53**, 210-214 (2016).

20. Wang, Y., He, N.P. & Lu, Z.W. Synthesis of End-functional and Mid-functional Temperature-responsive Poly(N,N-diethyl-acrylamide) by ATRP. *Acta Polym Sin*, 464-470 (2017).

21. Liu, K., Cao, Y.F., Li, Y., Liu, Z.L. & Tan, F.Z. R-ATRP of acrylamide under the action of copper complex system in aqueous two-phase. *Adv Mater Res-Switz* **652-654**, 430-434 (2013).

22. Ma, Y.H. et al. Immobilization of poly(acrylamide) brushes onto poly(caprolactone) surface by combining ATRP and "click" chemistry: Synthesis, characterization and evaluation of protein adhesion. *Appl Surf Sci* **329**, 223-233 (2015).

23. Xia, J.H., Zhang, X. & Matyjaszewski, K. Atom transfer radical polymerization of 4-vinylpyridine. *Macromolecules* **32**, 3531-3533 (1999).

24. Tang, W. & Matyjaszewski, K. Effect of ligand structure on activation rate constants in ATRP. *Macromolecules* **39**, 4953-4959 (2006).

25. Keating, J.J., Lee, A. & Belfort, G. Predictive Tool for Design and Analysis of ARGET ATRP Grafting Reactions. *Macromolecules* **50**, 7930-7939 (2017).

26. Fierens, S.K., Van Steenberge, P.H.M., Reyniers, M.F., Marin, G.B. & D'hooge, D.R. How Penultimate Monomer Unit Effects and Initiator Influence ICAR ATRP of n-Butyl Acrylate and Methyl Methacrylate. *Aiche J* **63**, 4971-4986 (2017).

27. Wu, J.Y. et al. A effective approach for surface modification of polymer membrane via SI-eATRP in an electrochemical cell with a three electrode system. *Surf Interfaces* **8**, 119-126 (2017).

28. Augustine, K.F. et al. Activation of Alkyl Halides at the Cu-0 Surface in SARA ATRP: An Assessment of Reaction Order and Surface Mechanisms. *J Polym Sci Pol Chem* **55**, 3048-3057 (2017).

29. Treat, N.J. et al. Metal-Free Atom Transfer Radical Polymerization. *J Am Chem Soc* **136**, 16096-16101 (2014).

30. Miyake, G.M. & Theriot, J.C. Perylene as an Organic Photocatalyst for the Radical Polymerization of Functionalized Vinyl Monomers through Oxidative Quenching with Alkyl Bromides and Visible Light. *Macromolecules* **47**, 8255-8261 (2014).

31. Gawande, M.B. et al. Core-shell nanoparticles: synthesis and applications in catalysis and electrocatalysis. *Chem Soc Rev* **44**, 7540-7590 (2015).

32. Turkevich, J., Stevenson, P.C. & Hillier, J. A Study of the Nucleation and Growth Processes in the Synthesis of Colloidal Gold. *Discuss Faraday Soc*, 55-& (1951).

33. Piella, J., Bastus, N.G. & Puntes, V. Size-Controlled Synthesis of Sub-10-nanometer Citrate-Stabilized Gold Nanoparticles and Related Optical Properties. *Chem Mater* **28**, 1066-1075 (2016).

34. Wang, X., Zhuang, J., Peng, Q. & Li, Y.D. A general strategy for nanocrystal synthesis. *Nature* **437**, 121-124 (2005).

35. Park, J. et al. Ultra-large-scale syntheses of monodisperse nanocrystals. *Nat Mater* **3**, 891-895 (2004).

36. Si, R., Zhang, Y.W., Zhou, H.P., Sun, L.D. & Yan, C.H. Controlled-synthesis, self-assembly behavior, and surface-dependent optical properties of high-quality rare-earth oxide nanocrystals. *Chem Mater* **19**, 18-27 (2007).

37. Chen, J. et al. Collective Dipolar Interactions in Self-Assembled Magnetic Binary Nanocrystal Superlattice Membranes. *Nano Lett* **10**, 5103-5108 (2010).

38. Murray, C.B., Norris, D.J. & Bawendi, M.G. Synthesis and Characterization of Nearly Monodisperse Cde (E = S, Se, Te) Semiconductor Nanocrystallites. *J Am Chem Soc* **115**, 8706-8715 (1993).

39. Kershaw, S.V., Susha, A.S. & Rogach, A.L. Narrow bandgap colloidal metal chalcogenide quantum dots: synthetic methods, heterostructures, assemblies, electronic and infrared optical properties. *Chem Soc Rev* **42**, 3033-3087 (2013).

40. Pietryga, J.M. et al. Pushing the band gap envelope: Mid-infrared emitting colloidal PbSe quantum dots. *J Am Chem Soc* **126**, 11752-11753 (2004).

41. Hines, M.A. & Scholes, G.D. Colloidal PbS nanocrystals with size-tunable near-infrared emission: Observation of post-synthesis self-narrowing of the particle size distribution. *Adv Mater* **15**, 1844-1849 (2003).

42. Kruger, S., Hickey, S.G., Tscharntke, S. & Eychmuller, A. Study of the Attachment of Linker Molecules and Their Effects on the Charge Carrier Transfer at Lead Sulfide Nanoparticle Sensitized ZnO Substrates. *J Phys Chem C* **115**, 13047-13055 (2011).

43. Li, H.B. et al. Size- and shape-controlled synthesis of PbSe and PbS nanocrystals via a facile method. *Crystengcomm* **12**, 1127-1133 (2010).

44. Berhanu, D. et al. A novel soft hydrothermal (SHY) route to crystalline PbS and CdS nanoparticles exhibiting diverse morphologies. *Chem Commun*, 4709-4711 (2006).

45. Cademartiri, L. et al. Size-dependent extinction coefficients of PbS quantum dots. *J Am Chem Soc* **128**, 10337-10346 (2006).

46. Bakueva, L. et al. PbS quantum dots with stable efficient luminescence in the near-IR spectral range. *Adv Mater* **16**, 926-929 (2004).

47. Mokari, T.L., Zhang, M.J. & Yang, P.D. Shape, size, and assembly control of PbTe nanocrystals. *J Am Chem Soc* **129**, 9864-+ (2007).

48. Urban, J.J., Talapin, D.V., Shevchenko, E.V. & Murray, C.B. Self-assembly of PbTe quantum dots into nanocrystal superlattices and glassy films. *J Am Chem Soc* **128**, 3248-3255 (2006).

49. Murphy, J.E. et al. PbTe colloidal nanocrystals: Synthesis, characterization, and multiple exciton generation. *J Am Chem Soc* **128**, 3241-3247 (2006).

50. Lu, W.G., Fang, J.Y., Stokes, K.L. & Lin, J. Shape evolution and self assembly of monodisperse PbTe nanocrystals. *J Am Chem Soc* **126**, 11798-11799 (2004).

51. Liu, M.Z., Johnston, M.B. & Snaith, H.J. Efficient planar heterojunction perovskite solar cells by vapour deposition. *Nature* **501**, 395-+ (2013).

52. Wang, N.N. et al. Perovskite light-emitting diodes based on solution-processed self-organized multiple quantum wells. *Nat Photonics* **10**, 699-+ (2016).

53. Zhang, L.Q. et al. Ultra-bright and highly efficient inorganic based perovskite light-emitting diodes. *Nat Commun* **8** (2017).

54. Huang, H., Bodnarchuk, M.I., Kershaw, S.V., Kovalenko, M.V. & Rogach, A.L. Lead Halide Perovskite Nanocrystals in the Research Spotlight: Stability and Defect Tolerance. *Acs Energy Lett* **2**, 2071-2083 (2017).

55. Schmidt, L.C. et al. Nontemplate Synthesis of CH3NH3PbBr3 Perovskite Nanoparticles. *J Am Chem Soc* **136**, 850-853 (2014).

56. Zhang, F. et al. Brightly Luminescent and Color-Tunable Colloidal CH3NH3PbX3 (X = Br, I, Cl) Quantum Dots: Potential Alternatives for Display Technology. *Acs Nano* **9**, 4533-4542 (2015).

57. Zhang, F. et al. Colloidal Synthesis of Air-Stable CH3NH3PbI3 Quantum Dots by Gaining Chemical Insight into the Solvent Effects. *Chem Mater* **29**, 3793-3799 (2017).

58. Protesescu, L. et al. Nanocrystals of Cesium Lead Halide Perovskites (CsPbX3, X = Cl, Br, and I): Novel Optoelectronic Materials Showing Bright Emission with Wide Color Gamut. *Nano Lett* **15**, 3692-3696 (2015).

59. Akkerman, Q.A. et al. Tuning the Optical Properties of Cesium Lead Halide Perovskite Nanocrystals by Anion Exchange Reactions. *J Am Chem Soc* **137**, 10276-10281 (2015).

60. Koscher, B.A., Swabeck, J.K., Bronstein, N.D. & Alivisatos, A.P. Essentially Trap-Free CsPbBr3 Colloidal Nanocrystals by Postsynthetic Thiocyanate Surface Treatment. *J Am Chem Soc* **139**, 6566-6569 (2017).

61. Swarnkar, A. et al. Quantum dot-induced phase stabilization of alpha-CsPbI3 perovskite for high-efficiency photovoltaics. *Science* **354**, 92-95 (2016).

62. Liu, F. et al. Highly Luminescent Phase-Stable CsPbI(3) Perovskite Quantum Dots Achieving Near 100% Absolute Photoluminescence Quantum Yield. *Acs Nano* **11**, 10373-10383 (2017).

63. Liu, F. et al. Colloidal Synthesis of Air-Stable Alloyed CsSn1-xPbxI3 Perovskite Nanocrystals for Use in Solar Cells. *J Am Chem Soc* **139**, 16708-16719 (2017).

64. Zhang, P. & Gao, L. Synthesis and characterization of CdS nanorods via hydrothermal microemulsion. *Langmuir* **19**, 208-210 (2003).

65. Carbone, L. et al. Synthesis and micrometer-scale assembly of colloidal CdSe/CdS nanorods prepared by a seeded growth approach. *Nano Lett* **7**, 2942-2950 (2007).

66. Li, Y.X., Hu, Y.F., Peng, S.Q., Lu, G.X. & Li, S.B. Synthesis of CdS Nanorods by an Ethylenediamine Assisted Hydrothermal Method for Photocatalytic Hydrogen Evolution. *J Phys Chem C* **113**, 9352-9358 (2009).

67. Bekenstein, Y., Koscher, B.A., Eaton, S.W., Yang, P.D. & Alivisatos, A.P. Highly Luminescent Colloidal Nanoplates of Perovskite Cesium Lead Halide and Their Oriented Assemblies. *J Am Chem Soc* **137**, 16008-16011 (2015).

68. Akkerman, Q.A. et al. Solution Synthesis Approach to Colloidal Cesium Lead Halide Perovskite Nanoplatelets with Monolayer-Level Thickness Control. *J Am Chem Soc* **138**, 1010-1016 (2016).

69. Zhang, D.D. et al. Ultrathin Colloidal Cesium Lead Halide Perovskite Nanowires. *J Am Chem Soc* **138**, 13155-13158 (2016).

70. Zhang, D.D., Eaton, S.W., Yu, Y., Dou, L.T. & Yang, P.D. Solution-Phase Synthesis of Cesium Lead Halide Perovskite Nanowires. *J Am Chem Soc* **137**, 9230-9233 (2015).

71. Balakrishnan, S.K. & Kamat, P.V. Au-CsPbBr3 Hybrid Architecture: Anchoring Gold Nanoparticles on Cubic Perovskite Nanocrystals. *Acs Energy Lett* **2**, 88-93 (2017).

72. Liu, W.Y. et al. Mn2+-Doped Lead Halide Perovskite Nanocrystals with Dual-Color Emission Controlled by Halide Content. *J Am Chem Soc* **138**, 14954-14961 (2016).

73. Akkerman, Q.A., Meggiolaro, D., Dang, Z.Y., De Angelis, F. & Manna, L. Fluorescent Alloy CsPbxMn1-x,I-3 Perovskite Nanocrystals with High Structural and Optica Stability. *Acs Energy Lett* **2**, 2183-2186 (2017).

74. Arunkumar, P. et al. Colloidal Organolead Halide Perovskite with a High Mn Solubility Limit: A Step Toward Pb-Free Luminescent Quantum Dots. *J Phys Chem Lett* **8**, 4161-4166 (2017).

75. Begum, R. et al. Engineering Interfacial Charge Transfer in CsPbBr3 Perovskite Nanocrystals by Heterovalent Doping. *J Am Chem Soc* **139**, 731-737 (2017).

76. Mattoni, A., Filippetti, A., Saba, M.I. & Delugas, P. Methylammonium Rotational Dynamics in Lead Halide Perovskite by Classical Molecular Dynamics: The Role of Temperature. *J Phys Chem C* **119**, 17421-17428 (2015).

77. Mosconi, E., Quarti, C., Ivanovska, T., Ruani, G. & De Angelis, F. Structural and electronic properties of organo-halide lead perovskites: a combined IR-spectroscopy and ab initio molecular dynamics investigation. *Phys Chem Chem Phys* **16**, 16137-16144 (2014).

78. Park, B.W. et al. Resonance Raman and Excitation Energy Dependent Charge Transfer Mechanism in Halide-Substituted Hybrid Perovskite Solar Cells. *Acs Nano* **9**, 2088-2101 (2015).

79. Berhe, T.A. et al. Organometal halide perovskite solar cells: degradation and stability. *Energ Environ Sci* **9**, 323-356 (2016).

80. Sun, C. et al. Efficient and Stable White LEDs with Silica-Coated Inorganic Perovskite Quantum Dots. *Adv Mater* **28**, 10088-10094 (2016).

81. Huang, H. et al. Water resistant CsPbX3 nanocrystals coated with polyhedral oligomeric silsesquioxane and their use as solid state luminophores in all-perovskite white light-emitting devices. *Chem Sci* **7**, 5699-5703 (2016).

82. Parobek, D., Dong, Y., Qiao, T., Rossi, D. & Son, D.H. Photoinduced Anion Exchange in Cesium Lead Halide Perovskite Nanocrystals. *J Am Chem Soc* **139**, 4358-4361 (2017).

83. Koposova, E. et al. Oleylamine-Stabilized Gold Nanostructures for Bioelectronic Assembly. Direct Electrochemistry of Cytochrome c. *J Phys Chem C* **117**, 13944-13951 (2013).

84. Zhou, S. et al. Facile Synthesis of Silver Nanocubes with Sharp Corners and Edges in an Aqueous Solution. *Acs Nano* **10**, 9861-9870 (2016).

85. Frank, A.J., Cathcart, N., Maly, K.E. & Kitaev, V. Synthesis of Silver Nanoprisms with Variable Size and Investigation of Their Optical Properties: A First-Year Undergraduate Experiment Exploring Plasmonic Nanoparticles (vol 87, pg 1098, 2010). *J Chem Educ* **89**, 1087-1087 (2012).

86. Samim, M., Prashant, C.K., Dinda, A.K., Maitra, A.N. & Arora, I. Synthesis and characterization of gold nanorods and their application for photothermal cell damage. *Int J Nanomed* **6**, 1825-1831 (2011).

87. Kim, S.M., Lee, D.G. & Lee, I.S. Selective and differential functionalization of interior surface of hollow nanoparticles for nanoreactor applications. *Abstr Pap Am Chem S* **249** (2015).

88. De Volder, M.F.L., Tawfick, S.H., Baughman, R.H. & Hart, A.J. Carbon Nanotubes: Present and Future Commercial Applications. *Science* **339**, 535-539 (2013).

89. Zhang, Q., Wang, W.S., Goebl, J. & Yin, Y.D. Self-templated synthesis of hollow nanostructures. *Nano Today* **4**, 494-507 (2009).

90. Lou, J.Y., Xu, J. & Wang, K. Study on Construction Quality Control of Urban Complex Project Based on BIM. *Procedia Engineer* **174**, 668-676 (2017).

91. Chen, L.F., Lu, Y., Yu, L. & Lou, X.W. Designed formation of hollow particle-based nitrogen-doped carbon nanofibers for high-performance supercapacitors. *Energ Environ Sci* **10**, 1777-1783 (2017).

92. Liang, J.C. et al. Fabrication of TiO2 hollow nanocrystals through the nanoscale Kirkendall effect for lithium-ion batteries and photocatalysis. *New J Chem* **39**, 3145-3149 (2015).

93. Wang, W.S., Dahl, M. & Yin, Y.D. Hollow Nanocrystals through the Nanoscale Kirkendall Effect. *Chem Mater* **25**, 1179-1189 (2013).

94. Yin, Y.D. et al. Formation of hollow nanocrystals through the nanoscale Kirkendall Effect. *Science* **304**, 711-714 (2004).

95. da Silva, A.G.M., Rodrigues, T.S., Haigh, S.J. & Camargo, P.H.C. Galvanic replacement reaction: recent developments for engineering metal nanostructures towards catalytic applications. *Chem Commun* **53**, 7135-7148 (2017).

96. Gatemala, H., Ekgasit, S. & Pienpinijtham, P. 3D structure-preserving galvanic replacement to create hollow Au microstructures. *Crystengcomm* **19**, 3808-3816 (2017).

97. An, K. et al. Synthesis of Uniform Hollow Oxide Nanoparticles through Nanoscale Acid Etching. *Nano Lett* **8**, 4252-4258 (2008).

98. Sohn, J.H., Cha, H.G., Kim, C.W., Kim, D.K. & Kang, Y.S. Fabrication of hollow metal oxide nanocrystals by etching cuprous oxide with metal(II) ions: approach to the essential driving force. *Nanoscale* **5**, 11227-11233 (2013).

99. Fan, H.J., Gosele, U. & Zacharias, M. Formation of nanotubes and hollow nanoparticles based on Kirkendall and diffusion processes: A review. *Small* **3**, 1660-1671 (2007).

100. Railsback, J.G., Johnston-Peck, A.C., Wang, J.W. & Tracy, J.B. Size-Dependent Nanoscale Kirkendall Effect During the Oxidation of Nickel Nanoparticles. *Acs Nano* **4**, 1913-1920 (2010).

101. Cabot, A., Ibanez, M., Guardia, P. & Alivisatos, A.P. Reaction Regimes on the Synthesis of Hollow Particles by the Kirkendall Effect. *J Am Chem Soc* **131**, 11326-+ (2009).

102. Sun, Y.G., Mayers, B.T. & Xia, Y.N. Template-engaged replacement reaction: A one-step approach to the large-scale synthesis of metal nanostructures with hollow interiors. *Nano Lett* **2**, 481-485 (2002).

103. Oh, M.H. et al. Galvanic Replacement Reactions in Metal Oxide Nanocrystals. *Science* **340**, 964-968 (2013).

104. Chen, Y.H. et al. Hairy Uniform Permanently Ligated Hollow Nanoparticles with Precise Dimension Control and Tunable Optical Properties. *J Am Chem Soc* **139**, 12956-12967 (2017).

105. An, K. & Hyeon, T. Synthesis and biomedical applications of hollow nanostructures. *Nano Today* **4**, 359-373 (2009).

106. Kim, D. et al. Synthesis of hollow iron nanoframes. *J Am Chem Soc* **129**, 5812-+ (2007).

107. Sui, Y.M. et al. Synthesis of Cu2O Nanoframes and Nanocages by Selective Oxidative Etching at Room Temperature. *Angew Chem Int Edit* **49**, 4282-4285 (2010).

108. Feng, C.W., Pang, X.C., He, Y.J., Li, B. & Lin, Z.Q. Robust Route to Unimolecular Core-Shell and Hollow Polymer Nanoparticles. *Chem Mater* **26**, 6058-6067 (2014).

109. Pang, X.C., Zhao, L., Han, W., Xin, X.K. & Lin, Z.Q. A general and robust strategy for the synthesis of nearly monodisperse colloidal nanocrystals. *Nat Nanotechnol* **8**, 426-431 (2013).

110. Bohm, M.L. et al. Lead Telluride Quantum Dot Solar Cells Displaying External Quantum Efficiencies Exceeding 120%. *Nano Lett* **15**, 7987-7993 (2015).

111. Finefrock, S.W. et al. Measurement of Thermal Conductivity of PbTe Nanocrystal Coated Glass Fibers by the 3 omega Method. *Nano Lett* **13**, 5006-5012 (2013).

112. Saran, R. & Curry, R.J. Lead sulphide nanocrystal photodetector technologies. *Nat Photonics* **10**, 81-92 (2016).

113. Zeng, H.B. et al. ZnO-based hollow nanoparticles by selective etching: Elimination and reconstruction of metal-semiconductor interface, improvement of blue emission and photocatalysis. *Acs Nano* **2**, 1661-1670 (2008).

114. Sun, C.Q. Size dependence of nanostructures: Impact of bond order deficiency. *Prog Solid State Ch* **35**, 1-159 (2007).

115. Ziqubu, N., Ramasamy, K., Rajasekhar, P.V.S.R., Revaprasadu, N. & O'Brien, P. Simple Route to Dots and Rods of PbTe Nanocrystals. *Chem Mater* **22**, 3817-3819 (2010).

116. Pang, X.C., Zhao, L., Akinc, M., Kim, J.K. & Lin, Z.Q. Novel Amphiphilic Multi-Arm, Star-Like Block Copolymers as Unimolecular Micelles. *Macromolecules* **44**, 3746-3752 (2011).

117. Im, J.H., Jang, I.H., Pellet, N., Gratzel, M. & Park, N.G. Growth of CH3NH3PbI3 cuboids with controlled size for high-efficiency perovskite solar cells. *Nat Nanotechnol* **9**, 927-932 (2014).

118. Luo, J. et al. Tailored Engineering of an Unusual (C4H9NH3)2(CH3NH3)2Pb3Br10 Two-dimensional Multilayered Perovskite Ferroelectric for High Performance Photodetectors. *Angew Chem Int Ed Engl* (2017).

119. Li, G.R. et al. Highly Efficient Perovskite Nanocrystal Light-Emitting Diodes Enabled by a Universal Crosslinking Method. *Adv Mater* **28**, 3528-+ (2016).

120. Zhang, X.Y. et al. Enhancing the Brightness of Cesium Lead Halide Perovskite Nanocrystal Based Green Light-Emitting Devices through the Interface Engineering with Perfluorinated Ionomer. *Nano Lett* **16**, 1415-1420 (2016).

121. Xu, Y.Q. et al. Two-Photon-Pumped Perovskite Semiconductor Nanocrystal Lasers. *J Am Chem Soc* **138**, 3761-3768 (2016).

122. Huang, S.Q. et al. Enhancing the Stability of CH3NH3PbBr3 Quantum Dots by Embedding in Silica Spheres Derived from Tetramethyl Orthosilicate in "Waterless" Toluene. *J Am Chem Soc* **138**, 5749-5752 (2016).

123. Li, Z.C., Kong, L., Huang, S.Q. & Li, L. Highly Luminescent and Ultrastable CsPbBr3 Perovskite Quantum Dots Incorporated into a Silica/Alumina Monolith. *Angew Chem Int Edit* **56**, 8134-8138 (2017).

124. Loiudice, A., Saris, S., Oveisi, E., Alexander, D.T.L. & Buonsanti, R. CsPbBr3 QD/AlOx Inorganic Nanocomposites with Exceptional Stability in Water, Light, and Heat. *Angew Chem Int Ed Engl* **56**, 10696-10701 (2017).

125. Malgras, V. et al. Observation of Quantum Confinement in Monodisperse Methylammonium Lead Halide Perovskite Nanocrystals Embedded in Mesoporous Silica. *J Am Chem Soc* **138**, 13874-13881 (2016).

126. Wang, H.C. et al. Mesoporous Silica Particles Integrated with All-Inorganic CsPbBr3 Perovskite Quantum-Dot Nanocomposites (MP-PQDs) with High Stability and Wide Color Gamut Used for Backlight Display. *Angew Chem Int Edit* **55**, 7924-7929 (2016).

127. Wang, Y.N. et al. Ultrastable, Highly Luminescent Organic-Inorganic Perovskite-Polymer Composite Films. *Adv Mater* **28**, 10710-+ (2016).

128. Luo, B.B. et al. Organolead Halide Perovskite Nanocrystals: Branched Capping Ligands Control Crystal Size and Stability. *Angew Chem Int Edit* **55**, 8864-8868 (2016).

129. Wang, L.L. et al. Scalable Ligand-Mediated Transport Synthesis of Organic-Inorganic Hybrid Perovskite Nanocrystals with Resolved Electronic Structure and Ultrafast Dynamics. *Acs Nano* **11**, 2689-2696 (2017).

130. De Roo, J. et al. Highly Dynamic Ligand Binding and Light Absorption Coefficient of Cesium Lead Bromide Perovskite Nanocrystals. *Acs Nano* **10**, 2071-2081 (2016).

131. Li, Z.Y., Li, P.P. & Huang, J.L. Synthesis of amphiphilic copolymer brushes: Poly(ethylene oxide)-graft-polystyrene. *J Polym Sci Pol Chem* **44**, 4361-4371 (2006).

132. Pang, X.C., He, Y.J., Jung, J.H. & Lin, Z.Q. 1D nanocrystals with precisely controlled dimensions, compositions, and architectures. *Science* **353**, 1268-1272 (2016).

133. Kim, Y. et al. Efficient Luminescence from Perovskite Quantum Dot Solids. *Acs Appl Mater Inter* **7**, 25007-25013 (2015).

134. Liu, Y. et al. Atomistic Origins of Surface Defects in CH3NH3PbBr3 Perovskite and Their Electronic Structures. *Acs Nano* **11**, 2060-2065 (2017).

135. Meyns, M. et al. Polymer-Enhanced Stability of Inorganic Perovskite Nanocrystals and Their Application in Color Conversion LEDs. *Acs Appl Mater Inter* **8**, 19579-19586 (2016).

136. Wang, Y.J. et al. Visible light driven type II heterostructures and their enhanced photocatalysis properties: a review. *Nanoscale* **5**, 8326-8339 (2013).

137. Wang, J., Peng, L., Cao, F., Su, B.Q. & Shi, H. A Fe3O4-SiO2-TiO2 core-shell nanoparticle: Preparation and photocatalytic properties. *Inorg Nano-Met Chem* **47**, 396-400 (2017).

138. Yan, X.C. et al. High Performance Lithium Secondary Batteries Based on Novel Ni3Co6S8@C Core-Shell Nanoparticle. *J Nanosci Nanotechno* **17**, 5384-5390 (2017).

139. Zhang, H.X., Zhang, Z.W., Li, N., Yan, W.J. & Zhu, Z.P. Cu2O@C core/shell nanoparticle as an electrocatalyst for oxygen evolution reaction. *J Catal* **352**, 239-245 (2017).

140. Xu, Z.C., Hou, Y.L. & Sun, S.H. Magnetic core/shell Fe3O4/Au and Fe3O4/Au/Ag nanoparticles with tunable plasmonic properties. *J Am Chem Soc* **129**, 8698-+ (2007).

141. Zhang, J.T., Tang, Y., Lee, K. & Ouyang, M. Tailoring light-matter-spin interactions in colloidal hetero-nanostructures. *Nature* **466**, 91-95 (2010).

142. Zhang, J.T., Tang, Y., Lee, K. & Min, O.Y. Nonepitaxial Growth of Hybrid Core-Shell Nanostructures with Large Lattice Mismatches. *Science* **327**, 1634-1638 (2010).

143. Wang, G. et al. Abnormal change of melting points of gold nanoparticles confined between two-layer graphene nanosheets. *Rsc Adv* **6**, 108343-108346 (2016).

144. Cho, Y., Lee, S.S. & Jung, J.H. Recyclable fluorimetric and colorimetric mercury-specific sensor using porphyrin-functionalized Au@SiO2 core/shell nanoparticles. *Analyst* **135**, 1551-1555 (2010).

145. Liz-Marzan, L.M., Giersig, M. & Mulvaney, P. Synthesis of nanosized gold-silica core-shell particles. *Langmuir* **12**, 4329-4335 (1996).

146. V, S.-M., Caruso, F. & Liz-Marzan, L.M. Coated colloids with tailored optical properties. *J Phys Chem B* **107**, 10990-10994 (2003).

147. Lu, Y., Yin, Y.D., Li, Z.Y. & Xia, Y.N. Synthesis and self-assembly of Au@SiO2 core-shell colloids. *Nano Lett* **2**, 785-788 (2002).

148. Kobayashi, Y. et al. Synthesis of Au-silica core-shell particles by sol-gel process. *Surf Eng* **28**, 129-133 (2012).

149. Alam, H. & Ramakrishna, S. A review on the enhancement of figure of merit from bulk to nano-thermoelectric materials. *Nano Energy* **2**, 190-212 (2013).

150. Elsheikh, M.H. et al. A review on thermoelectric renewable energy: Principle parameters that affect their performance. *Renew Sust Energ Rev* **30**, 337-355 (2014).

151. Tang, J.Y. et al. Holey Silicon as an Efficient Thermoelectric Material. *Nano Lett* **10**, 4279-4283 (2010).

152. Humphrey, T.E., O'Dwyer, M.F. & Linke, H. Power optimization in thermionic devices. *J Phys D Appl Phys* **38**, 2051-2054 (2005).

153. (!!! INVALID CITATION !!! 85, 86).